

Measurement of the Partial Widths Ratio

$$\Gamma(D_s^{*+} \rightarrow D_s^+ \pi^0) / \Gamma(D_s^{*+} \rightarrow D_s^+ \gamma)$$

at the *BABAR* Experiment

D I S S E R T A T I O N

zur Erlangung des akademischen Grades

Doctor rerum naturalium
(Dr. rer. nat.)

vorgelegt

der Fakultät Mathematik und Naturwissenschaften
der Technischen Universität Dresden

von

Diplom-Physiker Martin Dickopp
geboren am 05. Mai 1972 in Mülheim a. d. Ruhr

Gutachter:

Prof. Dr. Bernhard Spaan

Prof. Dr. Klaus R. Schubert

Prof. Dr. Helmut Koch

Datum des Einreichens der Arbeit: 05.04.2004

Datum der mündlichen Prüfung: 22.07.2004

Abstract

Using 90.4 fb^{-1} of data taken at the *BABAR* experiment in the years 1999 to 2002, the decays $D_s^{*+} \rightarrow D_s^+ \pi^0$ and $D_s^{*+} \rightarrow D_s^+ \gamma$ have been reconstructed with two different methods. Signal Monte Carlo events as well as D^{*0} decays have been used to determine the reconstruction efficiencies. Thereby, the partial widths ratio $\Gamma(D_s^{*+} \rightarrow D_s^+ \pi^0)/\Gamma(D_s^{*+} \rightarrow D_s^+ \gamma)$ has been measured in four different ways, and the following results have been obtained:

$$\begin{aligned}\Gamma(D_s^{*+} \rightarrow D_s^+ \pi^0)/\Gamma(D_s^{*+} \rightarrow D_s^+ \gamma) &= 0.0621 \pm 0.0049 \pm 0.0063; \\ \Gamma(D_s^{*+} \rightarrow D_s^+ \pi^0)/\Gamma(D_s^{*+} \rightarrow D_s^+ \gamma) &= 0.0653 \pm 0.0048 \pm 0.0082; \\ \Gamma(D_s^{*+} \rightarrow D_s^+ \pi^0)/\Gamma(D_s^{*+} \rightarrow D_s^+ \gamma) &= 0.0574 \pm 0.0046 \pm 0.0089; \\ \Gamma(D_s^{*+} \rightarrow D_s^+ \pi^0)/\Gamma(D_s^{*+} \rightarrow D_s^+ \gamma) &= 0.0593 \pm 0.0044 \pm 0.0092.\end{aligned}$$

The first error is statistical, the second represents systematic uncertainties.

Additionally, the partial widths ratio $\Gamma(D^{*0} \rightarrow D^0 \pi^0)/\Gamma(D^{*0} \rightarrow D^0 \gamma)$ has been measured:

$$\Gamma(D^{*0} \rightarrow D^0 \pi^0)/\Gamma(D^{*0} \rightarrow D^0 \gamma) = 1.7401 \pm 0.0204 \pm 0.1247.$$

Kurzfassung

Unter Benutzung von 90.4 fb^{-1} Daten, die das *BABAR*-Experiment in den Jahren 1999 bis 2002 genommen hat, wurden die Zerfälle $D_s^{*+} \rightarrow D_s^+ \pi^0$ und $D_s^{*+} \rightarrow D_s^+ \gamma$ mit zwei verschiedenen Methoden rekonstruiert. Die Rekonstruktions-Effizienzen wurden mittels Signal-Monte Carlo-Ereignissen und D^{*0} -Zerfällen ermittelt. Auf diese Weise wurde das Partialbreiten-Verhältnis $\Gamma(D_s^{*+} \rightarrow D_s^+ \pi^0)/\Gamma(D_s^{*+} \rightarrow D_s^+ \gamma)$ auf vier verschiedene Weisen gemessen, wobei sich folgende Ergebnisse ergaben:

$$\begin{aligned}\Gamma(D_s^{*+} \rightarrow D_s^+ \pi^0)/\Gamma(D_s^{*+} \rightarrow D_s^+ \gamma) &= 0.0621 \pm 0.0049 \pm 0.0063; \\ \Gamma(D_s^{*+} \rightarrow D_s^+ \pi^0)/\Gamma(D_s^{*+} \rightarrow D_s^+ \gamma) &= 0.0653 \pm 0.0048 \pm 0.0082; \\ \Gamma(D_s^{*+} \rightarrow D_s^+ \pi^0)/\Gamma(D_s^{*+} \rightarrow D_s^+ \gamma) &= 0.0574 \pm 0.0046 \pm 0.0089; \\ \Gamma(D_s^{*+} \rightarrow D_s^+ \pi^0)/\Gamma(D_s^{*+} \rightarrow D_s^+ \gamma) &= 0.0593 \pm 0.0044 \pm 0.0092.\end{aligned}$$

Der erste Fehler ist statistisch, der zweite repräsentiert systematische Unsicherheiten.

Zusätzlich wurde das Partialbreiten-Verhältnis $\Gamma(D^{*0} \rightarrow D^0 \pi^0)/\Gamma(D^{*0} \rightarrow D^0 \gamma)$ gemessen:

$$\Gamma(D^{*0} \rightarrow D^0 \pi^0)/\Gamma(D^{*0} \rightarrow D^0 \gamma) = 1.7401 \pm 0.0204 \pm 0.1247.$$

Contents

1	Introduction	1
1.1	Outline	2
2	Theory and Motivation	5
2.1	The Quark Model	5
2.2	Isospin Symmetry Breaking	6
2.3	Calculation of $\mathcal{B}(D_s^{*+} \rightarrow D_s^+ \pi^0)$	7
2.4	Previous Measurement	9
2.4.1	Comparison with the Theory	10
3	The <i>BABAR</i> Experiment	13
3.1	Introduction	13
3.2	The <i>BABAR</i> Detector	14
3.2.1	Coordinate System	15
3.2.2	The Silicon Vertex Tracker (SVT)	16
3.2.3	The Drift Chamber (DCH)	16
3.2.4	The Detector of Internally Reflected Cherenkov Light (DIRC)	17
3.2.5	The Electromagnetic Calorimeter (EMC)	19
3.2.6	The Solenoid Magnet	22
3.2.7	The Instrumented Flux Return (IFR)	22
3.3	Run Periods and Luminosity	22
4	Measurement of $\Gamma(D_s^{*+} \rightarrow D_s^+ \pi^0)/\Gamma(D_s^{*+} \rightarrow D_s^+ \gamma)$	25
4.1	Overview	25
4.1.1	Data and Monte Carlo Sets	25
4.2	Charged Particle Identification	27
4.2.1	Kaon Identification	28
4.2.2	Pion Identification	31
4.3	Energy Measurement	31
4.4	D_s^+ Reconstruction	32
4.4.1	Helicity Distribution	32
4.4.2	D_s^+ Candidate Selection	34
4.5	$\pi^0 \rightarrow \gamma\gamma$ Reconstruction	39

4.5.1	π^0 Candidate Selection	40
4.6	$D_s^{*+} \rightarrow D_s^+ \pi^0$ Reconstruction	44
4.6.1	Signal Shape Determination	44
4.6.2	Background Shape Determination	45
4.6.3	$D_s^{*+} \rightarrow D_s^+ \pi^0$ Event Yield	46
4.7	$D_s^{*+} \rightarrow D_s^+ \gamma$ Reconstruction	53
4.7.1	Signal Shape	53
4.7.2	$D_s^{*+} \rightarrow D_s^+ \gamma$ Event Yield	54
4.8	Efficiency Determination with Signal Monte Carlo Events	57
4.8.1	Systematic Uncertainties in Monte Carlo Efficiencies	57
4.8.2	Efficiencies from Signal Monte Carlo Events	61
4.9	Efficiency Determination with D^{*0} Decays	63
4.9.1	D^0 Reconstruction	63
4.9.2	$D^{*0} \rightarrow D^0 \pi^0$ Reconstruction	64
4.9.3	$D^{*0} \rightarrow D^0 \gamma$ Reconstruction	65
4.9.4	Efficiencies from D^{*0} Decays	66
4.9.5	Efficiencies of D^{*0} Decays from Signal Monte Carlo Events	67
4.10	Results	71
4.11	Measurement of $\Gamma(D^{*0} \rightarrow D^0 \pi^0)/\Gamma(D^{*0} \rightarrow D^0 \gamma)$	71
4.12	Confirmation of $D_{sJ}^*(2317)^+ \rightarrow D_s^+ \pi^0$	71
5	Background	73
5.1	D_s^+ Sidebands	73
5.1.1	$D_s^+ \pi^0$ Reconstructed from D_s^+ Sidebands	74
5.1.2	$D_s^+ \gamma$ Reconstructed from D_s^+ Sidebands	74
5.2	D^0 Sidebands	78
5.2.1	$D^0 \pi^0$ Reconstructed from D^0 Sidebands	78
5.2.2	$D^0 \gamma$ Reconstructed from D^0 Sidebands	79
5.3	π^0 Sidebands	81
5.3.1	$D_s^+ \pi^0$ and $D^0 \pi^0$ Reconstructed from π^0 Sidebands	81
5.3.2	Data with Monte Carlo Events Subtracted	85
6	Momentum Spectra	87
6.1	Introduction	87
6.2	Momentum Dependent Event Yields	87
6.3	Efficiency Correction	97
6.3.1	Determination of Momentum Dependent Efficiencies with Signal Monte Carlo Events	97
6.3.2	Efficiency Corrected Momentum Spectra	97
6.4	Momentum Dependent Partial Widths Ratios	103
6.5	Systematic Momentum Dependency	107
7	Systematic Uncertainties	111
7.1	Systematic Uncertainties on $\Gamma(D_s^{*+} \rightarrow D_s^+ \pi^0)/\Gamma(D_s^{*+} \rightarrow D_s^+ \gamma)$	111

7.2 Systematic Uncertainties on $\Gamma(D^{*0} \rightarrow D^0\pi^0)/\Gamma(D^{*0} \rightarrow D^0\gamma)$	113
8 Summary and Results	115
References	119
Acknowledgements	121

List of Figures

2.1	Classification of the light pseudoscalar mesons by isospin and strangeness	6
2.2	Feynman diagram of the process $D_s^{*+} \rightarrow D_s^+ \eta$	7
2.3	Correlation between $\mathcal{B}(D_s^{*+} \rightarrow D^+ \gamma)$ and $\mathcal{B}(D_s^{*+} \rightarrow D_s^+ \pi^0)$	9
2.4	$m_{D_s^+ \pi^0} - m_{D_s^+}$ mass difference as measured by CLEO	10
3.1	Longitudinal section through the <i>BABAR</i> detector	15
3.2	Longitudinal section through the silicon vertex tracker (SVT)	16
3.3	Schematic view of the DIRC	18
3.4	Transverse section through a DIRC bar box	18
3.5	Cherenkov angle θ_C vs. momentum p	19
3.6	Longitudinal section through the electromagnetic calorimeter (EMC)	20
3.7	Shape of the calorimeter crystals	21
3.8	Integrated luminosity vs. time	23
4.1	Momentum spectrum of charged particle candidates	28
4.2	dE/dx distribution for π^\pm and K^\pm in the SVT and DCH	29
4.3	Momentum domains in which SVT, DCH, and DIRC are considered for K^\pm identification	30
4.4	$K^+ K^-$ invariant mass distribution	33
4.5	Definition of the helicity angle θ_H	34
4.6	Distribution of $\cos \theta_H$	35
4.7	Normalized second Legendre polynomial \bar{P}_2	36
4.8	$\phi \pi^+$ invariant mass distribution	37
4.9	$\gamma \gamma$ invariant mass distribution	40
4.10	$\gamma \gamma$ invariant mass distribution for exclusive π^0 candidates	42
4.11	$\Delta m_{D_s^+ \pi^0}$ signal shape (matched generic Monte Carlo events)	47
4.12	$\Delta m_{D_s^+ \pi^0}$ background shape (unmatched generic Monte Carlo events)	49
4.13	$\Delta m_{D_s^+ \pi^0}$ invariant mass difference distribution	51
4.14	$\Delta m_{D_s^+ \gamma}$ signal shape (matched generic Monte Carlo events)	54
4.15	$\Delta m_{D_s^+ \gamma}$ invariant mass difference distribution	55
4.16	Signal Monte Carlo $\Delta m_{D_s^+ \pi^0}$ and $\Delta m_{D_s^+ \gamma}$ invariant mass difference distributions	57

4.17	Monte Carlo efficiency correction function for π^0 mesons	59
4.18	Signal Monte Carlo $\Delta m_{D_s^+\pi^0}$ and $\Delta m_{D_s^+\gamma}$ invariant mass difference distributions with ‘random killing’ and γ correction function for systematic uncertainties applied	60
4.19	$K^-\pi^+$ invariant mass distribution	64
4.20	$\Delta m_{D^0\pi^0}$ invariant mass difference distribution	65
4.21	$\Delta m_{D^0\gamma}$ background shape (unmatched generic Monte Carlo events) .	66
4.22	$\Delta m_{D^0\gamma}$ invariant mass difference distribution	67
4.23	Signal Monte Carlo $\Delta m_{D^0\pi^0}$ and $\Delta m_{D^0\gamma}$ invariant mass difference distributions	69
4.24	$D_s^+\pi^0$ invariant mass distribution in the region of the $D_{sJ}^*(2317)^+$ mass	72
5.1	$\Delta m_{D_s^+\pi^0}$ invariant mass difference distributions, D_s^+ sidebands . . .	76
5.2	$\Delta m_{D_s^+\gamma}$ invariant mass difference distributions, D_s^+ sidebands	77
5.3	$\Delta m_{D^0\pi^0}$ invariant mass difference distributions, D^0 sidebands	78
5.4	$\Delta m_{D^0\gamma}$ invariant mass difference distributions, D^0 sidebands	80
5.5	$\Delta m_{D_s^+\pi^0}$ invariant mass difference distributions, π^0 sidebands	83
5.6	$\Delta m_{D^0\pi^0}$ invariant mass difference distributions, π^0 sidebands	84
5.7	$\Delta m_{D_s^+\pi^0}$ invariant mass difference distributions, π^0 sidebands, data with Monte Carlo events subtracted	85
5.8	$\Delta m_{D^0\pi^0}$ invariant mass difference distributions, π^0 sidebands, data with Monte Carlo events subtracted	86
6.1	$\Delta m_{D_s^+\pi^0}$ invariant mass difference distributions in D_s^{*+} momentum bins, selection method	90
6.2	$\Delta m_{D_s^+\pi^0}$ invariant mass difference distributions in D_s^{*+} momentum bins, weighting method	91
6.3	$\Delta m_{D_s^+\gamma}$ invariant mass difference distributions in D_s^{*+} momentum bins, selection method	92
6.4	$\Delta m_{D_s^+\gamma}$ invariant mass difference distributions in D_s^{*+} momentum bins, weighting method	93
6.5	$\Delta m_{D^0\pi^0}$ invariant mass difference distributions in D^{*0} momentum bins	94
6.6	$\Delta m_{D^0\gamma}$ invariant mass difference distributions in D^{*0} momentum bins	95
6.7	Momentum spectra of $D_s^{*+} \rightarrow D_s^+\pi^0$ event yields	96
6.8	Momentum spectra of $D_s^{*+} \rightarrow D_s^+\gamma$ event yields	96
6.9	Momentum spectra of $D^{*0} \rightarrow D^0\pi^0$ and $D^{*0} \rightarrow D^0\gamma$ event yields . .	96
6.10	Momentum dependent efficiencies from signal Monte Carlo events . .	100
6.11	Efficiency corrected momentum spectra of $D_s^{*+} \rightarrow D_s^+\pi^0$ event yields	101
6.12	Efficiency corrected momentum spectra of $D_s^{*+} \rightarrow D_s^+\gamma$ event yields	101
6.13	Efficiency corrected momentum spectra of $D^{*0} \rightarrow D^0\pi^0$ and $D^{*0} \rightarrow D^0\gamma$ event yields	102
6.14	Momentum dependent $\Gamma(D_s^{*+} \rightarrow D_s^+\pi^0)/\Gamma(D_s^{*+} \rightarrow D_s^+\gamma)$ with efficiencies from signal Monte Carlo events	103

6.15	Momentum dependent $\Gamma(D_s^{*+} \rightarrow D_s^+ \pi^0)/\Gamma(D_s^{*+} \rightarrow D_s^+ \gamma)$ with efficiencies from D^{*0} decays	104
6.16	Momentum dependent $\Gamma(D^{*0} \rightarrow D^0 \pi^0)/\Gamma(D^{*0} \rightarrow D^0 \gamma)$ with efficiencies from signal Monte Carlo events	104
8.1	$\Gamma(D_s^{*+} \rightarrow D_s^+ \pi^0)/\Gamma(D_s^{*+} \rightarrow D_s^+ \gamma)$: comparison of methods	117

List of Figures

List of Tables

3.1	Fermion production cross-sections at $\sqrt{s} = 10.58$ GeV	14
4.1	Data sets used in this analysis	26
4.2	Generic Monte Carlo event sets used in this analysis	27
4.3	$\phi\pi^+$ invariant mass distribution fit results	38
4.4	$\gamma\gamma$ invariant mass distribution fit results	41
4.5	$\gamma\gamma$ invariant mass distribution fit results for exclusive π^0 candidates	43
4.6	Differences in fit results between inclusive and exclusive π^0 candidates	43
4.7	$\gamma\gamma$ invariant mass window where the fitted π^0 signal exceeds 0.2 times its maximum	43
4.8	$\Delta m_{D_s^+\pi^0}$ signal shape (matched generic Monte Carlo events) fit results	48
4.9	$\Delta m_{D_s^+\pi^0}$ background shape (unmatched generic Monte Carlo events) fit results	50
4.10	$\Delta m_{D_s^+\pi^0}$ invariant mass difference distribution fit results	52
4.11	$\Delta m_{D_s^+\gamma}$ signal shape (matched generic Monte Carlo events) fit results	54
4.12	$\Delta m_{D_s^+\gamma}$ invariant mass difference distribution fit results	56
4.13	Results of fits to signal Monte Carlo $\Delta m_{D_s^+\pi^0}$ and $\Delta m_{D_s^+\gamma}$ invariant mass difference distributions	58
4.14	Results of fits to signal Monte Carlo $\Delta m_{D_s^+\pi^0}$ and $\Delta m_{D_s^+\gamma}$ invariant mass difference distributions with ‘random killing’ and γ correction function for systematic uncertainties applied	61
4.15	Efficiencies of D_s^{*+} decays from signal Monte Carlo events	62
4.16	$K^-\pi^+$ invariant mass distribution fit results	64
4.17	$\Delta m_{D^0\pi^0}$ invariant mass difference distribution fit results	65
4.18	$\Delta m_{D^0\gamma}$ background shape (unmatched generic Monte Carlo events) fit results	67
4.19	$\Delta m_{D^0\gamma}$ invariant mass difference distribution fit results	68
4.20	Results of fits to signal Monte Carlo $\Delta m_{D^0\pi^0}$ and $\Delta m_{D^0\gamma}$ invariant mass difference distributions	70
4.21	Efficiencies of D^{*0} decays from signal Monte Carlo events	70
4.22	Partial widths ratio $\Gamma(D_s^{*+} \rightarrow D_s^+\pi^0)/\Gamma(D_s^{*+} \rightarrow D_s^+\gamma)$ (statistical errors only)	71

5.1	D_s^+ sideband definitions	73
5.2	Event yields in $\Delta m_{D_s^+\pi^0}$ invariant mass difference distributions, D_s^+ sidebands	74
5.3	Event yields in $\Delta m_{D_s^+\gamma}$ invariant mass difference distributions, D_s^+ sidebands	75
5.4	D^0 sideband definitions	78
5.5	Event yields in $\Delta m_{D^0\pi^0}$ invariant mass difference distributions, D^0 sidebands	79
5.6	Event yields in $\Delta m_{D^0\gamma}$ invariant mass difference distributions, D^0 sidebands	79
5.7	π^0 sideband definitions	81
5.8	Event yields in $\Delta m_{D_s^+\pi^0}$ invariant mass difference distributions, π^0 sidebands	82
5.9	Event yields in $\Delta m_{D^0\pi^0}$ invariant mass difference distributions, π^0 sidebands	82
5.10	Event yields in $\Delta m_{D_s^+\pi^0}$ invariant mass difference distributions, π^0 sidebands, data with Monte Carlo events subtracted	86
5.11	Event yields in $\Delta m_{D^0\pi^0}$ invariant mass difference distributions, π^0 sidebands, data with Monte Carlo events subtracted	86
6.1	$D_s^{*+} \rightarrow D_s^+\pi^0$ event yields in D_s^{*+} momentum bins	89
6.2	$D_s^{*+} \rightarrow D_s^+\gamma$ event yields in D_s^{*+} momentum bins	89
6.3	$D^{*0} \rightarrow D^0\pi^0$ and $D^{*0} \rightarrow D^0\gamma$ event yields in D^{*0} momentum bins	89
6.4	Momentum dependent $D_s^{*+} \rightarrow D_s^+\pi^0$ efficiency from signal Monte Carlo events, selection method	98
6.5	Momentum dependent $D_s^{*+} \rightarrow D_s^+\pi^0$ efficiency from signal Monte Carlo events, weighting method	98
6.6	Momentum dependent $D_s^{*+} \rightarrow D_s^+\gamma$ efficiency from signal Monte Carlo events, selection method	99
6.7	Momentum dependent $D_s^{*+} \rightarrow D_s^+\gamma$ efficiency from signal Monte Carlo events, weighting method	99
6.8	Momentum dependent $D^{*0} \rightarrow D^0\pi^0$ efficiency from signal Monte Carlo events	99
6.9	Momentum dependent $D^{*0} \rightarrow D^0\gamma$ efficiency from signal Monte Carlo events	100
6.10	Fits to momentum dependent efficiencies from signal Monte Carlo events	100
6.11	Fits of theoretical model functions to efficiency corrected momentum spectra	101
6.12	Momentum dependent $\Gamma(D_s^{*+} \rightarrow D_s^+\pi^0)/\Gamma(D_s^{*+} \rightarrow D_s^+\gamma)$ with efficiencies from signal Monte Carlo events	105
6.13	Momentum dependent $\Gamma(D_s^{*+} \rightarrow D_s^+\pi^0)/\Gamma(D_s^{*+} \rightarrow D_s^+\gamma)$ with efficiencies from D^{*0} decays	105
6.14	Momentum dependent $\Gamma(D^{*0} \rightarrow D^0\pi^0)/\Gamma(D^{*0} \rightarrow D^0\gamma)$	106

6.15	Systematic momentum dependencies	110
7.1	Summary of systematic uncertainties on $\Gamma(D_s^{*+} \rightarrow D_s^+ \pi^0)/\Gamma(D_s^{*+} \rightarrow D_s^+ \gamma)$	112
7.2	Summary of systematic uncertainties on $\Gamma(D^{*0} \rightarrow D^0 \pi^0)/\Gamma(D^{*0} \rightarrow D^0 \gamma)$	113
8.1	Partial widths ratio $\Gamma(D_s^{*+} \rightarrow D_s^+ \pi^0)/\Gamma(D_s^{*+} \rightarrow D_s^+ \gamma)$ and branching fractions $\mathcal{B}(D_s^{*+} \rightarrow D_s^+ \pi^0)$, $\mathcal{B}(D_s^{*+} \rightarrow D_s^+ \gamma)$	116
8.2	Partial widths ratio $\Gamma(D^{*0} \rightarrow D^0 \pi^0)/\Gamma(D^{*0} \rightarrow D^0 \gamma)$ and branching fractions $\mathcal{B}(D^{*0} \rightarrow D^0 \pi^0)$, $\mathcal{B}(D^{*0} \rightarrow D^0 \gamma)$	116

List of Tables

Chapter 1

Introduction

This dissertation presents an analysis in which the phenomenon of isospin symmetry breaking in the standard model is studied. The goal of the analysis is to measure the branching fraction of the isospin-violating decay¹ $D_s^{*+} \rightarrow D_s^+ \pi^0$; experimentally, this is best achieved by a measurement of the partial widths ratio $\Gamma(D_s^{*+} \rightarrow D_s^+ \pi^0)/\Gamma(D_s^{*+} \rightarrow D_s^+ \gamma)$. The same D_s^+ sample is used for the reconstruction of the decays $D_s^{*+} \rightarrow D_s^+ \pi^0$ and $D_s^{*+} \rightarrow D_s^+ \gamma$, so that systematic uncertainties in the D_s^+ reconstruction cancel in the ratio. Under the assumption that the D_s^{*+} meson can decay only to $D_s^+ \pi^0$ or $D_s^+ \gamma$, i.e., $\mathcal{B}(D_s^{*+} \rightarrow D_s^+ \pi^0) + \mathcal{B}(D_s^{*+} \rightarrow D_s^+ \gamma) = 1$, $\mathcal{B}(D_s^{*+} \rightarrow D_s^+ \pi^0)$ can be calculated from the partial widths ratio.

A previous measurement of the ratio $\Gamma(D_s^{*+} \rightarrow D_s^+ \pi^0)/\Gamma(D_s^{*+} \rightarrow D_s^+ \gamma)$ was performed by the CLEO Collaboration in 1995 [1], using 3.75 fb^{-1} of data. The ratio resulting from this measurement has a statistical error of $^{+32\%}_{-29\%}$ and a systematic uncertainty of $\pm 35\%$.

The analysis presented in this dissertation has used 90.40 fb^{-1} of data accumulated at the *BABAR* experiment in the years 1999 to 2002. While CLEO's previous result is confirmed, *BABAR*'s amount of data allows a measurement of $\Gamma(D_s^{*+} \rightarrow D_s^+ \pi^0)/\Gamma(D_s^{*+} \rightarrow D_s^+ \gamma)$ with much greater precision than CLEO could achieve.

BABAR has primarily been designed to study \mathcal{CP} violation in the system of $B^0 \bar{B}^0$ meson pairs, but its high luminosity allows a rich physics program, which makes it also ideally suited to study the physics of charmed mesons. *BABAR*'s recent observation of the charmed meson state $D_{sJ}^*(2317)^+$ [2] constitutes an important contribution to the area of charm physics.

An efficient detection of photons as well as a precise measurement of photon energies is crucial for this analysis, both for the reconstruction of the decay $D_s^{*+} \rightarrow D_s^+ \gamma$ and the reconstruction of π^0 mesons from the decay $D_s^{*+} \rightarrow D_s^+ \pi^0$. Specifically, due to the small mass difference [3]

$$m_{D_s^{*+}} - m_{D_s^+} = 143.8 \text{ MeV}/c^2, \quad (1.1)$$

¹References to a specific particle or decay channel also imply the charge-conjugated particle or decay channel. E.g., the notation $D_s^{*+} \rightarrow D_s^+ \pi^0$ also implies the decay $D_s^{*-} \rightarrow D_s^- \pi^0$.

which is only slightly larger than the π^0 mass $m_{\pi^0} = 135.0 \text{ MeV}/c^2$ [3], the decay $D_s^{*+} \rightarrow D_s^+ \pi^0$ produces *slow* π^0 mesons. With its electromagnetic calorimeter (described in detail in Section 3.2.5), which is designed to be efficient over a wide energy range, the *BABAR* detector is well suited for this task. It is therefore possible to use π^0 mesons with a momentum in the center-of-mass frame of $p_{\pi^0}^* > 150 \text{ MeV}/c$, while CLEO used only π^0 mesons with a momentum of $p_{\pi^0}^* > 250 \text{ MeV}/c$ [1].

The reconstruction efficiencies of the decays $D_s^{*+} \rightarrow D_s^+ \pi^0$ and $D_s^{*+} \rightarrow D_s^+ \gamma$ are determined in two different ways. First of all, signal Monte Carlo events are used, and secondly, the ratio of the efficiencies is obtained from a measurement of the event yield ratio of the decays $D^{*0} \rightarrow D^0 \pi^0$ and $D^{*0} \rightarrow D^0 \gamma$. The latter method requires knowledge of the branching fractions of these decays, which are currently not known with great precision. Therefore, the smallest uncertainty in $\Gamma(D_s^{*+} \rightarrow D_s^+ \pi^0)/\Gamma(D_s^{*+} \rightarrow D_s^+ \gamma)$ is achieved by determining the efficiencies with signal Monte Carlo events. However, if $\mathcal{B}(D^{*0} \rightarrow D^0 \pi^0)/\mathcal{B}(D^{*0} \rightarrow D^0 \gamma)$ is measured with greater precision in the future, this also improves the precision of $\Gamma(D_s^{*+} \rightarrow D_s^+ \pi^0)/\Gamma(D_s^{*+} \rightarrow D_s^+ \gamma)$, so that ultimately the second method of determining the efficiencies could become superior to the first.

Alternatively, the measurement of the event yield ratio $N(D^{*0} \rightarrow D^0 \pi^0)/N(D^{*0} \rightarrow D^0 \gamma)$ can be used to determine the partial width ratio $\Gamma(D^{*0} \rightarrow D^0 \pi^0)/\Gamma(D^{*0} \rightarrow D^0 \gamma)$, if the ratio of the efficiencies is calculated from signal Monte Carlo events. The result is also presented in this dissertation.

1.1 Outline

This dissertation is structured in the following way:

- Chapter 2 gives a short introduction to the theory of isospin symmetry breaking in the standard model and describes the prediction for $\mathcal{B}(D_s^{*+} \rightarrow D_s^+ \pi^0)$ as calculated using chiral perturbation theory.
- The *BABAR* experiment and detector are presented in Chapter 3. This chapter describes the subsystems of the *BABAR* detector and their properties.
- Chapter 4 presents the measurement of the partial widths ratio $\Gamma(D_s^{*+} \rightarrow D_s^+ \pi^0)/\Gamma(D_s^{*+} \rightarrow D_s^+ \gamma)$. First of all, the particle identification and the reconstruction of D_s^+ mesons are described. The next section explains the selection of $\pi^0 \rightarrow \gamma\gamma$ candidates. Following sections present how the decays $D_s^{*+} \rightarrow D_s^+ \pi^0$ and $D_s^{*+} \rightarrow D_s^+ \gamma$ have been reconstructed.

Finally, the two methods for the determination of the reconstruction efficiencies, signal Monte Carlo events and measurements of $N(D^{*0} \rightarrow D^0 \pi^0)$ and $N(D^{*0} \rightarrow D^0 \gamma)$, are introduced, and the results for the measurements of $\Gamma(D_s^{*+} \rightarrow D_s^+ \pi^0)/\Gamma(D_s^{*+} \rightarrow D_s^+ \gamma)$ and $\Gamma(D^{*0} \rightarrow D^0 \pi^0)/\Gamma(D^{*0} \rightarrow D^0 \gamma)$ are shown.

- Chapter 5 describes how the backgrounds under the D_s^{*+} and D^{*0} signals have been studied and how these backgrounds affect the result. D_s^+ , D^0 , and π^0 sidebands have been analyzed.
- To test for a possible momentum dependency of $\Gamma(D_s^{*+} \rightarrow D_s^+\pi^0)/\Gamma(D_s^{*+} \rightarrow D_s^+\gamma)$, the ratio has been measured separately in five momentum bins. This test is presented in Chapter 6, and the systematic uncertainty caused by a possibly unknown momentum dependency is estimated.
- Chapter 7 summarizes the systematic uncertainties.
- Finally, the results are shown in Chapter 8.

Chapter 2

Theory and Motivation

2.1 The Quark Model

The quarks as the constituents of the mesons and baryons can be divided into three ‘families’, where corresponding members of different families differ in their mass, but have the same electric charge:

$$\begin{array}{ccc} \begin{pmatrix} u \\ d \end{pmatrix} & \begin{pmatrix} c \\ s \end{pmatrix} & \begin{pmatrix} t \\ b \end{pmatrix} & \begin{array}{l} Q = +2/3e \\ Q = -1/3e \end{array} \end{array}$$

Antiquarks have the same mass as the corresponding quarks, but opposite electric charge.

The two lightest quarks, u and d , both have similar constituent masses $m_{ud} \approx 300 \text{ MeV}/c^2$, which makes it possible for $u\bar{u}$ and $d\bar{d}$ states to mix. This phenomenon is described by the isospin I : u and d form an isospin doublet ($I = 1/2$) with $I_3 = +1/2$ for the u and $I_3 = -1/2$ for the d quark. I_3 of the antiquarks has the opposite sign as I_3 of the corresponding quark.

The next heavier quark, s , has isospin $I = 0$. It is characterized by a new quantum number, the ‘strangeness’ S , which is -1 for the s quark and $+1$ for the \bar{s} antiquark. The three quarks u , d , and s can be combined to the flavor symmetry group $\text{SU}(3)$; the nine combinations are represented as an octet and a singlet. Considering only pseudoscalar ($J^P = 0^-$) mesons, the octet states are

- $|\pi^+\rangle = |u\bar{d}\rangle$,
- $|\pi^-\rangle = |d\bar{u}\rangle$,
- $|K^+\rangle = |u\bar{s}\rangle$,
- $|K^-\rangle = |\bar{u}s\rangle$,
- $|K^0\rangle = |d\bar{s}\rangle$,
- $|\bar{K}^0\rangle = |\bar{d}s\rangle$,

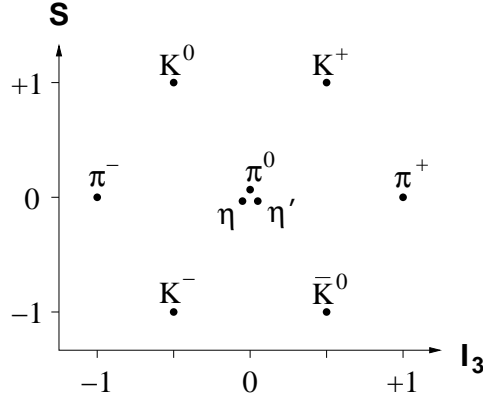


Figure 2.1: Classification of the light pseudoscalar mesons by isospin I_3 and strangeness S .

- $|\pi^0\rangle = (|u\bar{u}\rangle - |d\bar{d}\rangle) / \sqrt{2}$,
- $|\eta_8\rangle = (|u\bar{u}\rangle + |d\bar{d}\rangle - 2|s\bar{s}\rangle) / \sqrt{6}$,

and the singlet state is

- $|\eta_1\rangle = (|u\bar{u}\rangle + |d\bar{d}\rangle + |s\bar{s}\rangle) / \sqrt{3}$.

The s quark is heavier than the u and d quarks; it has a constituent mass of approximately $m_s \approx 450 \text{ MeV}/c^2$. Therefore, the $SU(3)$ symmetry is broken, which causes the $|\eta_8\rangle$ and $|\eta_1\rangle$ states to mix. However, there is only a slight mixing, so that the physical states $|\eta\rangle$ and $|\eta'\rangle$ correspond almost exactly to $|\eta_8\rangle$ and $|\eta_1\rangle$, respectively. A classification of the light pseudoscalar mesons by isospin I_3 and strangeness S is depicted in Figure 2.1.

2.2 Isospin Symmetry Breaking

Due to the mass difference between the u and d quarks [4],

$$\frac{m_d - m_u}{m_d + m_u} = 0.29 \pm 0.05, \quad (2.1)$$

the isospin symmetry is broken, and therefore mixing between the π^0 and the η mesons is possible. It is described by a mixing angle θ , which in lowest order chiral perturbation theory is given by [5]

$$\theta = \frac{\sqrt{3}}{4} \frac{m_d - m_u}{m_s - m_{ud}}, \quad m_{ud} = \frac{m_u + m_d}{2}. \quad (2.2)$$

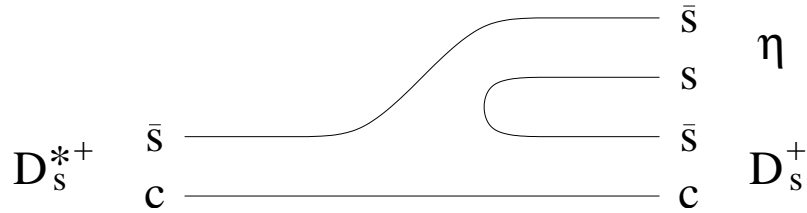


Figure 2.2: Feynman diagram of the process $D_s^{*+} \rightarrow D_s^+ \eta$. The η couples through its $s\bar{s}$ component.

The numerical value thereby obtained for the mixing angle is $\theta \approx 0.01$, but it should be noted that next to leading order corrections are typically of the order of 30% [4].

Experimentally, the phenomenon can best be studied by measuring the branching fraction for the $D_s^{*+} \rightarrow D_s^+ \pi^0$ decay [6]. The D_s^{*+} and D_s^+ mesons both have isospin $I = 0$, while the π^0 meson has isospin $I = 1$, so unlike the hadronic D^{*+} decay, $D_s^{*+} \rightarrow D_s^+ \pi^0$ is an isospin-violating process.

Cho and Wise describe the decay at tree level as the emission of a virtual η by the D_s^{*+} , which is isospin-conserving, followed by the isospin-violating mixing of the η into a π^0 [6]. The $D_s^{*+} \rightarrow D_s^+ \eta$ transition is dominantly strong, but also contains a small electromagnetic contribution, which is suppressed by a factor of $\alpha/\pi \approx 1/430$, and is therefore neglected in the partial width calculation.

The η couples through its $s\bar{s}$ component. The process is shown in Figure 2.2.

2.3 Calculation of $\mathcal{B}(D_s^{*+} \rightarrow D_s^+ \pi^0)$

A calculation of the partial width yields

$$\Gamma(D_s^{*+} \rightarrow D_s^+ \pi^0) = \frac{g^2}{48\pi f_\eta^2} \left(\frac{m_d - m_u}{m_s - m_{ud}} \right)^2 p_{\pi^0}^3, \quad (2.3)$$

where g denotes the (unknown) coupling constant, f_η the decay constant, and p_{π^0} the momentum of the π^0 meson. The usage of $f_\eta = 171$ MeV instead of $f_\pi = 132$ MeV takes higher order chiral perturbation theory SU(3) breaking into account.

It is possible to get rid of the unknown coupling constant g in the limit of SU(3) symmetry. By assuming $\Gamma(D_s^{*+} \rightarrow D_s^+ \gamma) = \Gamma(D^{*+} \rightarrow D^+ \gamma)$ and $f_\eta = f_\pi$, Equation 2.3 and the partial width

$$\Gamma(D^{*+} \rightarrow D^0 \pi^+) = \frac{g^2}{6\pi f_\pi^2} p_{\pi^+}^3 \quad (2.4)$$

can be used to calculate

$$\begin{aligned}
 \mathcal{B}(D_s^{*+} \rightarrow D_s^+ \pi^0) &\approx \frac{\Gamma(D_s^{*+} \rightarrow D_s^+ \pi^0)}{\Gamma(D_s^{*+} \rightarrow D_s^+ \gamma)} \\
 &= \frac{1}{8} \left(\frac{m_d - m_u}{m_s - m_{ud}} \right)^2 \frac{p_{\pi^0}^3}{p_{\pi^+}^3} \frac{\mathcal{B}(D^{*+} \rightarrow D^0 \pi^+)}{\mathcal{B}(D^{*+} \rightarrow D^+ \gamma)} \\
 &= \frac{2}{3} \theta^2 \frac{p_{\pi^0}^3}{p_{\pi^+}^3} \frac{\mathcal{B}(D^{*+} \rightarrow D^0 \pi^+)}{\mathcal{B}(D^{*+} \rightarrow D^+ \gamma)}.
 \end{aligned} \tag{2.5}$$

With $\theta = 0.01$ and the measured branching fraction $\mathcal{B}(D^{*+} \rightarrow D^0 \pi^+) = 67.7\%$ [3], the following result is obtained:

$$\mathcal{B}(D_s^{*+} \rightarrow D_s^+ \pi^0) \approx \frac{8 \times 10^{-5}}{\mathcal{B}(D^{*+} \rightarrow D^+ \gamma)}. \tag{2.6}$$

The partial widths of the electromagnetic transitions of charmed vector mesons to their pseudoscalar counterparts

$$\Gamma(D_i^* \rightarrow D_i \gamma) = \frac{\alpha}{3} |\mu_i|^2 p_\gamma^3, \quad i \in \{u, d, s\}, \quad D_i^{(*)} \in \{D^{(*)0}, D^{(*)+}, D_s^{(*)+}\} \tag{2.7}$$

depend on the transition magnetic moments μ_i . Since both the coupling to the heavy charm quark and to the light quark contribute, the $\mu_i = \mu^{(h)} + \mu_i^{(\ell)}$ are the sum of the charm magnetic moment, $\mu^{(h)} = 2/(3m_c)$, which is fixed by heavy quark spin symmetry, and the light quark magnetic moments $\mu_i^{(\ell)} = \beta Q_i$, which in the SU(3) symmetry limit are proportional to the electric charges of the quarks with some unknown proportionality constant β .

In chiral perturbation theory, the leading SU(3) corrections, which arise from one-loop Feynman diagrams, are calculable and are of the order $O(\sqrt{m_q})$. They modify the light quark transition moments in the following way [7]:

$$\mu_u^{(\ell)} = +\frac{2}{3}\beta - \frac{g^2 m_K}{4\pi f_K^2} - \frac{g^2 m_\pi}{4\pi f_\pi^2}, \tag{2.8}$$

$$\mu_d^{(\ell)} = -\frac{1}{3}\beta + \frac{g^2 m_\pi}{4\pi f_\pi^2}, \tag{2.9}$$

$$\mu_s^{(\ell)} = -\frac{1}{3}\beta + \frac{g^2 m_K}{4\pi f_K^2}. \tag{2.10}$$

It should be noted that since a neutral pion or kaon does not couple to the photon, only virtual states with a charged pion or kaon contribute to the corrections of the magnetic moments. The one-loop contributions are therefore not in the ratio $+2 : -1 : -1$, i.e., they violate SU(3) symmetry.

The moments depend on the unknown values of β and g , which can be determined by measurements of the independent radiative branching fractions $\mathcal{B}(D^{*0} \rightarrow D^0 \gamma)$ and $\mathcal{B}(D^{*+} \rightarrow D^+ \gamma)$. Once β and g are known as functions of $\mathcal{B}(D^{*+} \rightarrow D^+ \gamma)$, it is

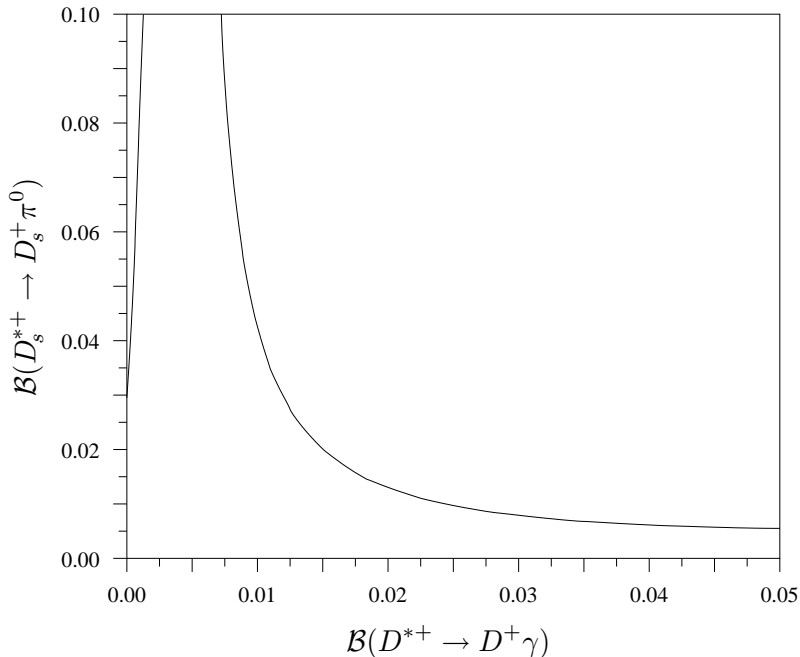


Figure 2.3: Correlation between $\mathcal{B}(D_s^{*+} \rightarrow D^+\gamma)$ and $\mathcal{B}(D_s^{*+} \rightarrow D_s^+\pi^0)$ [6]. Leading SU(3) corrections to the transition magnetic moments are included.

also possible to calculate $\mathcal{B}(D_s^{*+} \rightarrow D_s^+\pi^0)$ as function of $\mathcal{B}(D_s^{*+} \rightarrow D^+\gamma)$ [6]. For $\mathcal{B}(D_s^{*+} \rightarrow D^+\gamma) = (1.6 \pm 0.4)\%$ [3], $\mathcal{B}(D_s^{*+} \rightarrow D_s^+\pi^0)$ is in the range of $1 \sim 3\%$. However, it should be noted that $\mathcal{B}(D_s^{*+} \rightarrow D_s^+\pi^0)$ and $\mathcal{B}(D_s^{*+} \rightarrow D^+\gamma)$ are highly correlated. Specifically, for smaller values of $\mathcal{B}(D_s^{*+} \rightarrow D^+\gamma)$, there is a strong cancellation between $\mu^{(h)}$ and $\mu_s^{(\ell)}$ which greatly enhances $\mathcal{B}(D_s^{*+} \rightarrow D_s^+\pi^0)$. The correlation between $\mathcal{B}(D_s^{*+} \rightarrow D^+\gamma)$ and $\mathcal{B}(D_s^{*+} \rightarrow D_s^+\pi^0)$ is shown in Figure 2.3.

SU(3) corrections to the transition magnetic moments of the order $O(m_q)$ may also be important [6]. Unfortunately, these corrections are not completely calculable, so that unknown terms enter into Equations 2.8–2.10.

2.4 Previous Measurement

The partial widths ratio $\Gamma(D_s^{*+} \rightarrow D_s^+\pi^0)/\Gamma(D_s^{*+} \rightarrow D^+\gamma)$ was measured by the CLEO Collaboration in 1995 [1]. In 3.75 fb^{-1} of data, the decay chain $D_s^+ \rightarrow \phi\pi^+$, $\phi \rightarrow K^+K^-$ was reconstructed to search for $D_s^{*+} \rightarrow D_s^+\pi^0$. After the application of various selection criteria, $14.7^{+4.6}_{-4.0}$ $D_s^{*+} \rightarrow D_s^+\pi^0$ events and 944 ± 57 $D_s^{*+} \rightarrow D^+\gamma$ events were found (statistical errors only). The $D_s^{*+} \rightarrow D_s^+\pi^0$ signal is shown in Figure 2.4.

The ratio of the efficiencies of the hadronic and radiative D_s^{*+} decays was esti-

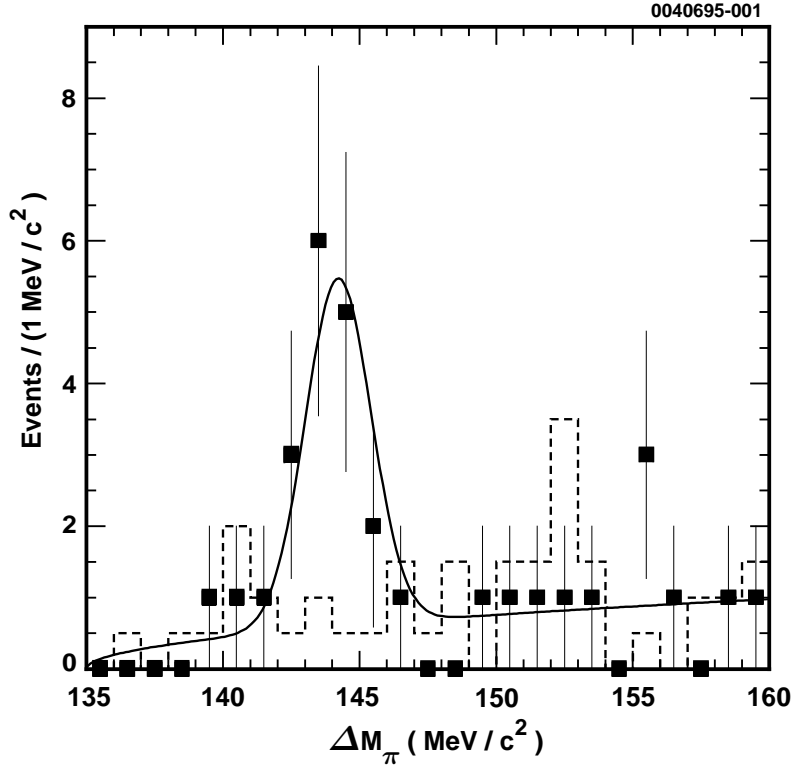


Figure 2.4: $m_{D_s^+\pi^0} - m_{D_s^+}$ mass difference as measured by the CLEO Collaboration in 1995 [1]. The points are the data, the solid line is the fit to the data, and the dashed line is an estimate of the background.

mated with Monte Carlo events. CLEO has obtained a partial widths ratio of

$$\frac{\Gamma(D_s^{*+} \rightarrow D_s^+\pi^0)}{\Gamma(D_s^{*+} \rightarrow D_s^+\gamma)} = 0.062^{+0.020}_{-0.018} \pm 0.022. \quad (2.11)$$

2.4.1 Comparison with the Theory

If the D_s^{*+} meson decays only the $D_s^+\pi^0$ and $D_s^+\gamma$, i.e., $\mathcal{B}(D_s^{*+} \rightarrow D_s^+\pi^0) + \mathcal{B}(D_s^{*+} \rightarrow D_s^+\gamma) = 1$, the branching fractions can be calculated from the partial widths ratio. The branching fraction of the hadronic D_s^{*+} decay thereby obtained is

$$\mathcal{B}(D_s^{*+} \rightarrow D_s^+\pi^0) = 0.058^{+0.018}_{-0.016} \pm 0.020. \quad (2.12)$$

While this number is significantly larger than the theoretical prediction of $0.01 \sim 0.03$, it must be taken into account that the latter has large uncertainties. Specifically,

- the mixing angle θ , which enters into Equation 2.5 quadratically, has a large uncertainty of 30%, and
- unknown terms enter into the SU(3) corrections to the transition magnetic moments (Equations 2.8–2.10).

Chapter 3

The *BABAR* Experiment

3.1 Introduction

In 1964, Christenson, Cronin, Fitch, and Turlay published their discovery that nature is not invariant under the symmetry known as \mathcal{CP} , the simultaneous interchange of particles with antiparticles (charge conjugation \mathcal{C}) and spatial inversion (parity \mathcal{P}) [8]. They had demonstrated that the long-lived component of the neutral K meson, known as K_L^0 , can decay to two charged pions $\pi^+\pi^-$ with a branching fraction in the order of 10^{-3} . Since K_L^0 is a \mathcal{CP} eigenstate with eigenvalue -1 , while the two-pion system $\pi^+\pi^-$ is a \mathcal{CP} eigenstate with eigenvalue $+1$, the decay violates \mathcal{CP} symmetry. Cronin and Fitch received the 1980 Nobel Prize in Physics for the discovery.

The Standard Model of particle physics has no explanation for what causes the phenomenon of \mathcal{CP} violation. It was therefore proposed in 1993 to construct an ‘Asymmetric B Factory’ at the Stanford Linear Accelerator Center (SLAC) to facilitate the study of \mathcal{CP} violation in the system of $B^0\bar{B}^0$ meson pairs [9]. The new machine, to be built into the existing tunnel of the Positron Electron Project (PEP) and therefore dubbed PEP-II, would collide 9 GeV electrons and 3.1 GeV positrons at an unprecedentedly high luminosity of $3 \times 10^{33} \text{ cm}^{-2}\text{s}^{-1}$. The collision energy of $\sqrt{s} = 10.58 \text{ GeV}$ in the center-of-mass frame excites the $\Upsilon(4S)$ resonance, which decays almost exclusively to a pair of B mesons ($B^0\bar{B}^0$ or B^+B^-) [3].

Due to the different energies of the electrons and positrons, the center-of-mass frame is boosted with $\beta\gamma = 0.56$ with respect to the laboratory frame. The B and \bar{B} move almost in parallel along the boost direction, so that, even without an exact knowledge of the position of the primary vertex, the spatial, and therefore also the temporal, distance between the decays of the B mesons can be determined if the decay vertices are reconstructed. Knowledge of this distance is crucial for the study of flavor oscillations and \mathcal{CP} violation.

A Letter of Intent to build a detector, named *BABAR*, at the PEP-II facility was published in 1994 [10], followed by a Technical Design Report one year later [11]. The *BABAR* experiment started to take data in October 1999. At the 30th International

$e^+e^- \rightarrow$	Cross-section
$b\bar{b}$	1.05 nb
$c\bar{c}$	1.30 nb
$s\bar{s}$	0.35 nb
$u\bar{u}$	1.39 nb
$d\bar{d}$	0.35 nb
$\tau^+\tau^-$	0.94 nb
$\mu^+\mu^-$	1.16 nb
e^+e^-	≈ 40 nb

Table 3.1: Fermion production cross-sections at the energy of the $\Upsilon(4S)$ resonance, $\sqrt{s} = 10.58$ GeV [16]. The $e^+e^- \rightarrow e^+e^-$ cross-section refers only to events which are entirely contained within the geometrical acceptance solid-angle of the *BABAR* detector.

Conference on High-Energy Physics (ICHEP 2000) in Osaka, Japan, *BABAR* and the Japanese Belle experiment simultaneously announced their discovery of \mathcal{CP} violation in the $B^0\bar{B}^0$ meson system [12, 13]. Both experiments published their results in 2001 [14, 15].

While *BABAR* is optimized for the study of \mathcal{CP} asymmetries in the B meson system, the high luminosity also makes it ideally suited for searches for rare decays, and for precision measurements of the decays of bottom and charm mesons and τ leptons. Table 3.1 lists the fermion production cross-sections at $\sqrt{s} = 10.58$ GeV.

3.2 The *BABAR* Detector

A detailed description of the *BABAR* detector can be found in [17]. The need to fully reconstruct B^0 mesons in various exclusive final states (many of which include several charged particles and π^0 mesons), and tag the flavor of the second neutral B , both with high efficiency, places a number of requirements on the detector:

- Large geometrical acceptance;
- High reconstruction efficiency for charged particles down to low momenta of 60 MeV/ c , and for photons down to low energies of 20 MeV;
- Very good momentum and vertex resolution;
- Very good energy and angular resolution for the detection of photons over a wide energy range;
- Efficient particle identification for both leptons and hadrons.

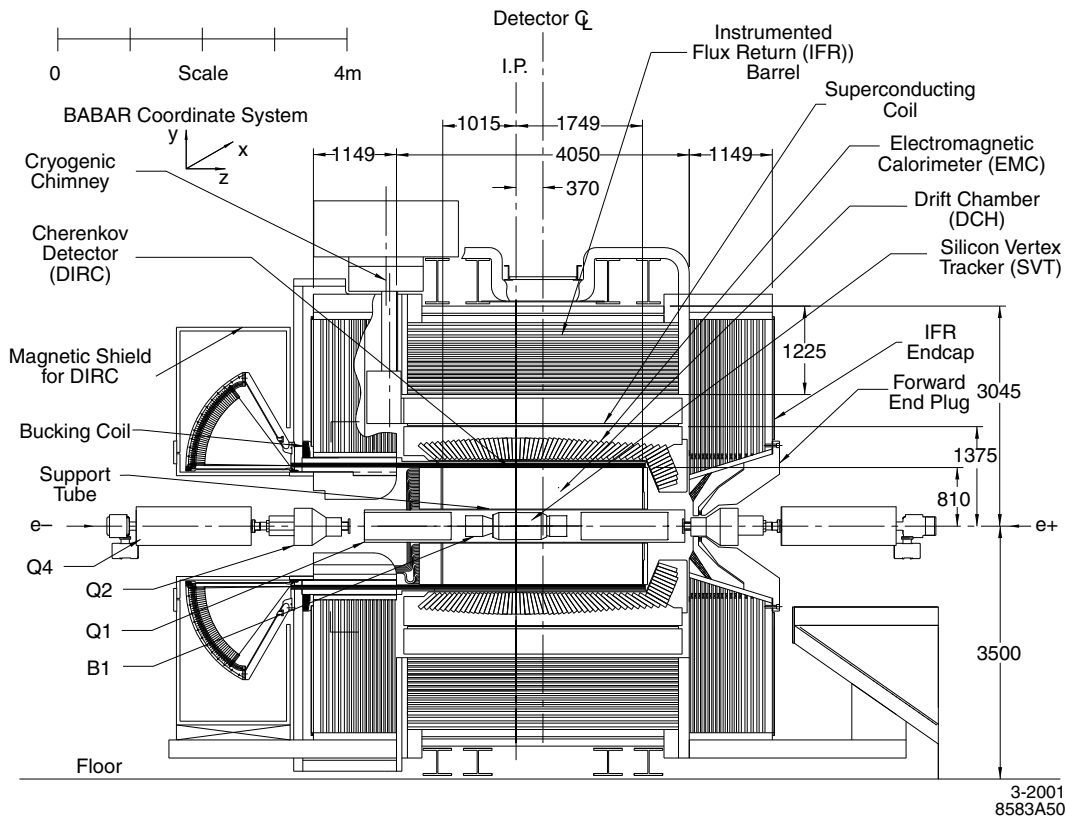


Figure 3.1: Longitudinal section through the *BABAR* detector [17]. All dimensions are given in mm.

A schematic view of the detector is shown in Figure 3.1. The detector is composed of a silicon vertex tracker (SVT), a drift chamber (DCH), a Cherenkov detector (DIRC), an electromagnetic calorimeter (EMC), a superconducting solenoid, and an instrumented flux return (IFR). These subsystems are described in the following sections.

3.2.1 Coordinate System

The *BABAR* coordinate system has its origin at the nominal interaction point (I.P.). The z -axis points in the flight direction of the electrons, which is also the direction of the boost of the center-of-mass frame with respect to the laboratory frame. It is known as the ‘forward direction.’ The y -axis points upwards and the x -axis points sideways in such a way that the coordinate system is right-handed.

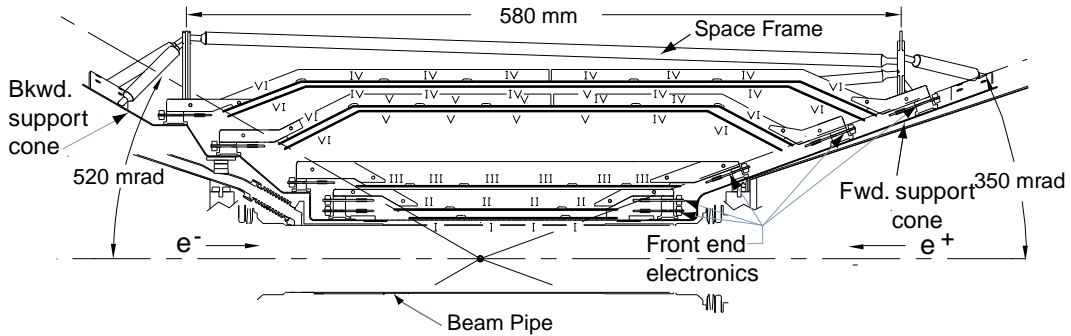


Figure 3.2: Top half of a longitudinal section through the silicon vertex tracker (SVT) [17].

3.2.2 The Silicon Vertex Tracker (SVT)

The purpose of the silicon vertex tracker is to facilitate the precise reconstruction of charged particle tracks and decay vertices close to the interaction region. To fully reconstruct B mesons, the vertex resolution must be better than $80\ \mu\text{m}$ along the z -axis and $100\ \mu\text{m}$ in the xy -plane. Since particles with a transverse momentum p_T below $120\ \text{MeV}/c$ are too slow to be reconstructed in the drift chamber, the measurement of the trajectories and the ionization loss dE/dx of these particles must be possible with the SVT alone.

The SVT is entirely contained within a support tube, which has an inner radius of $21.7\ \text{cm}$. The vertex detector is $58\ \text{cm}$ long and covers a polar angle from $350\ \text{mrad}$ from the beam line in forward direction to $520\ \text{mrad}$ from the beam line in backward direction. A schematic view is shown in Figure 3.2.

The SVT consists of five layers of double-sided silicon strip sensors. The inner three layers have a spatial resolution of $10 \sim 15\ \mu\text{m}$ for perpendicular tracks, while the resolution of the outer two layers is $40\ \mu\text{m}$. Each of the layers is organized into strips to measure the azimuthal angle ϕ , which run parallel to the beam axis, and strips to measure z , which run transverse to the beam axis. There are approximately 150 000 readout channels.

3.2.3 The Drift Chamber (DCH)

The drift chamber is designed for the precise reconstruction of the trajectories and momenta of charged particles. It also plays an important role for the identification of particles with low momenta (up to about $700\ \text{MeV}/c$), which is achieved with a measurement of the ionization loss dE/dx . In the extreme forward and backward directions, the drift chamber is the only device to provide information for the determination of particle masses.

The cylindrical chamber has an inner radius of $23.6\ \text{cm}$, an outer radius of

80.9 cm, and a length of 276.4 cm. It is composed of 7104 hexagonal drift cells, which have a size of 11.9 mm in radial direction and approximately 19.0 mm in azimuthal direction. The cells are arranged in 40 layers. Particles with transverse momenta above 180 MeV/ c pass all 40 layers.

The layers are divided into 10 superlayers, each consisting of four adjacent layers. The number of cells and wire orientation is identical in each layer of a superlayer. The wire orientation alternates between axial, stereo angle u , and stereo angle v , with axial wires in the innermost and the outermost superlayer. u and v have opposite signs; their values vary between ± 45 mrad and ± 76 mrad. The whole chamber has a 16-fold azimuthal symmetry.

Each drift cell contains one sense wire, which has a diameter of $20\ \mu\text{m}$ and is made of gold-plated tungsten-rhenium (WRe), surrounded by six field wires with a diameter of $120\ \mu\text{m}$, made of gold-plated aluminum (Al). While the field wires are at ground potential, a voltage of nominally 1960 V is applied to the sense wires.

The chamber uses a helium-based gas mixture, composed of 80% helium (He) and 20% isobutane (C_4H_{10}). This mixture has a radiation length of 807 m and a drift velocity (without magnetic field) of $22\ \mu\text{m}/\text{ns}$.

3.2.4 The Detector of Internally Reflected Cherenkov Light (DIRC)

The purpose of the detector of internally reflected Cherenkov light (DIRC) is the identification of charged particles. A good separation of K^\pm and π^\pm is important for the flavor-tagging of the B meson, as well as to be able to distinguish the rare decays $B^0 \rightarrow \pi^+\pi^-$ and $B^0 \rightarrow K^+\pi^-$. Additionally, the amount of material placed in front of the electromagnetic calorimeter is to be minimized, so that the measurement of neutral particles is disturbed as little as possible. The DIRC achieves these goals by separating the Cherenkov light production from the measurement. The design is shown schematically in Figure 3.3.

144 rectangular bars, made of synthetic, fused silica, form the active region of the detector. Each bar is 35 mm wide, 17 mm thick, and 4.9 m long. Groups of 12 bars are placed into hermetically sealed containers, called bar boxes, which are made of thin aluminum. Within each box, the bars are separated by $150\ \mu\text{m}$ air gaps. Figure 3.4 shows a schematic view of a bar box.

The DIRC surrounds the drift chamber and occupies 80 mm of radial space. The active region covers about 94% of the azimuth.

Particles passing through the silica, which has an index of refraction of $n = 1.473$, produce a light cone with a Cherenkov angle θ_C following the relation $\cos \theta_C = 1/\beta n$ ($\beta = v/c$ representing the velocity of the particle). A fraction of the Cherenkov photons is internally reflected within the bars, and since the forward ends are equipped with mirrors, all internally reflected photons are directed to the backward ends, irrespective of their original flight direction. This light transport mechanism preserves the magnitude of the Cherenkov angle.

At the backward end, the photons are directed into a container of stainless steel, known as the standoff box, which is located outside of the BABAR detector. It is

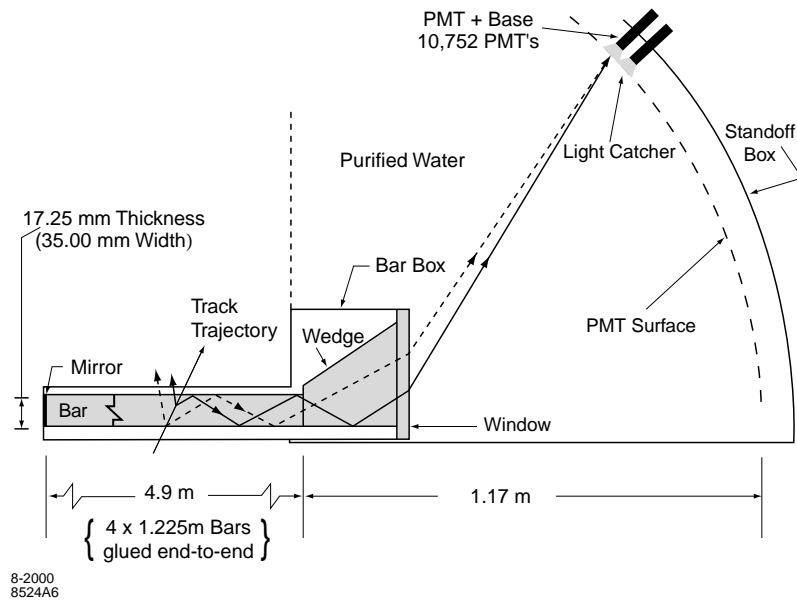


Figure 3.3: Schematic view of the DIRC [17].

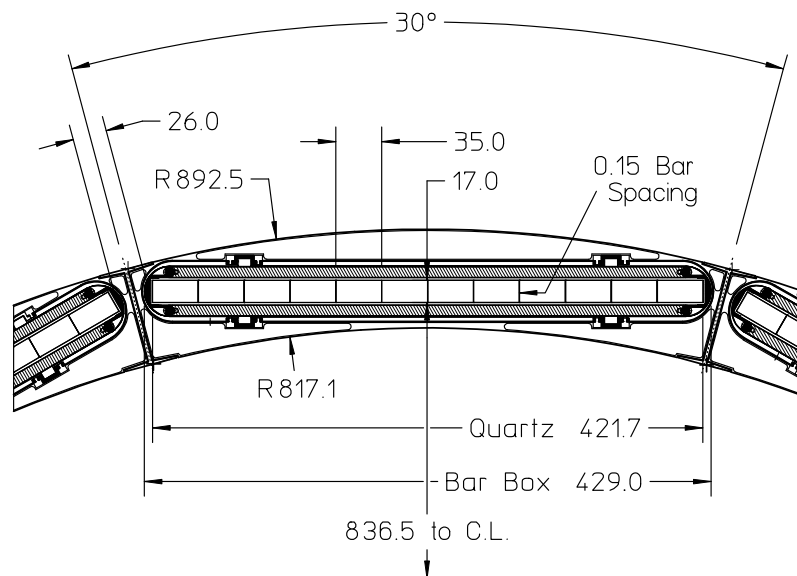


Figure 3.4: Transverse section through a DIRC bar box [17]. All dimensions are given in mm.

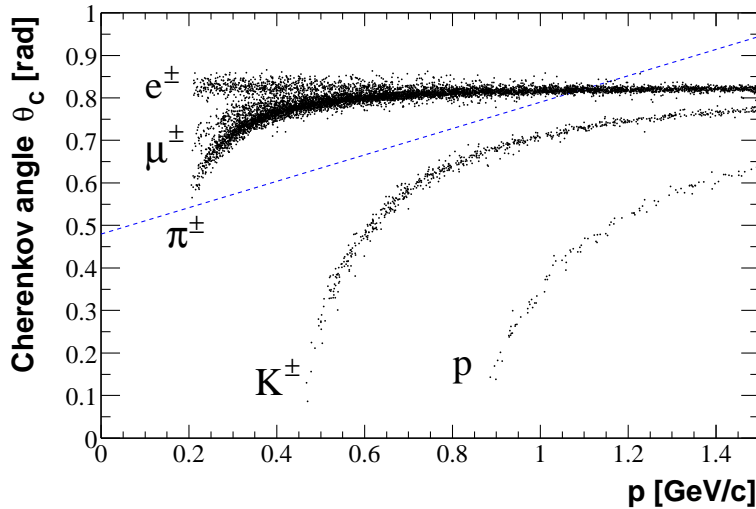


Figure 3.5: Cherenkov angle θ_C vs. momentum p . Each dot corresponds to a track in a sample of 5 000 events. The region above the dotted line is excluded by the K^\pm selector; see Section 4.2 for details.

filled with 6 000 liters of purified water. The rear of the standoff box is instrumented with 10 752 photomultiplier tubes (PMTs) with 29 mm diameter, which are closely packed inside the water volume. This results in about 90% of the rear surface being active for light collection. The PMTs are about 1.2 m away from the bar ends.

Measurement of the positions and arrival times of the PMT signals allows the reconstruction of the Cherenkov angles as well as an association of the light cones with tracks. Figure 3.5 shows a plot of the Cherenkov angle θ_C vs. the momentum p , where electrons, muons, pions, kaons, and protons correspond to different ‘bands’. As can be seen, kaons are very well separated from pions and leptons in the accessible momentum region.

The DIRC has an angular resolution of 10.2 mrad and a time resolution of 1.7 ns for single Cherenkov photons. This results in a track Cherenkov angle resolution of 2.5 mrad for di-muon events, which is close to the design goal of 2.2 mrad. The mean efficiency of kaons selected with the DIRC is $96.2 \pm 0.2\%$, and $2.1 \pm 0.1\%$ of the pions are misidentified as kaons.

3.2.5 The Electromagnetic Calorimeter (EMC)

The electromagnetic calorimeter is designed to measure electromagnetic showers with high efficiency to allow the reconstruction of π^0 and η mesons, as well as the detection of single photons with excellent angular and energy resolution. Additionally, it plays an important role for the identification of electrons and for the

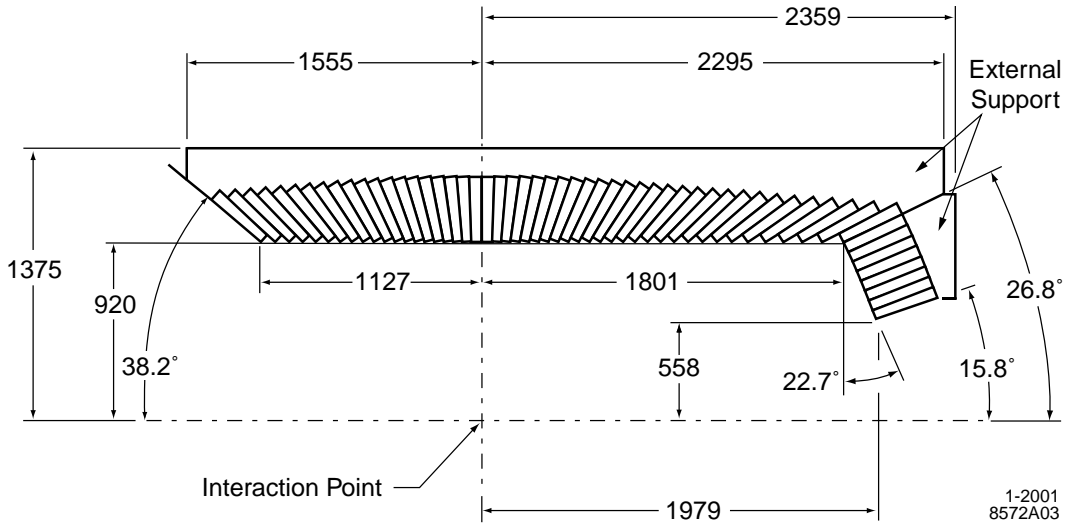


Figure 3.6: Top half of a longitudinal section through the electromagnetic calorimeter (EMC) [17]. All dimensions are given in mm.

separation of electrons from charged pions.

The calorimeter is made of 6580 thallium-doped cesium iodide (CsI(Th)) crystals, which are grouped into a barrel region and an endcap region. The barrel, which has an inner radius of 920 mm, encompasses 48 axially symmetric rings of 120 crystals each. The crystals are arranged to have a small polar dip angle, i.e., the center axis of each crystal does not point exactly to the interaction point. This prevents an acceptance loss which would otherwise result from the fact that the crystals are separated by about $700\ \mu\text{m}$ of wrapping and support structure material.

The conical endcap, which is positioned adjacent to the forward end of the barrel, is also axially symmetric. It is composed of three rings of 120 crystals, three rings of 100 crystals, and two rings of 80 crystals.

The calorimeter extends in polar angle from 15.8° to 141.8° , which corresponds to a 90% solid-angle coverage in the center-of-mass frame. A schematic view is shown in Figure 3.6.

The geometry of the calorimeter requires a trapezoidal crystal shape (Figure 3.7). The height of the crystals varies between 29.76 cm and 32.55 cm, the front face area varies between $19.13\ \text{cm}^2$ and $23.13\ \text{cm}^2$, and the back face area varies between $25.19\ \text{cm}^2$ and $39.90\ \text{cm}^2$ [11].

The thallium-doped cesium iodide has a radiation length of 1.85 cm and a light yield of about 50 000 photons per MeV of deposited energy. The scintillation light spectrum peaks at a wavelength of 565 nm. Two photo diodes and pre-amplifiers are attached to the back face of each crystal. This redundancy makes it possible to read out a channel even if a single diode or pre-amplifier has failed.

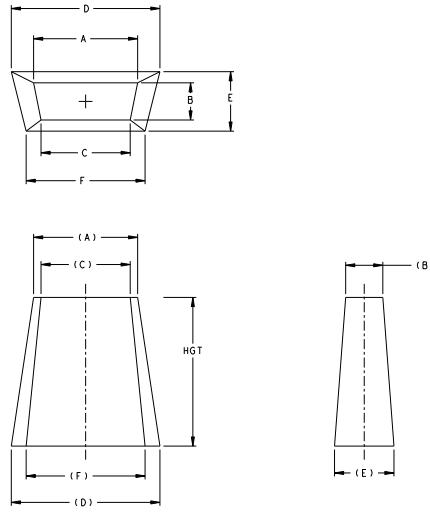


Figure 3.7: Shape of the calorimeter crystals [11].

In order to fulfill the stringent resolution requirements, various calibration and monitoring mechanisms are in place. To test and calibrate the readout electronics, it is possible to inject a defined charge into the pre-amplifier input. The single crystal deposited energy is calibrated at opposite ends of the dynamic range and interpolated in between. For the low energy calibration, activated Fluorinert is pumped through a system of thin aluminum pipes which run in front of the crystals. The reaction $^{16}\text{N} \rightarrow ^{16}\text{O}^* + \beta$, $^{16}\text{O}^* \rightarrow ^{16}\text{O} + \gamma(6.13 \text{ MeV})$ provides a calibration point at 6.13 MeV. For the high energy calibration, the known kinematics of Bhabha events ($e^+e^- \rightarrow e^+e^-$) is exploited to obtain a calibration point in the range of 3 ~ 9 GeV, with a well-defined relation between polar angle and e^\pm energy. Furthermore, a correction on the energy of clusters, which encompass more than one crystal, is needed to account for shower leakage. It is derived from π^0 decays.

To monitor the light response of individual crystals, a light-pulsar systems allows to inject light pulses from a xenon flash-lamp into each crystal through optical fibers. The intensity of the pulses is itself monitored with a reference system, which is calibrated with two radioactive sources, ^{241}Am and ^{148}Gd .

Both the energy resolution σ_E/E and the angular resolutions σ_θ , σ_ϕ of the calorimeter depend on the energy. They are given by the following formulas:

$$\begin{aligned} \sigma_E/E &= \frac{(2.32 \pm 0.30)\%}{\sqrt[4]{E/1 \text{ GeV}}} \oplus (1.85 \pm 0.12)\%; \\ \sigma_\theta = \sigma_\phi &= \frac{(3.87 \pm 0.07) \text{ mrad}}{\sqrt{E/1 \text{ GeV}}} + (0.00 \pm 0.04) \text{ mrad}. \end{aligned} \quad (3.1)$$

3.2.6 The Solenoid Magnet

The electromagnetic calorimeter is surrounded by a superconducting solenoid coil with a mean radius of 153 cm, which is embedded in a cryostat system with an inner radius of 142 cm and a length of 385 cm. The coil operates at a current of 4 596 A, resulting in a magnetic field of 1.5 T which stores 27 MJ of energy.

3.2.7 The Instrumented Flux Return (IFR)

The magnetic flux of the solenoid is returned in steel plates which are instrumented with resistive plate chambers (RPCs). This system, called instrumented flux return (IFR), is used to identify muons and detect neutral hadrons (primarily K_L^0 mesons and neutrons).

The flux return consists of a barrel, a forward and a backward endcap, all of which have a hexagonal cross-section. The thickness of the steel plates varies from 2 cm for the innermost to 10 cm for the outermost plates. The gap between the plates is 3.5 cm in the inner barrel region and 3.2 cm elsewhere. There are 19 layers of RPCs in the barrel, 18 layers in each endcap, and 2 layers of cylindrical RPCs between the electromagnetic calorimeter and the cryostat. The total number of 806 RPCs covers an active area of about 2 000 m².

The RPCs are made of two 2 mm thick bakelite (phenolic polymer) sheets, which have a high resistivity of $10^{11} \sim 10^{12} \Omega \text{ cm}$, and which are separated by a 2 mm gap. The volume between the sheets is filled with a gas mixture, consisting nominally of 56.7% argon, 38.8% 1,1,1,2-tetrafluoroethane ('Freon 134a'), and 4.5% isobutane. The exterior surfaces of the bakelite sheets are coated with graphite, and a voltage of 8 kV is applied between the two graphite layers. Spark discharges are read out by aluminum strips on both sides of the chambers, which have varying lengths up to 423 cm and widths between 1.97 cm and 3.85 cm. This results in a total number of almost 53 000 readout channels.

3.3 Run Periods and Luminosity

As has been explained in Section 3.1, the excitation of the $\Upsilon(4S)$ resonance requires a collision energy of $\sqrt{s} = 10.58 \text{ GeV}$. The integrated luminosity recorded in this mode, which is called 'on-peak', amounts to 163.24 fb^{-1} (until March 2004). Additionally, *BABAR* operates at a collision energy 40 MeV below the $\Upsilon(4S)$ resonance for a fraction of the time to facilitate background studies. In this mode, called 'off-peak', 17.27 fb^{-1} of data have been recorded. Figure 3.8 shows the integrated luminosities at different times.

The highest peak luminosity which PEP-II achieved until March 2004 is $8.16 \times 10^{33} \text{ cm}^{-2}\text{s}^{-1}$, which considerably exceeds the design luminosity of $3 \times 10^{33} \text{ cm}^{-2}\text{s}^{-1}$.

Since the error of the analysis presented in this dissertation is dominated by systematic uncertainties, only data from the first two periods of data taking, known

2004/03/22 09.20

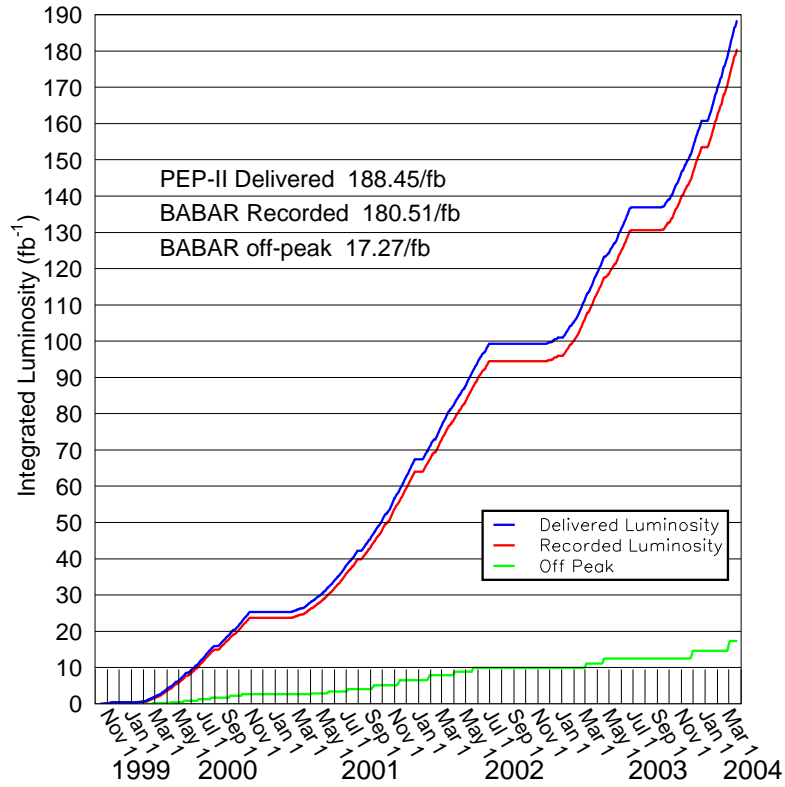


Figure 3.8: Integrated luminosity delivered by PEP-II and recorded by *BABAR* vs. time.

as ‘Run 1’ and ‘Run 2’, have been used. Run 1 encompasses October 1999 to October 2000, while Run 2 includes February 2001 to June 2002.

Chapter 4

Measurement of $\Gamma(D_s^{*+} \rightarrow D_s^+ \pi^0) / \Gamma(D_s^{*+} \rightarrow D_s^+ \gamma)$

4.1 Overview

For a reconstruction of the decays $D_s^{*+} \rightarrow D_s^+ \pi^0$ and $D_s^{*+} \rightarrow D_s^+ \gamma$, a clear D_s^+ signal is required. The decay chain $D_s^+ \rightarrow \phi \pi^+$, $\phi \rightarrow K^+ K^-$ has the best signal-to-background ratio [18], therefore this decay chain has been chosen for the D_s^+ reconstruction. $D_s^+ \rightarrow \phi \pi^+$ has a branching fraction of $(3.6 \pm 0.9)\%$ and $\phi \rightarrow K^+ K^-$ has a branching fraction of $(49.2 \pm_{-0.7}^{+0.6})\%$ [3].

π^0 candidates are reconstructed in the channel $\pi^0 \rightarrow \gamma\gamma$. Since the same set of D_s^+ candidates is used for the $D_s^{*+} \rightarrow D_s^+ \pi^0$ as for the $D_s^{*+} \rightarrow D_s^+ \gamma$ decay channel, systematic uncertainties in the D_s^+ reconstruction cancel out when the partial widths ratio $\Gamma(D_s^{*+} \rightarrow D_s^+ \pi^0) / \Gamma(D_s^{*+} \rightarrow D_s^+ \gamma)$ is calculated.

Various selection criteria, which are described in detail in the following sections, have been applied to obtain $D_s^{*+} \rightarrow D_s^+ \pi^0$ and $D_s^{*+} \rightarrow D_s^+ \gamma$ signals. Unless stated otherwise, these criteria have been optimized to maximize the signal efficiency of the $D_s^{*+} \rightarrow D_s^+ \pi^0$ channel, i.e., the function $S^2 / (S + B)$ has been maximized. S and B correspond to the expected number of signal events and background events in the signal region, respectively, according to a $D_s^{*+} \rightarrow D_s^+ \pi^0$ signal obtained from generic Monte Carlo events.

4.1.1 Data and Monte Carlo Sets

For the inclusive reconstruction of $D_s^{*+} \rightarrow D_s^+ \pi^0$ and $D_s^{*+} \rightarrow D_s^+ \gamma$, off-peak and on-peak data can be used alike. Of the 93.80 fb^{-1} of data recorded during Run 1 and Run 2, 91.46 fb^{-1} are available to be used in analyses.

This analysis is based on 90.40 fb^{-1} . The remaining 1.06 fb^{-1} correspond to a running period during which the electromagnetic calorimeter was miscalibrated. Since the efficient identification of neutral particles is crucial for this analysis, the data from this period have explicitly been excluded.

	Run 1	Run 2	Run 1 + Run 2
Off-Peak	2.60 fb ⁻¹	6.98 fb ⁻¹	9.58 fb ⁻¹
On-Peak	20.73 fb ⁻¹	60.09 fb ⁻¹	80.82 fb ⁻¹
Off-Peak + On-Peak	23.33 fb ⁻¹	67.07 fb ⁻¹	90.40 fb ⁻¹

Table 4.1: Data sets used in the analysis presented in this dissertation. The numbers have a systematic uncertainty of 0.5% or better [19].

Table 4.1 gives an overview of the data sets which have been used.

Since the start of the *BABAR* experiment, 573 569 600 generic Monte Carlo events have been generated in the four channels (referred to as ‘Monte Carlo types’)

- $e^+e^- \rightarrow \Upsilon(4S) \rightarrow B^0\bar{B}^0$,
- $e^+e^- \rightarrow \Upsilon(4S) \rightarrow B^+B^-$,
- $e^+e^- \rightarrow c\bar{c}$, and
- $e^+e^- \rightarrow u\bar{u}/d\bar{d}/s\bar{s}$.

During the generation of each Monte Carlo event, the detector conditions of a specific month of data taking have been simulated, so that changing conditions are taken into account. The detector background has not been simulated, but measured background has been mixed into the Monte Carlo events. This has been achieved with a ‘random trigger’, a system which triggers the read-out of the detector at random times.

Table 4.2 lists the numbers of Monte Carlo events of the different Monte Carlo types and run periods. A scale factor has been applied to each event, so that the scaled number of Monte Carlo events corresponds to the expected number of data events. For the $e^+e^- \rightarrow u\bar{u}/d\bar{d}/c\bar{c}/s\bar{s}$ channels, this number has been calculated as the product of the integrated luminosities in Table 4.1 and the corresponding cross-sections which have been obtained from [16] and are shown in Table 3.1. The number of $B\bar{B}$ pairs are measured by comparing the cross-sections of multi-hadron events, normalized to the $e^+e^- \rightarrow \mu^+\mu^-$ cross-sections, in on-peak and off-peak data [20]. This method yields, respectively, $22\,325\,255 \pm 245\,839$ and $65\,399\,735 \pm 719\,660$ $B\bar{B}$ events in the Run 1 and Run 2 data sets used in this analysis.

In addition to generic Monte Carlo, signal Monte Carlo events are used. For each of the channels $D_s^{*+} \rightarrow D_s^+\pi^0$, $D_s^{*+} \rightarrow D_s^+\gamma$, $D^{*0} \rightarrow D^0\pi^0$, and $D^{*0} \rightarrow D^0\gamma$, 30 000 events have been generated.

Run	Monte Carlo type	Number of events	Scale factor
Run 1	$B^0 \bar{B}^0$	27 693 600	0.403
	$B^+ B^-$	27 356 000	0.408
	$c\bar{c}$	36 452 000	0.832
	$u\bar{u}/d\bar{d}/s\bar{s}$	60 491 000	0.806
Run 2	$B^0 \bar{B}^0$	73 479 100	0.445
	$B^+ B^-$	76 558 000	0.427
	$c\bar{c}$	106 595 900	0.818
	$u\bar{u}/d\bar{d}/s\bar{s}$	164 944 000	0.850

Table 4.2: Generic Monte Carlo event sets used in the analysis presented in this dissertation. The events have been scaled to match the number of events in the data.

4.2 Charged Particle Identification

Charged particles are identified by their trajectories in the silicon vertex tracker and the drift chamber. Tracks are fitted to the hits in these two subsystems and these tracks are then extrapolated. The point in space where the extrapolation of a track is closest to the interaction point is referred to as the ‘point of closest approach’ (‘POCA’); the distance between the POCA and the interaction point is called the ‘distance of closest approach’ (‘DOCA’).

To be considered for this analysis, charged particle tracks must fulfill the following criteria:

- Momentum $p < 10 \text{ GeV}/c$;
- Track fit probability $P_{\text{track}}(\chi^2) > 0$;
- Transverse momentum $p_T > 100 \text{ MeV}/c$;
- Number of hits in the drift chamber ≥ 12 ;
- DOCA in the xy -plane $< 1.5 \text{ cm}$;
- DOCA in z direction $< 10 \text{ cm}$.

Figure 4.1(a) shows the momentum spectrum of the tracks.

The product of efficiency ϵ and acceptance A varies with the multiplicity of the event and high voltage setting of the drift chamber. For events with low multiplicity, it is of the order of $85\% < \epsilon A < 88\%$. This is only slightly less than the ϵA of all identified tracks, which is of the order of $89\% < \epsilon A < 92\%$ [21].

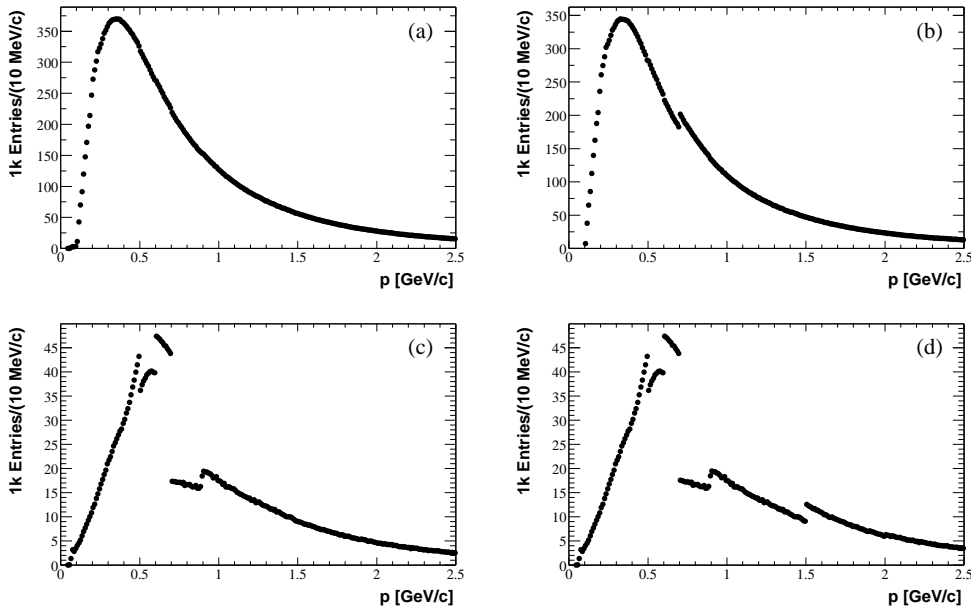


Figure 4.1: Momentum spectrum of (a) tracks, (b) π^\pm candidates, (c) *tight* K^\pm candidates, (d) *loose* K^\pm candidates, based on a 0.9 fb^{-1} subsample of the data. The discontinuities in the kaon spectra correspond to momenta where the selector switches criteria; see text for details.

4.2.1 Kaon Identification

Charged kaons are identified with a likelihood selector which combines measurements of the silicon vertex tracker, the drift chamber, and the DIRC [22].

The measurement of dE/dx allows a better than 2σ π^\pm/K^\pm separation for momenta of up to 600 MeV/c in the SVT and momenta of up to 700 MeV/c in the DCH (see Figure 4.2). While dE/dx in principle follows the Bethe-Bloch formula, a phenomenological parameterization which includes calibration constants is used.

Under the assumption that dE/dx follows a Gaussian distribution with well-known width σ , the probability density function (PDF) g_i for a particular particle hypothesis i with an expected ionization loss $(dE/dx)_i$ can be calculated in the following way:¹

$$g_i = \frac{1}{\sqrt{2\pi}\sigma} \exp\left(-\frac{(dE/dx - (dE/dx)_i)^2}{2\sigma^2}\right), \quad i \in \{e^\pm, \mu^\pm, \pi^\pm, K^\pm, p\}. \quad (4.1)$$

This is done separately for the SVT and the DCH, so that each subsystem yields a likelihood for each of the five particle hypotheses.

¹ dE/dx as well as σ are functions of the momentum p .

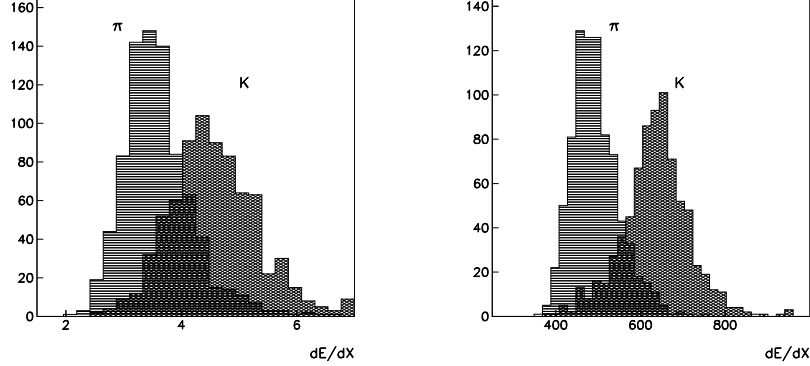


Figure 4.2: dE/dx distribution for pions and kaons in the momentum range $500 < p < 600 \text{ MeV}/c$ measured in the SVT (left) and DCH (right). The pions and kaons are obtained from a very pure D^* decay sample [22].

Kaons with momenta above

$$p > \frac{m_{K^\pm}}{\sqrt{n^2 - 1}} \approx 460 \text{ MeV}/c \quad (4.2)$$

emit Cherenkov light in the silica bars of the DIRC (index of refraction $n = 1.473$). While the Cherenkov angle θ_C is described by

$$\cos \theta_C = \frac{1}{\beta n}, \quad \beta = \frac{p}{E}, \quad (4.3)$$

the expected number of Cherenkov photons N_i depends on the particle type, charge, momentum, polar angle, and bar number. It is obtained from a lookup table.

The DIRC likelihood is the normalized product of a Gaussian probability g_i , based on the measurement of the Cherenkov angle θ_C , and a Poisson probability p_i , based on the number of signal photons N and the number of background photons N_b :

$$p_i = \frac{(N_i + N_b)^{N+N_b}}{(N + N_b)!} e^{-(N_i+N_b)}, \quad i \in \{e^\pm, \mu^\pm, \pi^\pm, K^\pm, p\}. \quad (4.4)$$

Below the Cherenkov threshold of protons ($p \approx 880 \text{ MeV}/c$), a constant probability of 0.2 is assigned to the proton hypothesis.

An overall likelihood ℓ_i is calculated for each particle hypothesis by multiplying the subsystem likelihoods, but each subsystem is considered only in certain momentum domains. Specifically,

- the SVT likelihood is used if $25 < p < 700 \text{ MeV}/c$ or $p > 1.5 \text{ GeV}/c$;
- the DCH likelihood is used if $90 < p < 700 \text{ MeV}/c$ or $p > 1.5 \text{ GeV}/c$;

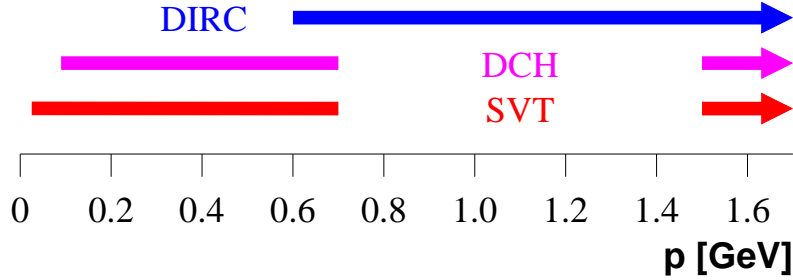


Figure 4.3: Momentum domains in which the SVT, DCH, and DIRC likelihoods are considered for charged kaon identification.

- the DIRC likelihood is used if $p > 600 \text{ MeV}/c$.

The momentum domains are depicted in Figure 4.3.

The selection of kaons is based on likelihood ratios. Of the various modes supported by the selector, two are used in this analysis. They are referred to as *tight* and *loose*. The *tight* mode is optimized to keep the misidentification rate below 5% for momenta up to $4 \text{ GeV}/c$. It applies the following criteria:

- The SVT and DCH are disregarded if $p > 1.5 \text{ GeV}/c$. Only the DIRC likelihood is used for high momenta.
- $\ell_{K^\pm}/\ell_{\pi^\pm} > 1$ if $p < 500 \text{ MeV}/c$ and $0.7 < p < 2.7 \text{ GeV}/c$;
- $\ell_{K^\pm}/\ell_{\pi^\pm} > 15$ if $500 < p < 700 \text{ MeV}/c$;
- $\ell_{K^\pm}/\ell_{\pi^\pm} > 80$ if $p > 2.7 \text{ GeV}/c$;
- $\ell_{K^\pm}/\ell_p > 1$;
- $\theta_C(p) < \left(\frac{310}{1 \text{ MeV}/c} p + 0.48 \right) \text{ rad}$.

The last criterion excludes the region above the dotted line in Figure 3.5, which contains slow leptons and pions.

The *loose* mode keeps the misidentification rate below 7% for momenta up to $4 \text{ GeV}/c$ and improves the efficiency at momenta above $1.5 \text{ GeV}/c$. The same selection criteria as for the *tight* mode are applied, but the SVT and DCH are taken into account for $p > 1.5 \text{ GeV}/c$ (as well as for $p < 700 \text{ MeV}/c$).

Figures 4.1(c) and (d) show the momentum spectra of *tight* and *loose* kaons, respectively. The discontinuities in the spectra can be understood in terms of the subsystems used and the required $\ell_{K^\pm}/\ell_{\pi^\pm}$ likelihood ratio:

- $p < 0.5 \text{ GeV}/c$: SVT, DCH, $\ell_{K^\pm}/\ell_{\pi^\pm} > 1$;

- $0.5 < p < 0.6 \text{ GeV}/c$: SVT, DCH, $\ell_{K^\pm}/\ell_{\pi^\pm} > 15$;
- $0.6 < p < 0.7 \text{ GeV}/c$: SVT, DCH, DIRC, $\ell_{K^\pm}/\ell_{\pi^\pm} > 15$;
- $0.7 < p < 1.5 \text{ GeV}/c$: DIRC, $\ell_{K^\pm}/\ell_{\pi^\pm} > 1$;
- $1.5 < p < 2.7 \text{ GeV}/c$: SVT, DCH (*loose mode only*), DIRC, $\ell_{K^\pm}/\ell_{\pi^\pm} > 1$;

The discontinuity at $p \approx 880 \text{ MeV}/c$ is caused by the proton Cherenkov threshold.

4.2.2 Pion Identification

Due to the large number of charged pions per event, no attempt is made to actively identify them. However, charged particle tracks which have been identified as *tight* kaons are vetoed in order to reduce the combinatoric background under the D_s^+ signal. All charged particles which have not been identified as *tight* kaons are considered as π^\pm candidates.

The momentum spectrum of the π^\pm candidates is shown in Figure 4.1(c).

4.3 Energy Measurement

Energy which is deposited in the calorimeter usually spreads over several adjacent crystals, making it necessary to deploy pattern recognition algorithms to determine energies and impact points [17].

Regions of adjacent crystals into which an electromagnetic shower has spread are known as ‘clusters’. More specifically, a cluster must contain at least one ‘seed’ crystal with an energy above 10 MeV. Surrounding crystals with an energy of at least 1 MeV are considered a part of the same cluster, as are crystals for which at least one neighbor (including corners) has an energy above 3 MeV.

If two or more particles hit the calorimeter with little spatial distance, the electromagnetic showers caused by the energy deposits can merge into a single cluster. It is therefore necessary to split clusters with more than one local energy maximum into what is referred to as ‘bumps’. To be considered a local maximum, a crystal is required to exceed the energy of each of its neighbors, and additionally its energy E must satisfy the condition $E/E_N < 0.5(N - 2.5)$, where N is the number of neighboring crystals with an energy above 2 MeV and E_N is the highest energy of any of these N crystals.

For single bump clusters, the energy of the bump is simply the sum of the energies of the crystals in the cluster, while for multiple bump clusters, the energy of the bumps is determined by an iterative algorithm. A weight

$$w_i = E_i \frac{\exp(-2.5r_i/r_M)}{\sum_{j \in \text{cluster}} E_j \exp(-2.5r_j/r_M)} \quad (4.5)$$

is assigned to each crystal i in the cluster, where r_i is the distance from the centroid of the bump and $r_M = 3.8 \text{ cm}$ is the Molière radius of CsI(Th). Initially, all weights

are set to 1, and then the process is iterated using the previous w_i to determine the centroid position, until the centroid position is stable within 1 mm. The energy of the bump is then calculated as

$$E_{\text{bump}} = \sum_{i \in \text{cluster}} w_i E_i. \quad (4.6)$$

The bump position is defined as the center-of-gravity of the logarithmic weights

$$W_i = 4.0 + \ln \frac{E_i}{E_{\text{bump}}}. \quad (4.7)$$

Only crystals with positive weights $W_i > 0$ are taken into account. This method emphasizes lower-energy crystals, while neglecting peripheral crystals. The polar non-projectivity of the crystals causes a systematic bias, which is corrected by an offset of -2.6 mrad for $\theta > 90^\circ$ and $+2.6$ mrad for $\theta < 90^\circ$.

Each bump with a position that is consistent with an extrapolated charged track is associated with that track. The remaining bumps are assumed to originate from neutral particles.

4.4 D_s^+ Reconstruction

As described in Section 4.1, D_s^+ candidates are reconstructed in the decay chain $D_s^+ \rightarrow \phi\pi^+$, $\phi \rightarrow K^+K^-$. First of all, each positively charged kaon candidate K^+ is combined with each negatively charged kaon candidate K^- . The combination is only considered further if one of the kaons fulfills the *tight* criteria, while the other kaon must fulfill the *loose* criteria. Figure 4.4 shows the distribution of the invariant K^+K^- mass. ϕ candidates are selected according to the following criterion:

$$|m_{K^+K^-} - m_\phi| < 8 \text{ MeV}/c^2, \quad (4.8)$$

where $m_{K^+K^-}$ is the measured K^+K^- invariant mass and $m_\phi = 1019.456 \text{ MeV}/c^2$ is the known ϕ mass [3].

The ϕ are then combined with π^+ candidates (see Section 4.2.2). A vertex fit is applied to these combinations, and only those candidates are retained for which the fit does not fail, i.e., for which the fit probability is greater than zero:

$$P_{\text{vertex}}(\chi^2) > 0. \quad (4.9)$$

To be accepted as D_s^+ candidates, the $\phi\pi^+$ combinations must fulfill a number of additional criteria, described in the following sections.

4.4.1 Helicity Distribution

The D_s^+ is a pseudoscalar meson ($J^P = 0^-$), as is the π^+ . However, the ϕ is a vector meson ($J^P = 1^-$). When the D_s^+ meson decays to a pion and a ϕ meson, the spin

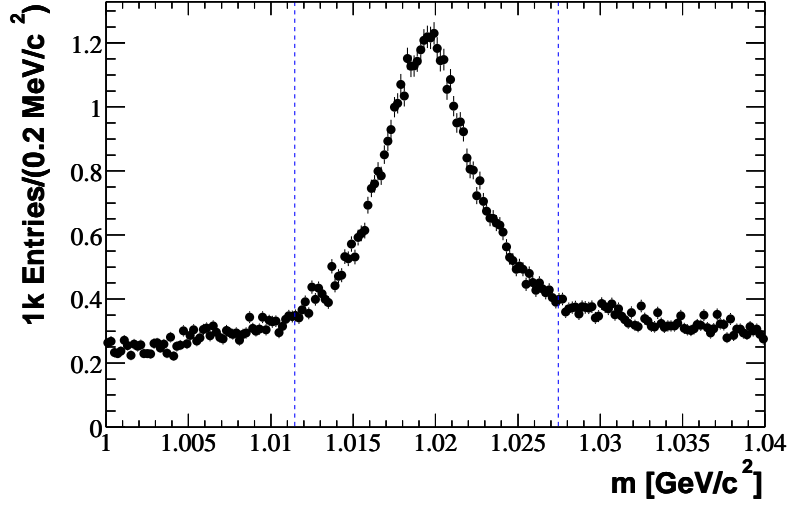


Figure 4.4: K^+K^- invariant mass distribution, based on a 0.9 fb^{-1} subsample of the data. The candidates between the vertical dotted lines are selected as ϕ candidates.

of the latter is compensated by the angular momentum of the $\phi\pi^+$ system, which must be perpendicular to the ϕ momentum direction (as well as the π^+ momentum direction) in the D_s^+ rest frame. The ϕ meson is therefore polarized.

When the polarized ϕ meson decays to two kaons, the momentum direction of the kaons in the ϕ rest frame shows a characteristic angular distribution with respect to the ϕ momentum direction in the D_s^+ rest frame. To describe this behavior, the helicity angle θ_H is defined as the angle between the ϕ momentum direction in the D_s^+ rest frame and the momentum direction of the positively charged kaon K^+ in the ϕ rest frame, as illustrated by Figure 4.5. It is distributed proportionally to $\cos^2 \theta_H$, as shown in Figure 4.6.

There are two ways in which this can be exploited to discriminate $D_s^+ \rightarrow \phi\pi^+$ from background events, both of which this analysis follows alternatively. The first one is to require that the absolute value of $\cos \theta_H$ exceeds a certain value; this will be referred to as the ‘selection method’ in the following text. The criterion

$$|\cos \theta_H| > 0.3 \quad (4.10)$$

is chosen.

Due to this selection, a small number of signal events is lost; this is avoided by the ‘weighting method’ [23]: Instead of discarding some events, all events are retained and weighted with the normalized second Legendre polynomial

$$\bar{P}_2(x) = \frac{5}{2}P_2(x) = \frac{5}{4}(3x^2 - 1), \quad x = \cos \theta_H. \quad (4.11)$$

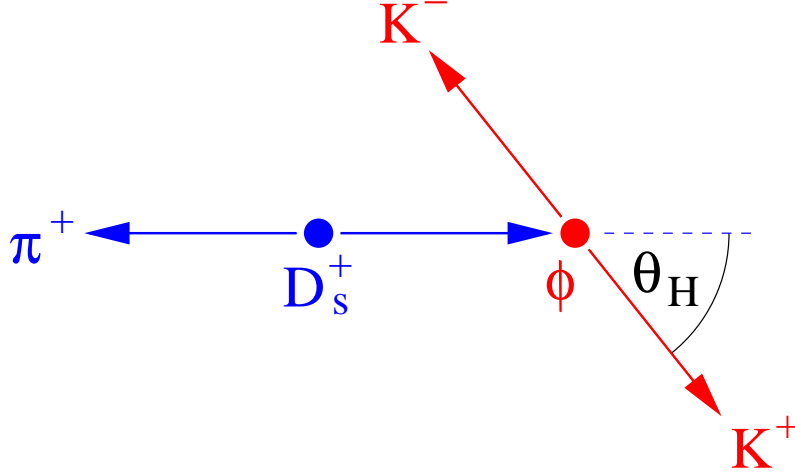


Figure 4.5: The helicity angle θ_H is the angle between the ϕ momentum direction in the D_s^+ rest frame and the K^+ momentum direction in the ϕ rest frame. The blue lines refer to directions in the D_s^+ rest frame, the red lines to directions in the ϕ rest frame.

The normalization factor $5/2$ in front of the second Legendre polynomial

$$P_2(x) = \frac{1}{2} (3x^2 - 1) \quad (4.12)$$

is chosen such that the yield of the $\cos^2 \theta_H$ distributed signal events is correctly produced when the events are weighted with $\bar{P}_2(\cos^2 \theta_H)$, i.e.,

$$\int_{-1}^1 dx \bar{P}_2(x) x^2 \Big/ \int_{-1}^1 dx x^2 = 1. \quad (4.13)$$

The Legendre polynomials obey the orthogonality relationship

$$\int_{-1}^1 dx P_n(x) P_m(x) = 0 \quad \text{if } n \neq m; \quad (4.14)$$

therefore, the weighting causes all parts of the background distribution not proportional to $P_2(\cos^2 \theta_H)$ (in an expansion in the Legendre polynomials) to vanish. Specifically, all background events are projected away in the ideal case of a flat ($\cos \theta_H$ independent) background distribution.

Figure 4.7 depicts the normalized second Legendre polynomial \bar{P}_2 .

4.4.2 D_s^+ Candidate Selection

When D_s^{*+} mesons are produced in the fragmentation of $e^+e^- \rightarrow c\bar{c}$ processes, the high momentum of the c quark causes the D_s^{*+} meson, and therefore also the D_s^+

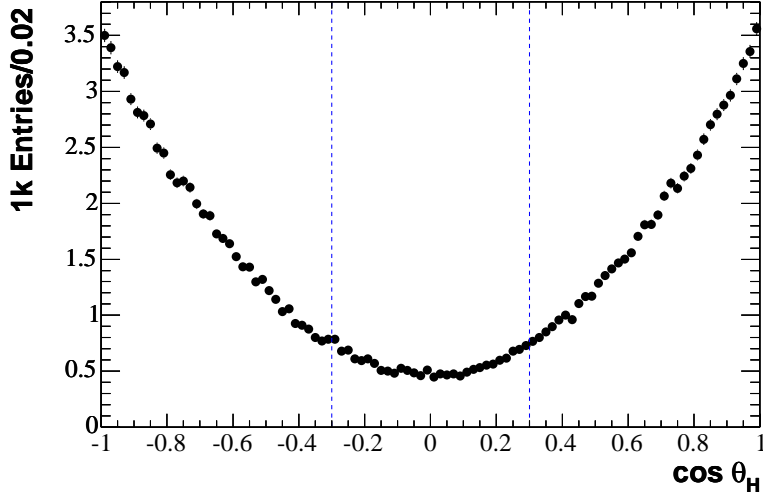


Figure 4.6: Distribution of the cosine of the helicity angle, $\cos \theta_H$, based on a 0.9 fb^{-1} subsample of the data. In addition to the selection criteria described in the text, $|m_{\phi\pi^+} - m_{D_s^+}| < 12 \text{ MeV}/c^2$ has been required. The candidates outside the vertical dotted lines are selected when the ‘selection method’ is used.

meson, to have a high momentum as well. To reduce the combinatoric background, D_s^+ candidates are therefore required to have a scaled momentum greater than 0.6:

$$x_p = p_{D_s^+}^* / \sqrt{E_{\text{beam}}^{*2} - m_{D_s^+}^2} > 0.6. \quad (4.15)$$

$p_{D_s^+}^*$ is the measured momentum of the D_s^+ candidate in the center-of-mass frame, E_{beam}^* is the energy of one beam in the center-of-mass frame (i.e., $\sqrt{s}/2$), and $m_{D_s^+}$ is the mass of the D_s^+ meson. $x_p = 0.6$ corresponds to a D_s^+ momentum of $\approx 2.9 \text{ GeV}/c$; this selection also removes all D_s^+ particles from B decays, for which the kinematic threshold is below $x_p = 0.6$.

Finally, the invariant mass $m_{\phi\pi^+}$ of the D_s^+ candidates must differ by less than $12 \text{ MeV}/c^2$ from the expected D_s^+ mass $m_{D_s^+}$:

$$|m_{\phi\pi^+} - m_{D_s^+}| < 12 \text{ MeV}/c^2. \quad (4.16)$$

For the generic Monte Carlo events, the known D_s^+ mass $m_{D_s^+} = 1968.5 \text{ MeV}/c^2$ [3] has been used as the expected value, while in the data, the mean D_s^+ mass comes out approximately $90 \text{ keV}/c^2$ below the mean Monte Carlo mass. This slight mass shift has been taken into account when selecting D_s^+ candidates in the data.

The $\phi\pi^+$ invariant mass distributions obtained with the selection and the weighting method from generic Monte Carlo events and data is shown in Figure 4.8.

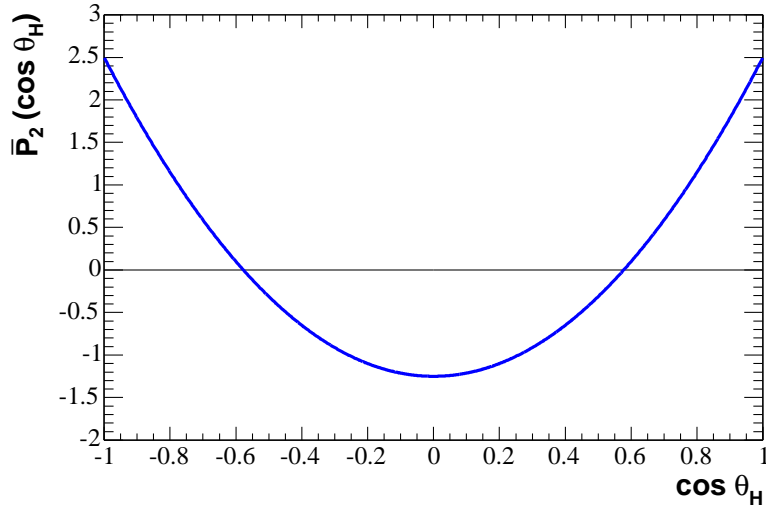


Figure 4.7: The normalized second Legendre polynomial $\bar{P}_2(\cos \theta_H) = 5/4(3 \cos^2 \theta_H - 1)$.

To determine the signal event yields, a binned maximum likelihood fit is used to fit a function to the data points. The function used is a sum of Gauss functions to model the signal and a third-order polynomial for the background:

$$f(x) = G_1(x) + G_2(x) + ax^3 + bx^2 + cx + d; \quad (4.17)$$

$$G_i(x) = \frac{N_i}{\sqrt{2\pi}\sigma_i} \exp\left(-\frac{(x - m_i)^2}{2\sigma_i^2}\right), \quad i \in \{1, 2\}.$$

The resulting parameters obtained for the signal shape and event yields are shown in Figure 4.3. The number of true (matched) Monte Carlo events has also been counted, so that this number can be compared with the event yield from the fit. The fit finds $68\,809 \pm 329$ signal events for the selection method, while 68 703 true events have been counted. For the weighting method, $71\,228 \pm 278$ signals are obtained from the fit, and 70 744 true events are found by counting.

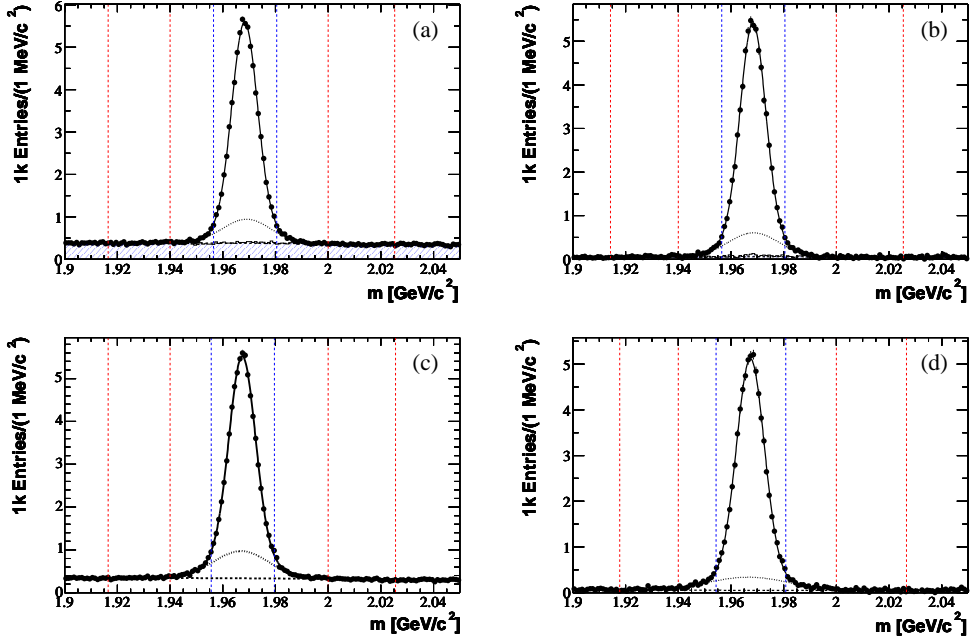


Figure 4.8: $\phi\pi^+$ invariant mass and fit functions: (a) generic Monte Carlo, selection method; (b) generic Monte Carlo, weighting method; (c) data, selection method; (d) data, weighting method. The hatched areas in the Monte Carlo diagrams correspond to background. The vertical dotted lines indicate the signal and sideband regions.

	Generic Monte Carlo	
	Selection Method	Weighting Method
N_1	$55\,753 \pm 2\,228$	$57\,941 \pm 1\,156$
m_1	$1968.279 \pm 0.037 \text{ MeV}/c^2$	$1968.302 \pm 0.028 \text{ MeV}/c^2$
σ_1	$4.758 \pm 0.073 \text{ MeV}/c^2$	$4.798 \pm 0.045 \text{ MeV}/c^2$
N_2	$13\,056 \pm 2\,136$	$13\,254 \pm 1\,109$
m_2	$1969.055 \pm 0.249 \text{ MeV}/c^2$	$1968.566 \pm 0.148 \text{ MeV}/c^2$
σ_2	$9.182 \pm 0.623 \text{ MeV}/c^2$	$9.597 \pm 0.305 \text{ MeV}/c^2$
$N = N_1 + N_2$	$68\,809 \pm 329$	$71\,228 \pm 278$
	Data	
	Selection Method	Weighting Method
N_1	$56\,792 \pm 1\,666$	$63\,344 \pm 512$
m_1	$1967.419 \pm 0.033 \text{ MeV}/c^2$	$1967.391 \pm 0.025 \text{ MeV}/c^2$
σ_1	$4.975 \pm 0.066 \text{ MeV}/c^2$	$5.288 \pm 0.032 \text{ MeV}/c^2$
N_2	$16\,725 \pm 1\,564$	$11\,005 \pm 409$
m_2	$1966.926 \pm 0.209 \text{ MeV}/c^2$	$1966.688 \pm 0.243 \text{ MeV}/c^2$
σ_2	$10.543 \pm 0.496 \text{ MeV}/c^2$	$15.298 \pm 0.455 \text{ MeV}/c^2$
$N = N_1 + N_2$	$73\,518 \pm 344$	$74\,349 \pm 304$

Table 4.3: Results of the fits to the $\phi\pi^+$ invariant mass distributions.

4.5 $\pi^0 \rightarrow \gamma\gamma$ Reconstruction

The selection of γ candidates to be used for π^0 reconstruction starts from a list of neutral candidates as described in Section 4.3. First of all,

$$E_\gamma > 45 \text{ MeV} \quad (4.18)$$

is required for the energy measured in the laboratory frame, which eliminates most neutral clusters which are not photons.

To further separate electromagnetic from hadronic showers in the calorimeter, the lateral energy distribution ‘*LAT*’ of each bump is considered. It is defined as

$$LAT = \frac{\sum_{i \geq 3} E_i r_i^2}{E_1 r_0^2 + E_2 r_0^2 + \sum_{i \geq 3} E_i r_i^2}. \quad (4.19)$$

E_i represents the energy deposited in the i th crystal after having sorted the crystals by deposited energy:

$$E_1 > E_2 > E_3 > \dots \quad (4.20)$$

r_i is the distance between the center of the i th crystal and the bump position as defined by Equation 4.7; $r_0 = 5 \text{ cm}$ is a measure of the distance between two crystals.

For electromagnetic showers, most of the energy is typically contained in two to three crystals, while hadronic showers spread out over greater distances. Since the sum in the numerator of Equation 4.19 omits the two highest energies, *LAT* is typically small for electromagnetic showers and larger for hadronic showers.

Only γ candidates which fulfill the condition

$$LAT < 0.55 \quad (4.21)$$

are retained. Two γ candidates are then combined to form a π^0 candidate.

The signal in the $\gamma\gamma$ invariant mass distribution is modeled by a ‘Novosibirsk function’

$$f(x) = \frac{N}{\sqrt{2\pi}\sigma} \exp \left(-\frac{1}{2} \left[\left(\frac{\ln \left(1 + \tau \frac{\sinh(\tau\sqrt{\ln 4})}{\tau\sqrt{\ln 4}} \frac{x-m}{\sigma} \right)}{\tau} \right)^2 + \tau^2 \right] \right). \quad (4.22)$$

The Novosibirsk function is a logarithmic normal distribution which is parameterized in such a way that two of its parameters, m and σ , correspond to the mean and standard deviation of a Gauss function. The third parameter, τ , describes the asymmetry. The Novosibirsk function is commonly used to model the energy distribution of neutral calorimeter clusters; its asymmetry takes energy leakage in the calorimeter into account.

The background is described by a third-order polynomial.

Since there is a mass shift in the measured π^0 mass between Run 1 and Run 2, both runs are considered separately. The $\gamma\gamma$ invariant mass distributions are shown in Figure 4.9; Table 4.4 summarizes the fit results. As can be seen, the Monte Carlo model does not produce the mass distributions of the data exactly.

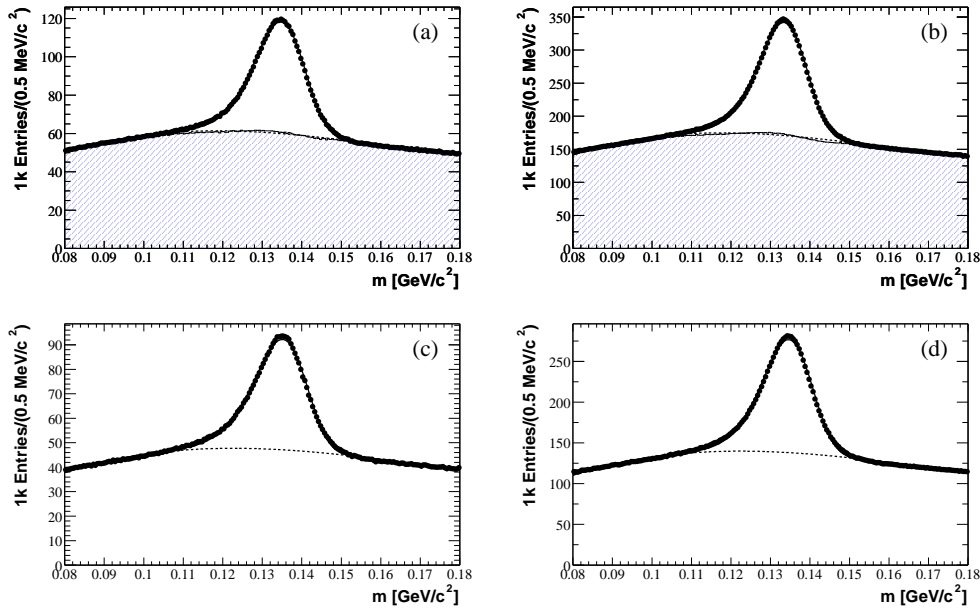


Figure 4.9: $\gamma\gamma$ invariant mass and fit functions, based on a 0.9 fb^{-1} subsample of the data and a corresponding amount of generic Monte Carlo events: (a) generic Monte Carlo, Run 1; (b) generic Monte Carlo, Run 2; (c) data, Run 1; (d) data, Run 2. The hatched areas in the Monte Carlo diagrams correspond to background.

4.5.1 π^0 Candidate Selection

The decay angle $\theta_{\pi^0}^*$ is defined as the angle between the momentum direction of one of the photons in the π^0 rest frame and the π^0 momentum direction in the $\Upsilon(4S)$ rest frame (center-of-mass frame).² The definition of this angle may appear similar to the definition of the helicity angle in Section 4.4.1; in fact, it is sometimes referred to as ‘helicity angle’. However, the two describe unrelated phenomena: While the helicity angle models the fact that a polarized vector meson decays with a characteristic angular distribution, the decay angle discriminates signal from background by the fact that the π^0 decays isotropically (which causes a flat distribution of $|\cos\theta_{\pi^0}^*|$), while $|\cos\theta_{\pi^0}^*|$ peaks near 1 for background introduced by random $\gamma\gamma$ combinations. To be retained, π^0 candidates must therefore fulfill the condition

$$|\cos\theta_{\pi^0}^*| < 0.85. \quad (4.23)$$

Furthermore, the π^0 candidates are required to have a momentum in the center-

²The momentum direction of the π^0 in the laboratory frame could also be used to define a similar decay angle θ_{π^0} ; however, a selection based on $\theta_{\pi^0}^*$ has slightly better discrimination power than a selection based on θ_{π^0} .

	Generic Monte Carlo	
	Run 1	Run 2
N	$(1.9138 \pm 0.0042) \times 10^6$	$(5.4038 \pm 0.0067) \times 10^6$
m	$134.757 \pm 0.016 \text{ MeV}/c^2$	$133.462 \pm 0.009 \text{ MeV}/c^2$
σ	$6.469 \pm 0.012 \text{ MeV}/c^2$	$6.236 \pm 0.007 \text{ MeV}/c^2$
τ	-0.1619 ± 0.0024	-0.1534 ± 0.0014
	Data	
	Run 1	Run 2
N	$(1.5440 \pm 0.0031) \times 10^6$	$(4.4846 \pm 0.0061) \times 10^6$
m	$135.155 \pm 0.018 \text{ MeV}/c^2$	$134.658 \pm 0.010 \text{ MeV}/c^2$
σ	$6.715 \pm 0.013 \text{ MeV}/c^2$	$6.375 \pm 0.008 \text{ MeV}/c^2$
τ	-0.1886 ± 0.0026	-0.1587 ± 0.0015

Table 4.4: Results of the fits to the $\gamma\gamma$ invariant mass distributions.

of-mass frame of

$$p_{\pi^0}^* > 150 \text{ MeV}/c. \quad (4.24)$$

To determine the optimal mass window for the selection of $\pi^0 \rightarrow \gamma\gamma$ candidates, it is necessary to compare the $\gamma\gamma$ mass distributions shown in Figure 4.9 with the mass distributions of exclusive π^0 candidates. The latter must fulfill all the π^0 candidate selection criteria and must additionally form a D_s^{*+} candidate when combined with a D_s^+ candidate³ according to the condition $139 < m_{D_s^+ \pi^0} - m_{D_s^+} < 151 \text{ MeV}/c^2$. The invariant mass distributions and fit results are shown in Figure 4.10 and Table 4.5.

The counted numbers of true Monte Carlo exclusive π^0 particles are 510 and 1343, while the yields obtained from the fits are 487.6 ± 59.0 and 1369.4 ± 100.3 for Run 1 and Run 2, respectively. These numbers therefore agree within error margins.

No useful information can be derived from the fit to Run 1 data due to low statistics. Specifically, the positive τ parameter is not compatible with the expectation of energy leakage in the calorimeter, which pulls the measured energy towards lower values and should therefore result in a negative τ . The Run 1 data has therefore been disregarded. Otherwise, the differences between the inclusive and exclusive π^0 candidates are summarized in Table 4.6.

To determine mass selection windows, the region where the fitted signal exceeds 0.2 times its maximum has been calculated for all samples with the exception of the exclusive Run 1 data sample. The results are shown in Table 4.7.

Given the large errors in the fits to the exclusive samples, and the fact that the signal shape of the exclusive π^0 mass distributions is mostly compatible with the

³A mass constrained fit is performed on the π^0 candidates before they are combined with the D_s^+ candidates.

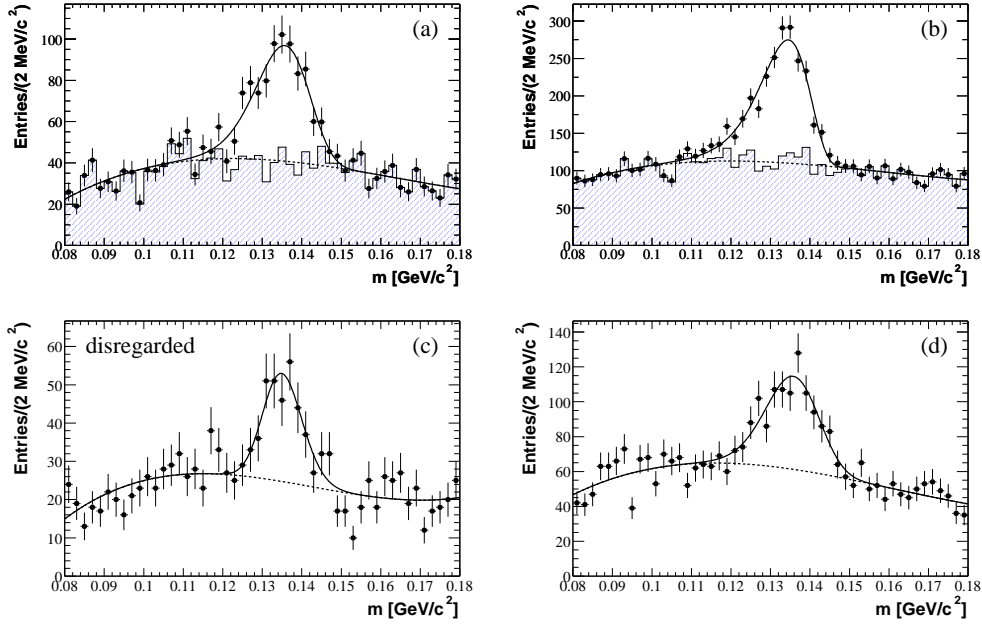


Figure 4.10: $\gamma\gamma$ invariant mass and fit functions for exclusive π^0 candidates (see text): (a) generic Monte Carlo, Run 1; (b) generic Monte Carlo, Run 2; (c) data, Run 1; (d) data, Run 2. The hatched areas in the Monte Carlo diagrams correspond to background. Figure (c) has been disregarded for the determination of the $\gamma\gamma$ mass window.

signal shape of the inclusive π^0 mass distributions, it has been decided to base the four mass windows on the inclusive samples. However, since there seems to be a $\approx 1 \text{ MeV}/c^2$ mass shift, $1 \text{ MeV}/c^2$ is subtracted from the values in the ‘Inclusive π^0 Candidates’ column of Table 4.7. The resulting mass windows are used to select π^0 candidates.

	Generic Monte Carlo	
	Run 1	Run 2
N	487.6 ± 59.0	1369.4 ± 100.3
m	$135.682 \pm 1.005 \text{ MeV}/c^2$	$134.510 \pm 0.474 \text{ MeV}/c^2$
σ	$6.843 \pm 0.730 \text{ MeV}/c^2$	$6.323 \pm 0.149 \text{ MeV}/c^2$
τ	-0.1716 ± 0.1519	-0.3107 ± 0.0725
	Data	
	Run 1	Run 2
N	175.2 ± 28.6	452.7 ± 59.9
m	$134.892 \pm 1.171 \text{ MeV}/c^2$	$135.777 \pm 1.165 \text{ MeV}/c^2$
σ	$4.941 \pm 0.789 \text{ MeV}/c^2$	$6.742 \pm 0.749 \text{ MeV}/c^2$
τ	0.0660 ± 0.1979	-0.0980 ± 0.1532

Table 4.5: Results of the fits to the $\gamma\gamma$ invariant mass distributions for exclusive π^0 candidates.

	Generic Monte Carlo	
	Run 1	Run 2
$m_{\text{incl}} - m_{\text{excl}}$	$0.925 \pm 1.020 \text{ MeV}/c^2$	$1.048 \pm 0.483 \text{ MeV}/c^2$
$(\sigma_{\text{incl}} - \sigma_{\text{excl}})/\sigma_{\text{excl}}$	0.058 ± 0.115	0.014 ± 0.068
$(\tau_{\text{incl}} - \tau_{\text{excl}})/\tau_{\text{excl}}$	0.060 ± 0.954	1.026 ± 0.492
	Data	
	Run 1	Run 2
$m_{\text{incl}} - m_{\text{excl}}$		$1.119 \pm 1.175 \text{ MeV}/c^2$
$(\sigma_{\text{incl}} - \sigma_{\text{excl}})/\sigma_{\text{excl}}$		0.058 ± 0.119
$(\tau_{\text{incl}} - \tau_{\text{excl}})/\tau_{\text{excl}}$		-0.382 ± 0.971

Table 4.6: Differences in the fit results between inclusive and exclusive π^0 candidates.

	Inclusive π^0 Candidates	Exclusive π^0 Candidates
Run 1 MC	$121.37 < m_{\gamma\gamma} < 144.77 \text{ MeV}/c^2$	$121.40 < m_{\gamma\gamma} < 146.18 \text{ MeV}/c^2$
Run 2 MC	$120.65 < m_{\gamma\gamma} < 143.19 \text{ MeV}/c^2$	$119.66 < m_{\gamma\gamma} < 143.02 \text{ MeV}/c^2$
Run 1 Data	$120.94 < m_{\gamma\gamma} < 145.29 \text{ MeV}/c^2$	
Run 2 Data	$121.50 < m_{\gamma\gamma} < 144.55 \text{ MeV}/c^2$	$122.58 < m_{\gamma\gamma} < 146.84 \text{ MeV}/c^2$

Table 4.7: $\gamma\gamma$ invariant mass window where the fitted π^0 signal exceeds 0.2 times its maximum.

4.6 $D_s^{*+} \rightarrow D_s^+ \pi^0$ Reconstruction

A mass constrained fit is performed on the π^0 candidates, which are then combined with the D_s^+ candidates to form D_s^{*+} candidates. The difference between the D_s^{*+} and the D_s^+ invariant mass

$$\Delta m_{D_s^+ \pi^0} = m_{D_s^+ \pi^0} - m_{D_s^+} \quad (4.25)$$

is plotted. The binning of the $\Delta m_{D_s^+ \pi^0}$ histograms has been chosen such that the kinematic threshold (m_{π^0}) corresponds exactly to one bin edge.

4.6.1 Signal Shape Determination

The matched generic Monte Carlo $D_s^{*+} \rightarrow D_s^+ \pi^0$ events are used to find a function which best describes the signal shape of the $\Delta m_{D_s^+ \pi^0}$ distribution. Four functions have been considered: a Gauss function, a Novosibirsk function, the sum of two Gauss functions, and a ‘mirrored Crystal Ball function’:

$$f(x) = N \cdot \begin{cases} \exp\left(-\frac{(x-m)^2}{2\sigma^2}\right) & \text{if } (x-m)/\sigma \leq \alpha \\ A\left(B - \frac{x-m}{\sigma}\right)^{-n} & \text{if } (x-m)/\sigma \geq \alpha \end{cases}, \quad (4.26)$$

$$A = \left(\frac{|\alpha|}{n}\right)^{-n} \exp\left(-\frac{\alpha^2}{2}\right), \quad B = \frac{n}{|\alpha|} - |\alpha|.$$

The latter is a Gauss function which changes to a power function at point $(x-m)/\sigma = \alpha$. A and B are chosen such that the function and its first derivative are continuous.⁴

Figure 4.11 shows the fitted functions for the selection and weighting method. The fit results are summarized in Table 4.8. While the function parameters have been calculated with a maximum likelihood fit, the quantity

$$\chi^2 = \sum_i \frac{(f(x_i) - n_i)^2}{\sigma_i^2} \quad (4.27)$$

is used to characterize the quality of the fit, i.e., how well the fit function models the data. The index i indices all non-empty bins, x_i is the $\Delta m_{D_s^+ \pi^0}$ value corresponding to the center of the i th bin, n_i is the number of entries in the i th bin, and σ_i is the error on the number of entries in the i th bin.

⁴The original function introduced by the Crystal Ball experiment changes to a power function at a point *below* the mean of the Gauss function, unlike the function here, which changes at a point *above* the mean. This function is therefore referred to as a ‘mirrored Crystal Ball function’.

Table 4.8 also quotes the probability that the fit function models the data correctly. This probability is calculated as

$$\text{Probability} = 1 - P\left(\frac{ndf}{2}, \frac{\chi^2}{2}\right), \quad (4.28)$$

where P is the incomplete Gamma function and ndf is the number of degrees of freedom, i.e., the number of non-empty bins minus the number of parameters in the fit function.

Finally, it can be observed that all fit functions reproduce the event yield correctly within error margins: By counting, 733 and 795.9 signal events are found for the selection and weighting method, respectively.

The sum of two Gauss functions has the highest probability for both methods. It is therefore chosen to model the signal shape.

4.6.2 Background Shape Determination

The background shape has been determined in a similar fashion to the one described in the previous section. Various functions are fitted to the unmatched generic Monte Carlo events, and the resulting fit probabilities as defined by Equation 4.28 are compared.

Three functions have been considered: First of all, a power function

$$f(x) = a(x - b)^2. \quad (4.29)$$

Secondly, a power function which at some point β changes to a second-order polynomial

$$f(x) = \begin{cases} Ax^2 + Bx + C & \text{if } x \leq \beta \\ a(x - b)^2 & \text{if } x \geq \beta \end{cases}, \quad (4.30)$$

$$A = (\beta - b)^{c-2} \cdot (c - 1),$$

$$B = (\beta - b)^{c-2} \cdot (2\beta - c(\beta + b)),$$

$$C = (\beta - b)^{c-2} \cdot (b^2 + (c - 2)\beta b).$$

The parameters A , B , and C have been chosen such that the function and its first derivative are continuous, and the function is zero at $x = b$. This function will be referred to as a ‘quadratic/power function’.

Finally, the third function is a product of an exponential function and a second-order polynomial:

$$f(x) = n \cdot \left(1 - \exp\left(\frac{\beta - x}{m_e}\right)\right) \cdot (x^2 + ax + b). \quad (4.31)$$

This will be referred to as an ‘exponential/quadratic function’.

In all cases, one fit parameter has been fixed such that $f(m_{\pi^0}) = 0$, to take into account the kinematic threshold.

The fits and results are shown in Figure 4.12 and Table 4.9. The exponential/quadratic function has the highest probability, although it is only slightly better than the quadratic/power function. The former is therefore chosen to model the background shape.

4.6.3 $D_s^{*+} \rightarrow D_s^+ \pi^0$ Event Yield

A sum of two Gauss functions and an ‘exponential/quadratic function’ (Equation 4.31) is fitted to the $\Delta m_{D_s^+ \pi^0}$ invariant mass difference distributions; the results of these fits are shown in Figure 4.13 and Table 4.10.

For the Monte Carlo sample, the event numbers obtained by counting the matched (true) events are 733 and 795.9 for the selection and weighting method, respectively. These numbers agree well with the event yields from the fits, 697.0 ± 46.7 and 812.5 ± 143.8 .

For the data, the event yield found for the selection method is

$$N_{\text{selection}}(D_s^{*+} \rightarrow D_s^+ \pi^0) = 560.1 \pm 43.4, \quad (4.32)$$

while for the weighting method,

$$N_{\text{weighting}}(D_s^{*+} \rightarrow D_s^+ \pi^0) = 578.6 \pm 41.6 \quad (4.33)$$

events are found.

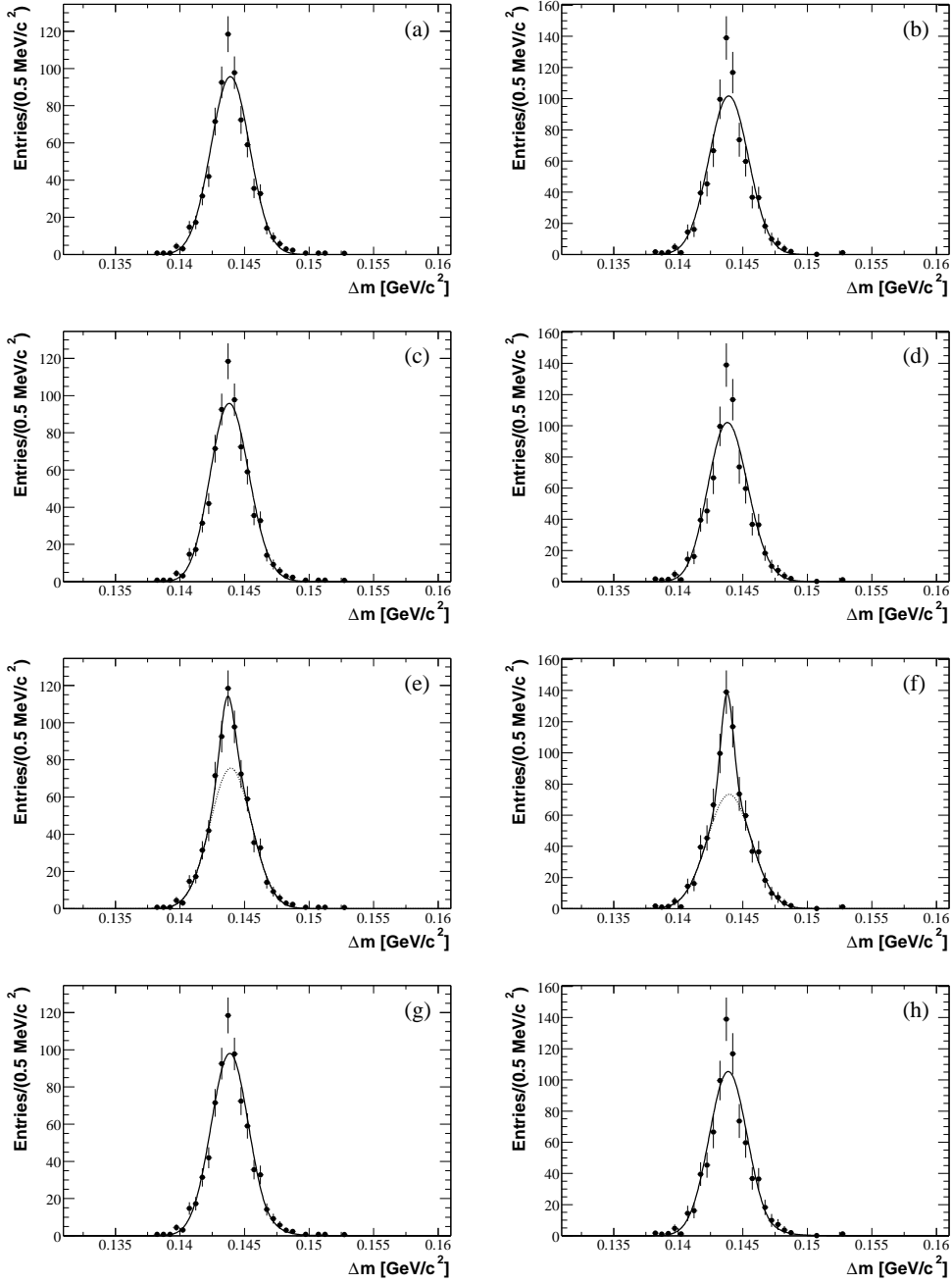


Figure 4.11: $\Delta m_{D_s^+ \pi^0}$ distribution of matched generic Monte Carlo events fitted with various functions: (a) Gauss function, selection method; (b) Gauss function, weighting method; (c) Novosibirsk function, selection method; (d) Novosibirsk function, weighting method; (e) sum of two Gauss functions, selection method; (f) sum of two Gauss functions, weighting method; (g) mirrored Crystal Ball function, selection method; (h) mirrored Crystal Ball function, weighting method.

	Gauss Function	
	Selection Method	Weighting Method
χ^2/ndf	30.74/23	41.61/24
Probability	0.129	0.014
N	719.0 ± 26.8	784.0 ± 28.0
m	$143.900 \pm 0.056 \text{ MeV}/c^2$	$143.912 \pm 0.055 \text{ MeV}/c^2$
σ	$1.499 \pm 0.040 \text{ MeV}/c^2$	$1.538 \pm 0.039 \text{ MeV}/c^2$
	Novosibirsk Function	
	Selection Method	Weighting Method
χ^2/ndf	29.09/22	38.24/23
Probability	0.142	0.024
N	719.3 ± 26.8	784.4 ± 28.0
m	$143.813 \pm 0.084 \text{ MeV}/c^2$	$143.810 \pm 0.074 \text{ MeV}/c^2$
σ	$1.496 \pm 0.040 \text{ MeV}/c^2$	$1.531 \pm 0.039 \text{ MeV}/c^2$
τ	0.0390 ± 0.0283	0.0443 ± 0.0219
	Sum of Two Gauss Functions	
	Selection Method	Weighting Method
χ^2/ndf	15.62/20	29.30/21
Probability	0.740	0.107
N_1	110.0 ± 52.2	158.0 ± 42.7
m_1	$143.669 \pm 0.140 \text{ MeV}/c^2$	$143.779 \pm 0.083 \text{ MeV}/c^2$
σ_1	$0.554 \pm 0.188 \text{ MeV}/c^2$	$0.484 \pm 0.110 \text{ MeV}/c^2$
N_2	609.0 ± 56.7	626.0 ± 47.8
m_2	$143.942 \pm 0.073 \text{ MeV}/c^2$	$143.946 \pm 0.072 \text{ MeV}/c^2$
σ_2	$1.609 \pm 0.067 \text{ MeV}/c^2$	$1.702 \pm 0.065 \text{ MeV}/c^2$
$N = N_1 + N_2$	719.0 ± 26.8	784.0 ± 28.0
	Mirrored Crystal Ball Function	
	Selection Method	Weighting Method
χ^2/ndf	25.31/21	45.26/22
Probability	0.234	0.002
N	719.0 ± 26.8	784.0 ± 28.0
m	$143.862 \pm 0.061 \text{ MeV}/c^2$	$143.873 \pm 0.058 \text{ MeV}/c^2$
σ	$1.450 \pm 0.049 \text{ MeV}/c^2$	$1.473 \pm 0.047 \text{ MeV}/c^2$
n	4.182 ± 0.595	9.835 ± 14.833
α	1.768 ± 0.293	1.982 ± 0.508

Table 4.8: Results of the fits of various functions to the $\Delta m_{D_s^+ \pi^0}$ distribution of matched generic Monte Carlo events.

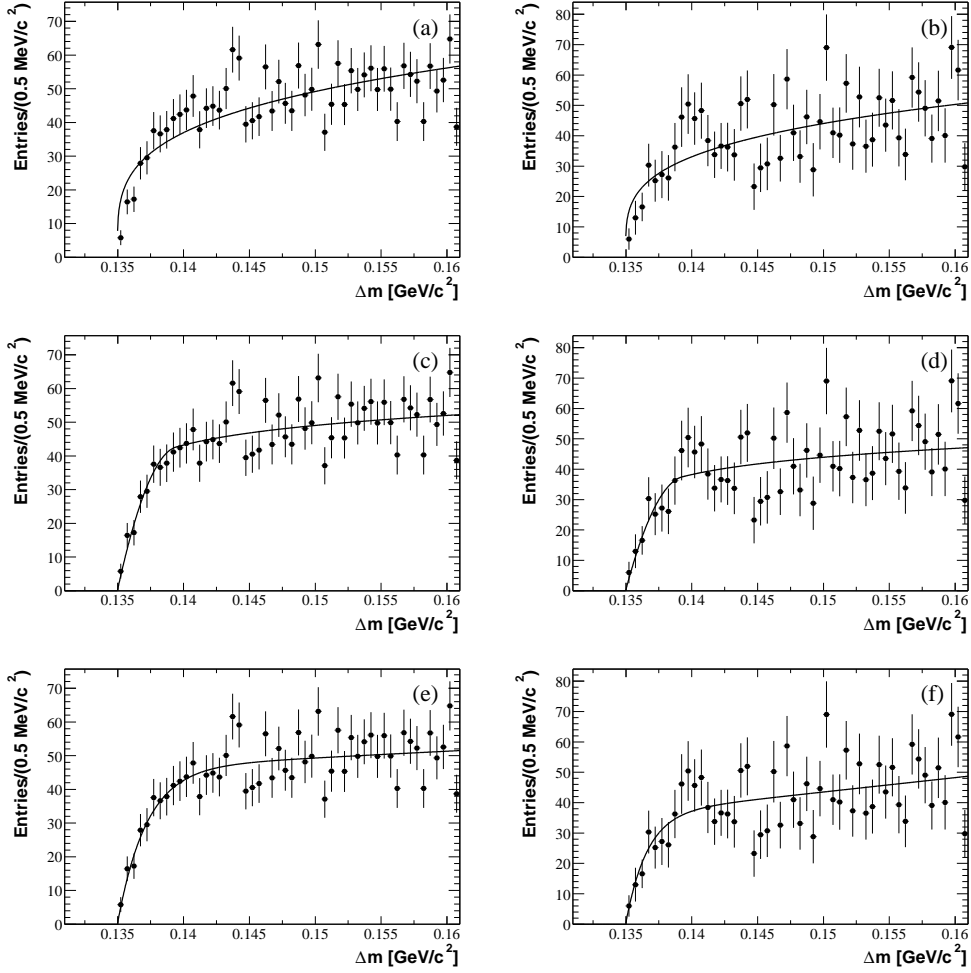


Figure 4.12: $\Delta m_{D_s^+ \pi^0}$ distribution of unmatched generic Monte Carlo events fitted with various functions: (a) power function, selection method; (b) power function, weighting method; (c) quadratic/power function, selection method; (d) quadratic/power function, weighting method; (e) exponential/quadratic function, selection method; (f) exponential/quadratic function, weighting method.

	Power Function	
	Selection Method	Weighting Method
χ^2/ndf	102.9/50	73.3/50
Probability	1.57×10^{-5}	0.017
a	$(293.39 \pm 34.55) \times 10^3$	$(263.75 \pm 32.83) \times 10^3$
b	m_{π^0}	m_{π^0}
c	0.260 ± 0.026	0.261 ± 0.028
	Quadratic/Power Function	
	Selection Method	Weighting Method
χ^2/ndf	54.3/49	60.2/49
Probability	0.279	0.131
a	$(159.09 \pm 31.68) \times 10^3$	$(149.61 \pm 28.48) \times 10^3$
b	m_{π^0}	m_{π^0}
c	0.115 ± 0.046	0.127 ± 0.044
β	$139.43 \pm 0.92 \text{ MeV}/c^2$	$139.27 \pm 0.78 \text{ MeV}/c^2$
	Exponential/Quadratic Function	
	Selection Method	Weighting Method
χ^2/ndf	52.3/48	58.9/48
Probability	0.311	0.134
n	$(60.37 \pm 17.72) \times 10^3$	$(63.89 \pm 63.92) \times 10^3$
m_e	$2.180 \pm 0.292 \text{ MeV}/c^2$	$1.579 \pm 0.316 \text{ MeV}/c^2$
β	m_{π^0}	m_{π^0}
a	6.218 ± 2.937	14.499 ± 11.685
b	0.680 ± 0.436	-0.835 ± 0.677

Table 4.9: Results of the fits of various functions to the $\Delta m_{D_s^+ \pi^0}$ distribution of unmatched generic Monte Carlo events.

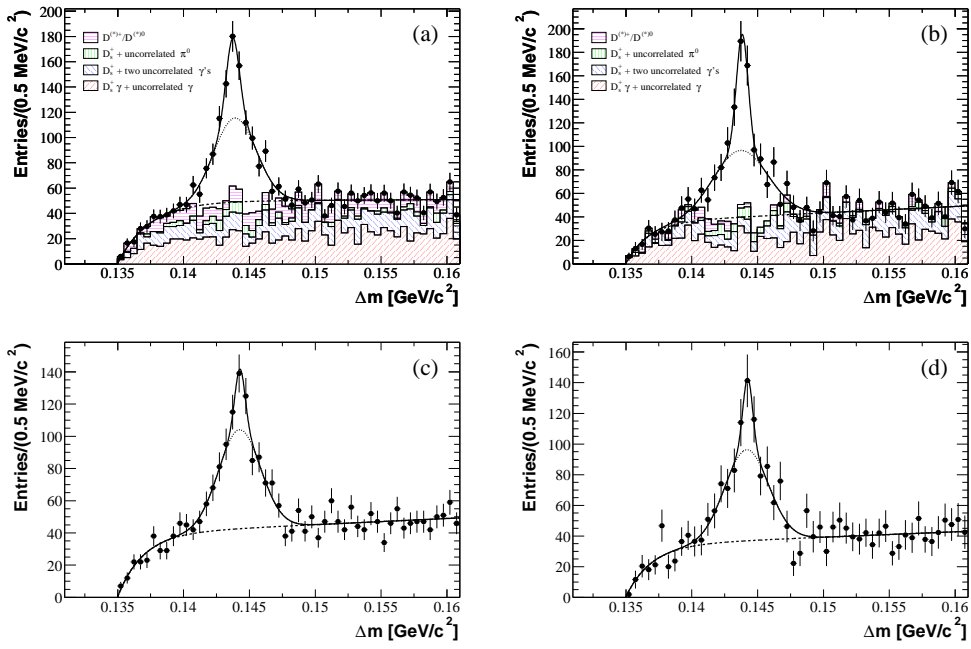


Figure 4.13: $\Delta m_{D_s^+ \pi^0}$ invariant mass difference distribution and fit functions: (a) generic Monte Carlo, selection method; (b) generic Monte Carlo, weighting method; (c) data, selection method; (d) data, weighting method. The hatched areas in the Monte Carlo diagrams correspond to background.

	Generic Monte Carlo	
	Selection Method	Weighting Method
N_1	159.1 ± 78.4	220.2 ± 49.0
m_1	$143.735 \pm 0.114 \text{ MeV}/c^2$	$143.835 \pm 0.064 \text{ MeV}/c^2$
σ_1	$0.499 \pm 0.171 \text{ MeV}/c^2$	$0.445 \pm 0.081 \text{ MeV}/c^2$
N_2	537.9 ± 80.8	592.4 ± 129.0
m_2	$143.907 \pm 0.155 \text{ MeV}/c^2$	$143.701 \pm 0.186 \text{ MeV}/c^2$
σ_2	$1.612 \pm 0.207 \text{ MeV}/c^2$	$2.081 \pm 0.392 \text{ MeV}/c^2$
$N = N_1 + N_2$	697.0 ± 46.7	812.5 ± 143.8
	Data	
	Selection Method	Weighting Method
N_1	72.8 ± 38.2	86.1 ± 31.9
m_1	$144.285 \pm 0.154 \text{ MeV}/c^2$	$144.252 \pm 0.110 \text{ MeV}/c^2$
σ_1	$0.387 \pm 0.132 \text{ MeV}/c^2$	$0.368 \pm 0.086 \text{ MeV}/c^2$
N_2	487.3 ± 51.7	492.6 ± 48.0
m_2	$144.251 \pm 0.138 \text{ MeV}/c^2$	$144.166 \pm 0.137 \text{ MeV}/c^2$
σ_2	$1.581 \pm 0.170 \text{ MeV}/c^2$	$1.655 \pm 0.151 \text{ MeV}/c^2$
$N = N_1 + N_2$	560.1 ± 43.4	578.6 ± 41.6

Table 4.10: Results of the fits to the $\Delta m_{D_s^+ \pi^0}$ invariant mass difference distributions.

4.7 $D_s^{*+} \rightarrow D_s^+ \gamma$ Reconstruction

The γ candidates for the reconstruction of the decay $D_s^{*+} \rightarrow D_s^+ \gamma$ are selected according to different criteria than the γ candidates for the $\pi^0 \rightarrow \gamma\gamma$ reconstruction. These criteria are chosen to optimize the signal efficiency of the $D_s^{*+} \rightarrow D_s^+ \gamma$ signal.

First of all, neutral clusters are required to have an energy in the laboratory frame of

$$E_\gamma > 50 \text{ MeV}. \quad (4.34)$$

The energy in the center-of-mass frame must fulfill the condition

$$E_\gamma^* > 100 \text{ MeV}, \quad (4.35)$$

and

$$LAT < 0.8 \quad (4.36)$$

must hold for the lateral energy distribution.

Furthermore, a π^0 *veto* greatly reduces the background consisting of photons from π^0 decays: The γ candidate under consideration is only retained if it does not form a π^0 candidate when it is combined with any other γ candidate in the event. For this selection criterion, a π^0 candidate is defined as a $\gamma\gamma$ combination with an invariant mass of

$$115 < m_{\gamma\gamma} < 155 \text{ MeV}/c^2 \quad (4.37)$$

and an energy in the center-of-mass frame of

$$E_{\gamma\gamma}^* > 200 \text{ MeV}. \quad (4.38)$$

The γ candidates which fulfill these criteria are combined with the D_s^+ candidates to form D_s^{*+} candidates, and the difference between the D_s^{*+} and the D_s^+ invariant mass

$$\Delta m_{D_s^+ \gamma} = m_{D_s^+ \gamma} - m_{D_s^+} \quad (4.39)$$

is plotted.

4.7.1 Signal Shape

To take into account the asymmetric line shape caused by energy leakage in the calorimeter, the $\Delta m_{D_s^+ \gamma}$ is modeled by a Crystal Ball function:⁵

$$f(x) = N \cdot \begin{cases} A \left(B - \frac{x-m}{\sigma} \right)^{-n} & \text{if } (x-m)/\sigma \leq \alpha \\ \exp \left(-\frac{(x-m)^2}{2\sigma^2} \right) & \text{if } (x-m)/\sigma \geq \alpha \end{cases}, \quad (4.40)$$

$$A = \left(\frac{|\alpha|}{n} \right)^{-n} \exp \left(-\frac{\alpha^2}{2} \right), \quad B = \frac{n}{|\alpha|} - |\alpha|.$$

⁵Its 'mirrored' version has already been introduced by Equation 4.26.

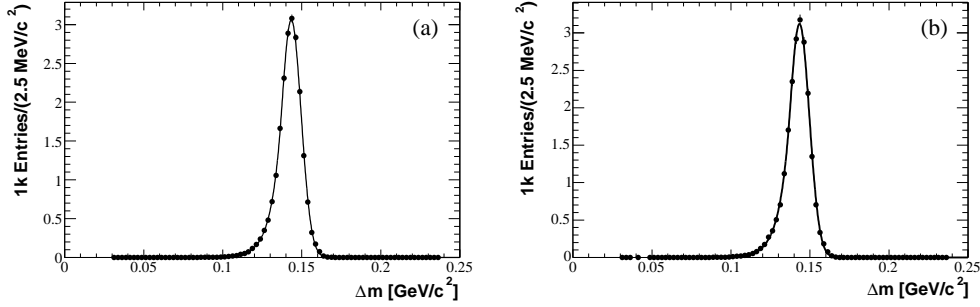


Figure 4.14: $\Delta m_{D_s^+\gamma}$ distribution of matched generic Monte Carlo events fitted with a Crystal Ball function: (a) selection method; (b) weighting method.

	Selection Method	Weighting Method
N	$20\,895 \pm 145$	$21\,386 \pm 146$
m	$143.347 \pm 0.072 \text{ MeV}/c^2$	$143.352 \pm 0.072 \text{ MeV}/c^2$
σ	$6.248 \pm 0.054 \text{ MeV}/c^2$	$6.253 \pm 0.054 \text{ MeV}/c^2$
n	61.502 ± 51.010	79.308 ± 83.806
α	-0.988 ± 0.031	-0.973 ± 0.030

Table 4.11: Results of the fits of a Crystal Ball function to the $\Delta m_{D_s^+\gamma}$ distribution of matched generic Monte Carlo events.

This function is a Gauss function which changes to a power function at point $(x - m)/\sigma = \alpha$. A and B are chosen such that the function and its first derivate are continuous.

A fit of the Crystal Ball function to the $\Delta m_{D_s^+\gamma}$ distribution of matched Monte Carlo events is shown in Figure 4.14; Table 4.11 summarizes the fit results. The counted numbers of true signal events are 20 914 for the selection method and 21 403 for the weighting method. The event yields from the fits, $20\,895 \pm 145$ for the selection method and $21\,386 \pm 146$ for the weighting method, therefore reproduce these numbers within error margins.

4.7.2 $D_s^{*+} \rightarrow D_s^+\gamma$ Event Yield

A sum of a Crystal Ball function for the signal and a third-order polynomial for the background is fitted to the $\Delta m_{D_s^+\gamma}$ invariant mass difference distributions. The fit range is constrained to $\Delta m_{D_s^+\gamma} > 60 \text{ MeV}/c^2$. Figure 4.15 shows the $\Delta m_{D_s^+\gamma}$ distributions; Table 4.12 summarizes the fit results.

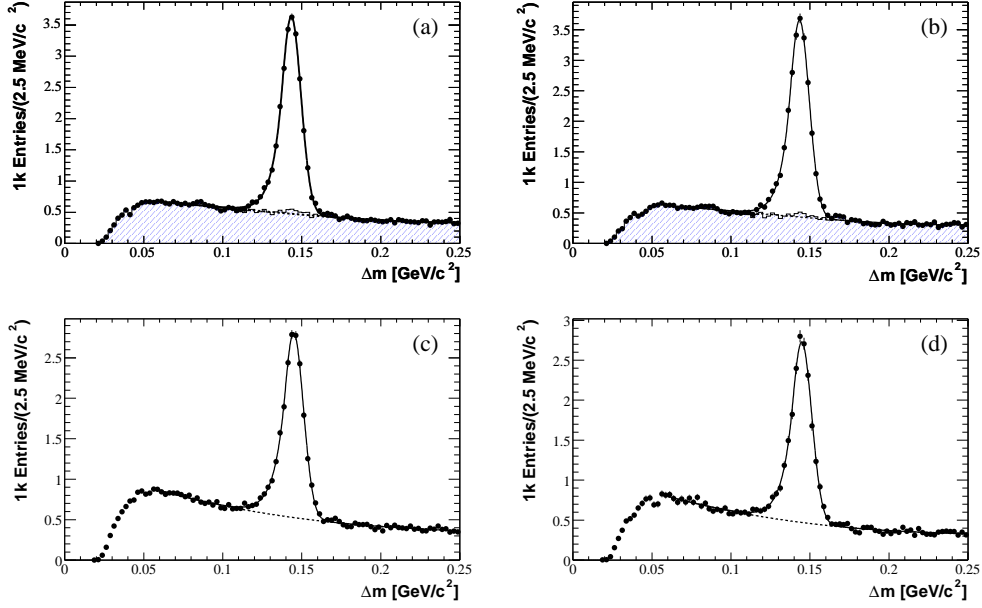


Figure 4.15: $\Delta m_{D_s^+ \gamma}$ invariant mass difference distribution and fit functions: (a) generic Monte Carlo, selection method; (b) generic Monte Carlo, weighting method; (c) data, selection method; (d) data, weighting method. The hatched areas in the Monte Carlo diagrams correspond to background.

The counted numbers of matched generic Monte Carlo events, 20 914 and 21 403 for the selection and weighting method, respectively, are reproduced within error margins by the fit results, $21\,055 \pm 199$ events for the selection and $21\,436 \pm 195$ events for the weighting method.

The event yield found in the data for the selection method is

$$N_{\text{selection}}(D_s^{*+} \rightarrow D_s^+ \pi^0) = 15\,622 \pm 194, \quad (4.41)$$

while

$$N_{\text{weighting}}(D_s^{*+} \rightarrow D_s^+ \pi^0) = 15\,616 \pm 208 \quad (4.42)$$

events are found for the weighting method.

	Generic Monte Carlo	
	Selection Method	Weighting Method
N	$21\,055 \pm 199$	$21\,436 \pm 195$
m	$143.386 \pm 0.081 \text{ MeV}/c^2$	$143.387 \pm 0.080 \text{ MeV}/c^2$
σ	$6.128 \pm 0.081 \text{ MeV}/c^2$	$6.117 \pm 0.079 \text{ MeV}/c^2$
n	$(1.316 \pm 0.596) \times 10^6$	$(2.752 \pm 0.288) \times 10^6$
α	-0.994 ± 0.035	-0.994 ± 0.034
	Data	
	Selection Method	Weighting Method
N	$15\,622 \pm 194$	$15\,616 \pm 208$
m	$144.887 \pm 0.103 \text{ MeV}/c^2$	$144.822 \pm 0.095 \text{ MeV}/c^2$
σ	$6.123 \pm 0.103 \text{ MeV}/c^2$	$6.267 \pm 0.098 \text{ MeV}/c^2$
n	$(687.8 \pm 1177.5) \times 10^3$	77.46 ± 305.82
α	-0.894 ± 0.037	-0.945 ± 0.055

Table 4.12: Results of the fits to the $\Delta m_{D_s^+\gamma}$ invariant mass difference distributions.

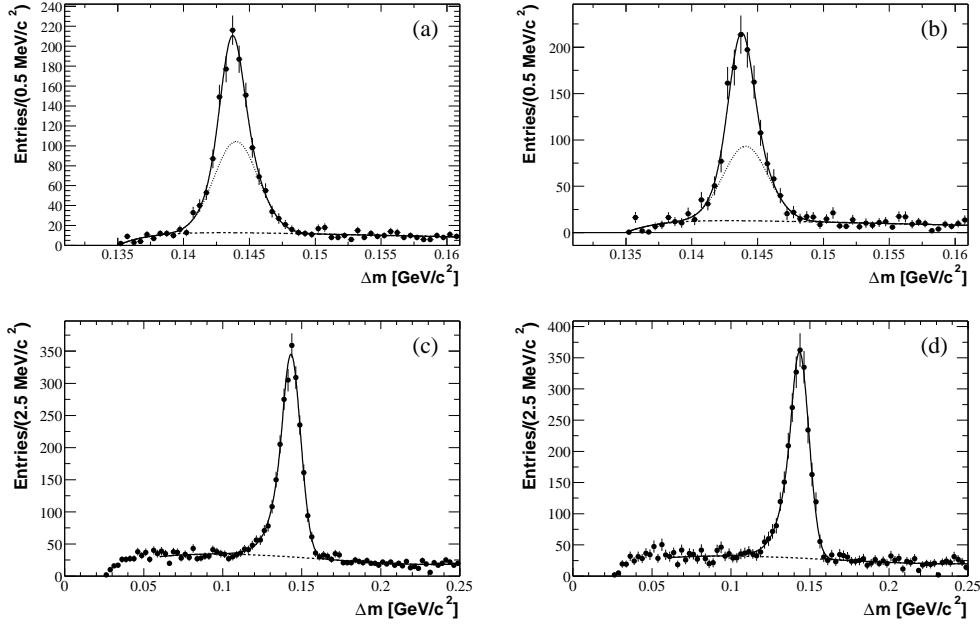


Figure 4.16: $\Delta m_{D_s^+ \pi^0}$ and $\Delta m_{D_s^+ \gamma}$ invariant mass difference distributions for 30 000 signal Monte Carlo events: (a) $\Delta m_{D_s^+ \pi^0}$ distribution, selection method; (b) $\Delta m_{D_s^+ \pi^0}$ distribution, weighting method; (c) $\Delta m_{D_s^+ \gamma}$ distribution, selection method; (d) $\Delta m_{D_s^+ \gamma}$ distribution, weighting method.

4.8 Efficiency Determination with Signal Monte Carlo Events

To estimate the efficiencies of the decays $D_s^{*+} \rightarrow D_s^+ \pi^0$ and $D_s^{*+} \rightarrow D_s^+ \gamma$, 30 000 signal Monte Carlo events of each decay channel have been used. By fitting the same functions to the $\Delta m_{D_s^+ \pi^0}$ and $\Delta m_{D_s^+ \gamma}$ distributions of signal Monte Carlo events as to the corresponding distributions of data events, the efficiencies can be determined.

The mass difference distributions for the signal Monte Carlo events are shown in Figure 4.16; Table 4.13 lists the fit results.

4.8.1 Systematic Uncertainties in Monte Carlo Efficiencies

The errors on the event numbers N express the limited statistics of signal Monte Carlo events; they represent a systematic uncertainty of the result.

Unrelated to this uncertainty, it must also be assumed that the Monte Carlo model does not describe the data perfectly, which introduces another source of uncertainty.

$D_s^{*+} \rightarrow D_s^+ \pi^0$ Signal Monte Carlo		
	Selection Method	Weighting Method
N_1	459.2 ± 191.6	559.7 ± 267.7
m_1	$143.677 \pm 0.098 \text{ MeV}/c^2$	$143.748 \pm 0.118 \text{ MeV}/c^2$
σ_1	$0.840 \pm 0.145 \text{ MeV}/c^2$	$0.901 \pm 0.153 \text{ MeV}/c^2$
N_2	769.3 ± 181.7	691.7 ± 245.3
m_2	$143.993 \pm 0.131 \text{ MeV}/c^2$	$144.091 \pm 0.148 \text{ MeV}/c^2$
σ_2	$1.675 \pm 0.188 \text{ MeV}/c^2$	$1.719 \pm 0.294 \text{ MeV}/c^2$
$N = N_1 + N_2$	$1\,222.2 \pm 51.2$	$1\,251.4 \pm 56.1$
$D_s^{*+} \rightarrow D_s^+ \gamma$ Signal Monte Carlo		
	Selection Method	Weighting Method
N	$2\,116.9 \pm 56.6$	$2\,206.8 \pm 57.1$
m	$143.195 \pm 0.257 \text{ MeV}/c^2$	$143.350 \pm 0.258 \text{ MeV}/c^2$
σ	$6.067 \pm 0.239 \text{ MeV}/c^2$	$5.968 \pm 0.230 \text{ MeV}/c^2$
n	$(481.49 \pm 634.99) \times 10^3$	$(1.657 \pm 4.514) \times 10^6$
α	-0.923 ± 0.088	-0.887 ± 0.080

Table 4.13: Results of the fits to the signal Monte Carlo $\Delta m_{D_s^+ \pi^0}$ and $\Delta m_{D_s^+ \gamma}$ invariant mass difference distributions.

π^0 Monte Carlo Efficiency

For the π^0 Monte Carlo, this has been studied using τ 1-on-1 decays, i.e., decays of $\tau^+ \tau^-$ lepton pairs, where one τ lepton decays to $e \nu_e \nu_\tau$, while the other τ lepton decays to a charged hadron, a neutrino, and one or two π^0 mesons [24]. The ratio R of two π^0 events to one π^0 events is calculated for the Monte Carlo and data samples in different energy ranges. The ratio of R obtained from data to R obtained from Monte Carlo events then provides an energy-dependent comparison of data and Monte Carlo efficiencies.

In this way, not only a correction function for the π^0 efficiency can be computed, but taking errors into account, an ‘error band’ corresponding to one standard deviation (1σ) can be obtained. This band represents the errors and uncertainties of the correction function. The result, which is a function of the π^0 energy in the laboratory frame $E_{\pi^0}^*$, is depicted in Figure 4.17.

The correction function and the error band are obtained by independent fits, so the function need not (and does not) lie entirely within the band. While this might at first seem surprising, it does in fact represent the best knowledge about the π^0 Monte Carlo efficiencies.

The correction function turns out to be 1, so no correction needs to be applied.

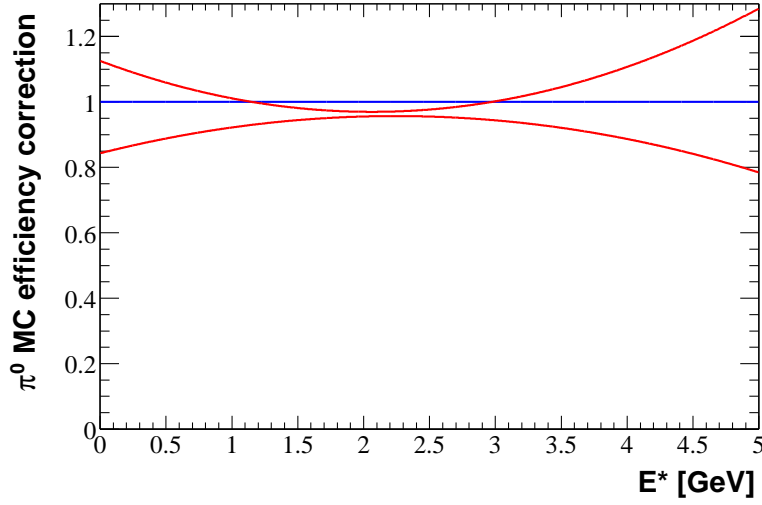


Figure 4.17: Monte Carlo efficiency correction function (blue) and 1σ error band (red) for π^0 mesons, as functions of the π^0 energy in the laboratory frame.

To obtain the systematic uncertainty of the $D_s^{*+} \rightarrow D_s^+ \pi^0$ efficiency, the method of ‘random killing’ is used: The signal Monte Carlo sample is processed again, and for each π^0 candidate, a normally distributed random number r is calculated according to the mean and standard deviation of the error band at the energy $E_{\pi^0}^*$ of the candidate. If r is greater than or equal to 1, nothing is done. Otherwise, another random number q is calculated, which is uniformly distributed between 0 and 1. If $q > r$, the candidate is ‘killed’, i.e., removed from the event.

γ Monte Carlo Efficiency

The same data and Monte Carlo samples used to obtain the π^0 Monte Carlo efficiency correction are also used to study the Monte Carlo efficiency of single photons. A comparison of the π^0 invariant mass width in the data and Monte Carlo samples is used to calculate an energy rescaling and random smearing function (collectively known as ‘ γ correction function’) to be applied to photons.

As in the case of the π^0 particles, a second processing of the Monte Carlo sample is required to obtain the systematic uncertainty. During this processing, a different γ correction function is used.

Monte Carlo Model Uncertainties

The results of processing the signal Monte Carlo sample with ‘random π^0 killing’ and the γ correction function for systematic uncertainties applied, as described in

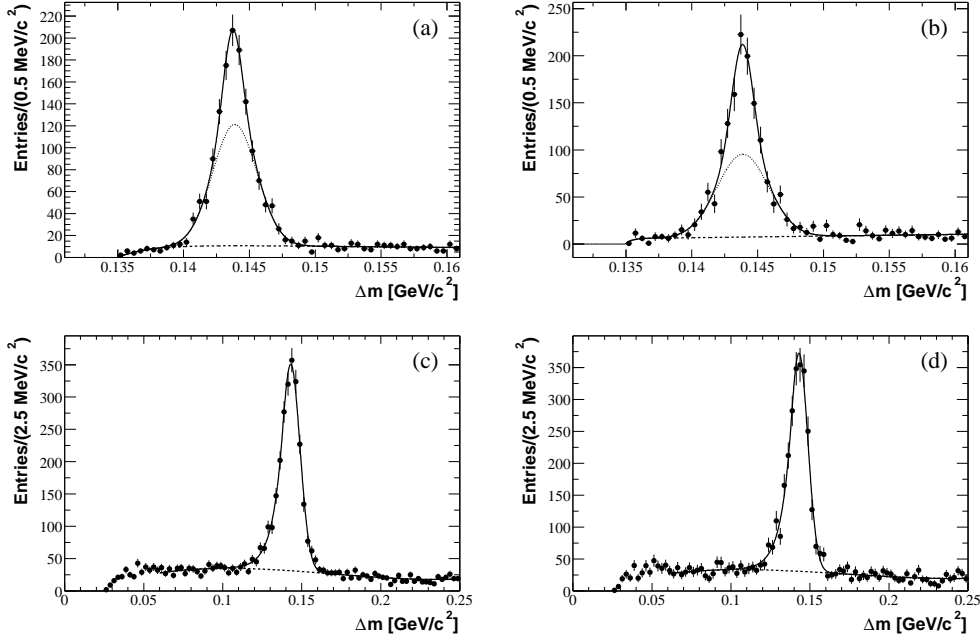


Figure 4.18: $\Delta m_{D_s^+ \pi^0}$ and $\Delta m_{D_s^+ \gamma}$ invariant mass difference distributions for 30 000 signal Monte Carlo events, with ‘random killing’ and the γ correction function for systematic uncertainties applied: (a) $\Delta m_{D_s^+ \pi^0}$ distribution, selection method; (b) $\Delta m_{D_s^+ \pi^0}$ distribution, weighting method; (c) $\Delta m_{D_s^+ \gamma}$ distribution, selection method; (d) $\Delta m_{D_s^+ \gamma}$ distribution, weighting method.

the previous sections, are shown in Figure 4.18 and Table 4.14. The discrepancies between these event yields and the event yields in Table 4.13 represent uncorrelated errors.

In addition to these uncorrelated errors, there are also (fixed) correlated errors. The correlated error on the π^0 Monte Carlo efficiency is 5.0%, while it is 2.5% for the γ Monte Carlo efficiency. The uncorrelated and correlated errors must be added in quadrature to obtain the total systematic uncertainty due to Monte Carlo model uncertainties.

However, this analysis does not make separate use of the efficiencies for the hadronic D_s^{*+} decay, $\epsilon(D_s^{*+} \rightarrow D_s^+ \pi^0)$, and the radiative D_s^{*+} decay, $\epsilon(D_s^{*+} \rightarrow D_s^+ \gamma)$. It only uses the *efficiency ratio* $\epsilon(D_s^{*+} \rightarrow D_s^+ \pi^0)/\epsilon(D_s^{*+} \rightarrow D_s^+ \gamma)$. Therefore, the two correlated errors cancel partially, and a total correlated error on the ratio of 2.5% remains. This must be summed in quadrature with the two uncorrelated errors.

	$D_s^{*+} \rightarrow D_s^+ \pi^0$ Signal Monte Carlo	
	Selection Method	Weighting Method
N_1	306.2 ± 120.6	470.2 ± 125.6
m_1	$143.733 \pm 0.100 \text{ MeV}/c^2$	$143.855 \pm 0.076 \text{ MeV}/c^2$
σ_1	$0.706 \pm 0.130 \text{ MeV}/c^2$	$0.804 \pm 0.112 \text{ MeV}/c^2$
N_2	931.8 ± 107.7	864.5 ± 118.5
m_2	$143.890 \pm 0.088 \text{ MeV}/c^2$	$143.877 \pm 0.096 \text{ MeV}/c^2$
σ_2	$1.682 \pm 0.164 \text{ MeV}/c^2$	$1.960 \pm 0.168 \text{ MeV}/c^2$
$N = N_1 + N_2$	$1\,238.0 \pm 76.6$	$1\,334.6 \pm 44.7$
	$D_s^{*+} \rightarrow D_s^+ \gamma$ Signal Monte Carlo	
	Selection Method	Weighting Method
N	$2\,068.6 \pm 56.0$	$2\,159.8 \pm 56.5$
m	$143.018 \pm 0.246 \text{ MeV}/c^2$	$143.011 \pm 0.247 \text{ MeV}/c^2$
σ	$5.834 \pm 0.245 \text{ MeV}/c^2$	$5.626 \pm 0.244 \text{ MeV}/c^2$
n	$(1.727 \pm 1.946) \times 10^6$	$(1.193 \pm 0.554) \times 10^6$
α	-0.916 ± 0.085	-0.872 ± 0.080

Table 4.14: Results of the fits to the signal Monte Carlo $\Delta m_{D_s^+ \pi^0}$ and $\Delta m_{D_s^+ \gamma}$ invariant mass difference distributions, with ‘random killing’ and the γ correction function for systematic uncertainties applied.

4.8.2 Efficiencies from Signal Monte Carlo Events

The efficiencies $\epsilon(D_s^{*+} \rightarrow D_s^+ \pi^0)$ and $\epsilon(D_s^{*+} \rightarrow D_s^+ \gamma)$ are calculated by dividing the event yields obtained in the signal Monte Carlo sample (Table 4.13) by 30 000, the number of signal Monte Carlo events. The resulting efficiencies, as well as their ratio, are tabulated in Table 4.15.

	Selection Method	Weighting Method
$\epsilon(D_s^{*+} \rightarrow D_s^+ \pi^0)$	0.0407 ± 0.0017	0.0417 ± 0.0019
$\epsilon(D_s^{*+} \rightarrow D_s^+ \gamma)$	0.0706 ± 0.0019	0.0736 ± 0.0019
$\frac{\epsilon(D_s^{*+} \rightarrow D_s^+ \pi^0)}{\epsilon(D_s^{*+} \rightarrow D_s^+ \gamma)}$	$0.5774 \pm 0.0287 \pm 0.0209$	$0.5671 \pm 0.0293 \pm 0.0421$

Table 4.15: Efficiencies of D_s^{*+} decays, and ratio of efficiencies, as obtained from signal Monte Carlo events. The first error results from Monte Carlo statistics; the second error in the ratio represents systematic uncertainties of the Monte Carlo model.

4.9 Efficiency Determination with D^{*0} Decays

To avoid dependency on Monte Carlo models, the efficiency ratio $\epsilon(D_s^{*+} \rightarrow D_s^+ \pi^0)/\epsilon(D_s^{*+} \rightarrow D_s^+ \gamma)$ can alternatively be determined from $D^{*0} \rightarrow D^0 \pi^0$ and $D^{*0} \rightarrow D^0 \gamma$ decays, exploiting the fact that the branching fractions

$$\mathcal{B}(D^{*0} \rightarrow D^0 \pi^0) = 0.619 \pm 0.029 \quad (4.43)$$

and

$$\mathcal{B}(D^{*0} \rightarrow D^0 \gamma) = 0.381 \pm 0.029 \quad (4.44)$$

are well known [3]. Under the assumptions that the efficiency ratio of the D^{*0} decays is identical to the efficiency ratio of the D_s^{*+} decays if the D^{*0} candidates are reconstructed with the same selection criteria as the D_s^{*+} candidates, i.e.,

$$\frac{\epsilon(D^{*0} \rightarrow D^0 \pi^0)}{\epsilon(D^{*0} \rightarrow D^0 \gamma)} = \frac{\epsilon(D_s^{*+} \rightarrow D_s^+ \pi^0)}{\epsilon(D_s^{*+} \rightarrow D_s^+ \gamma)}, \quad (4.45)$$

the efficiency ratio can be calculated by measuring the event yields $N(D^{*0} \rightarrow D^0 \pi^0)$ and $N(D^{*0} \rightarrow D^0 \gamma)$. To verify this assumption, the efficiency ratio $\epsilon(D^{*0} \rightarrow D^0 \pi^0)/\epsilon(D^{*0} \rightarrow D^0 \gamma)$ is calculated with signal Monte Carlo events, and compared to the ratio $\epsilon(D_s^{*+} \rightarrow D_s^+ \pi^0)/\epsilon(D_s^{*+} \rightarrow D_s^+ \gamma)$ as determined with signal Monte Carlo (cf. Section 4.8).

4.9.1 D^0 Reconstruction

D^0 candidates are reconstructed in the decay $D^0 \rightarrow K^- \pi^+$, where the kaon is required to fulfill the *tight* criteria. The D^0 candidates must satisfy the same vertex probability

$$P_{\text{vertex}}(\chi^2) > 0 \quad (4.46)$$

and scaled momentum

$$x_p = p_{D^0}^* / \sqrt{E_{\text{beam}}^{*2} - m_{D^0}^2} > 0.6 \quad (4.47)$$

criteria as the D_s^+ candidates (cf. Section 4.4).

The $K^- \pi^+$ invariant mass distributions for the Monte Carlo and data samples are shown in Figure 4.19. The sum of two Gauss functions for the signal and a third-order polynomial for the background is fitted to the distributions; the results of these fits are listed in Table 4.16. By counting matched Monte Carlo events, it is established that 1.05459×10^6 signal events are present, while $(1.04914 \pm 0.00128) \times 10^6$ are found by the fit.

D^0 candidates are retained for the D^{*0} reconstruction if their invariant mass $m_{K^- \pi^+}$ differs by less than $17 \text{ MeV}/c^2$ from expected mass m_{D^0} :

$$|m_{K^- \pi^+} - m_{D^0}| < 17 \text{ MeV}/c^2. \quad (4.48)$$

The known D^0 mass $m_{D^0} = 1864.5 \text{ MeV}/c^2$ [3] has been used for the Monte Carlo sample. For the data, it has been taken into account that the mean measured D^0 mass is $55 \text{ keV}/c^2$ below the mean Monte Carlo mass.

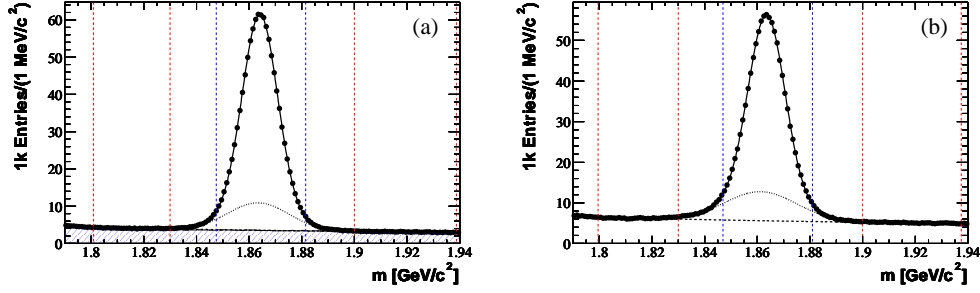


Figure 4.19: $K^-\pi^+$ invariant mass and fit functions: (a) generic Monte Carlo; (b) data. The hatched area in the Monte Carlo diagram corresponds to background. The vertical dotted lines indicate the signal and sideband regions.

	Generic Monte Carlo	Data
N_1	$(836.4 \pm 13.0) \times 10^3$	$(752.9 \pm 8.0) \times 10^3$
m_1	$1864.095 \pm 0.014 \text{ MeV}/c^2$	$1863.549 \pm 0.016 \text{ MeV}/c^2$
σ_1	$6.607 \pm 0.032 \text{ MeV}/c^2$	$6.893 \pm 0.029 \text{ MeV}/c^2$
N_2	$(212.7 \pm 12.6) \times 10^3$	$(243.1 \pm 7.5) \times 10^3$
m_2	$1863.548 \pm 0.079 \text{ MeV}/c^2$	$1861.342 \pm 0.111 \text{ MeV}/c^2$
σ_2	$11.532 \pm 0.227 \text{ MeV}/c^2$	$13.557 \pm 0.191 \text{ MeV}/c^2$
$N = N_1 + N_2$	$(1.04914 \pm 0.00128) \times 10^6$	$(0.99596 \pm 0.00146) \times 10^6$

Table 4.16: Results of the fits to the $K^-\pi^+$ invariant mass distributions.

4.9.2 $D^{*0} \rightarrow D^0\pi^0$ Reconstruction

The π^0 candidates to be combined with the D^0 candidates are selected in the same way as in the case of the $D_s^{*+} \rightarrow D_s^+\pi^0$ decay, as described in Section 4.5. The difference between the D^{*0} and the D^0 invariant mass

$$\Delta m_{D^0\pi^0} = m_{D^0\pi^0} - m_{D^0} \quad (4.49)$$

is shown in Figure 4.20 for both the Monte Carlo and the data sample.

The same fit function as for the $\Delta m_{D_s^+\pi^0}$ distribution is used to model $\Delta m_{D^0\pi^0}$: a sum of two Gauss functions for the signal and an ‘exponential/quadratic function’ (Equation 4.31) for the background. Table 4.17 lists the results.

The counted number of matched Monte Carlo events is 95 600, while the fit yields $94\,982 \pm 496$ events.

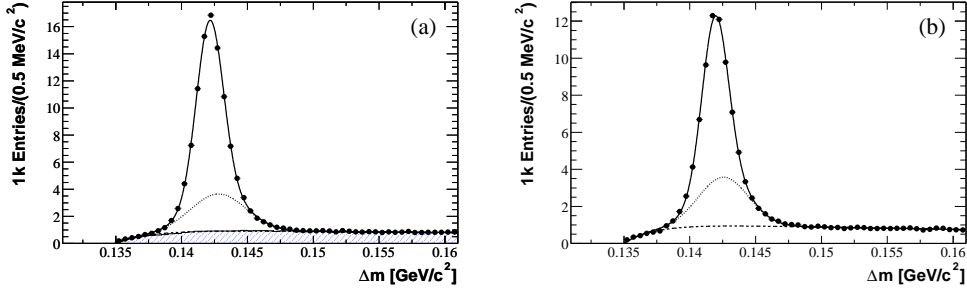


Figure 4.20: $\Delta m_{D^0 \pi^0}$ invariant mass difference distribution and fit functions: (a) generic Monte Carlo; (b) data. The hatched area in the Monte Carlo diagram corresponds to background.

	Generic Monte Carlo	Data
N_1	$(66.0 \pm 1.6) \times 10^3$	$(43.8 \pm 2.0) \times 10^3$
m_1	$142.147 \pm 0.008 \text{ MeV}/c^2$	$141.931 \pm 0.011 \text{ MeV}/c^2$
σ_1	$1.016 \pm 0.012 \text{ MeV}/c^2$	$0.988 \pm 0.019 \text{ MeV}/c^2$
N_2	$(29.0 \pm 1.5) \times 10^3$	$(25.1 \pm 1.9) \times 10^3$
m_2	$142.795 \pm 0.042 \text{ MeV}/c^2$	$142.561 \pm 0.061 \text{ MeV}/c^2$
σ_2	$2.107 \pm 0.046 \text{ MeV}/c^2$	$1.902 \pm 0.058 \text{ MeV}/c^2$
$N = N_1 + N_2$	$94\,982 \pm 496$	$68\,965 \pm 445$

Table 4.17: Results of the fits to the $\Delta m_{D^0 \pi^0}$ invariant mass difference distributions.

4.9.3 $D^{*0} \rightarrow D^0 \gamma$ Reconstruction

Again, the γ candidates to be combined with the D^0 candidates are selected in the same way as in the case of the corresponding D_s^{*+} decay $D_s^{*+} \rightarrow D_s^+ \gamma$, which is described in Section 4.7. The difference between the D^{*0} and the D^0 invariant mass

$$\Delta m_{D^0 \gamma} = m_{D^0 \gamma} - m_{D^0} \quad (4.50)$$

is then plotted.

Figure 4.21 shows the $\Delta m_{D^0 \gamma}$ distribution of unmatched (background) generic Monte Carlo events. A large π^0 reflection can be seen in the region $40 \lesssim \Delta m_{D^0 \gamma} \lesssim 110 \text{ MeV}/c^2$, which is unfortunately so close to the expected signal region that a polynomial is infeasible as a background model.

Instead, a product of an exponential function and a second-order polynomial is

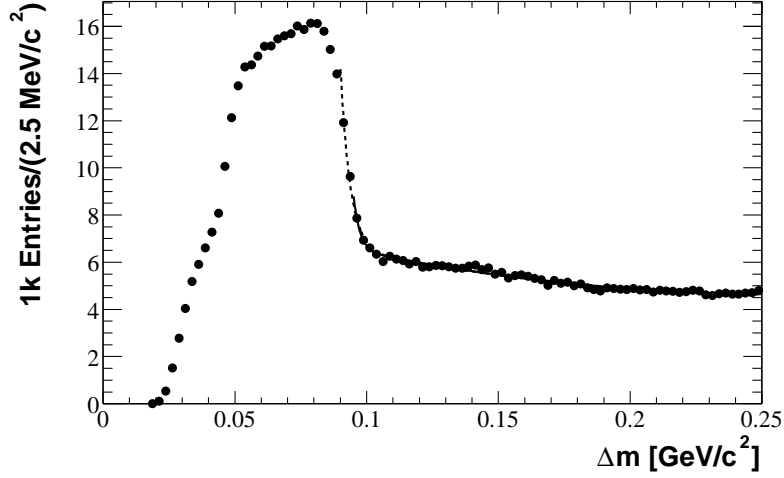


Figure 4.21: $\Delta m_{D^0\gamma}$ distribution of unmatched generic Monte Carlo events. The dotted line shows the result of a fit in the region $90 < \Delta m_{D^0\gamma} < 250 \text{ MeV}/c^2$, while the solid line results from a fit in the region $95 < \Delta m_{D^0\gamma} < 250 \text{ MeV}/c^2$.

used:⁶

$$f(x) = n \cdot \left(1 + \exp\left(\frac{\beta - x}{m_e}\right) \right) \cdot (x^2 + ax + b). \quad (4.51)$$

This function has been fitted to the $\Delta m_{D^0\gamma}$ distribution of unmatched generic Monte Carlo events in two different regions, $90 < \Delta m_{D^0\gamma} < 250 \text{ MeV}/c^2$ and $95 < \Delta m_{D^0\gamma} < 250 \text{ MeV}/c^2$. The results are listed in Table 4.18.

A Crystal Ball function (Equation 4.40) is used to model the signal. The fits to the generic Monte Carlo and data samples are shown in Figure 4.22 and Table 4.19. By counting matched Monte Carlo events, 94 761 events are found, which is in very good agreement with the event yield from the fit, $94\,374 \pm 623$.

4.9.4 Efficiencies from D^{*0} Decays

The efficiency ratio can be calculated from the event yields N obtained from the fits to the data and the known branching fractions:

$$\begin{aligned} \frac{\epsilon(D^{*0} \rightarrow D^0\pi^0)}{\epsilon(D^{*0} \rightarrow D^0\gamma)} &= \frac{N(D^{*0} \rightarrow D^0\pi^0)}{N(D^{*0} \rightarrow D^0\gamma)} \bigg/ \frac{\mathcal{B}(D^{*0} \rightarrow D^0\pi^0)}{\mathcal{B}(D^{*0} \rightarrow D^0\gamma)} \\ &= \frac{68\,965 \pm 445}{67\,882 \pm 665} \bigg/ \frac{0.619 \pm 0.029}{0.381 \pm 0.029} = 0.6253 \pm 0.0073 \pm 0.0769. \end{aligned} \quad (4.52)$$

⁶This function is similar to the ‘exponential/quadratic function’ (Equation 4.31), but differs in the sign of the exponential part.

	$90 < \Delta m_{D^0 \gamma} < 250 \text{ MeV}/c^2$	$95 < \Delta m_{D^0 \gamma} < 250 \text{ MeV}/c^2$
n	$(25.4 \pm 2.2) \times 10^6$	$(28.4 \pm 2.2) \times 10^6$
m_e	$3.726 \pm 0.126 \text{ MeV}/c^2$	$2.405 \pm 0.334 \text{ MeV}/c^2$
β	$90.645 \pm 0.087 \text{ MeV}/c^2$	$92.547 \pm 0.554 \text{ MeV}/c^2$
a	-0.530 ± 0.015	-0.515 ± 0.012
b	0.143 ± 0.010	0.132 ± 0.008

Table 4.18: Results of the fits to the $\Delta m_{D^0 \pi^0}$ distribution of unmatched generic Monte Carlo events for two different fitting regions.

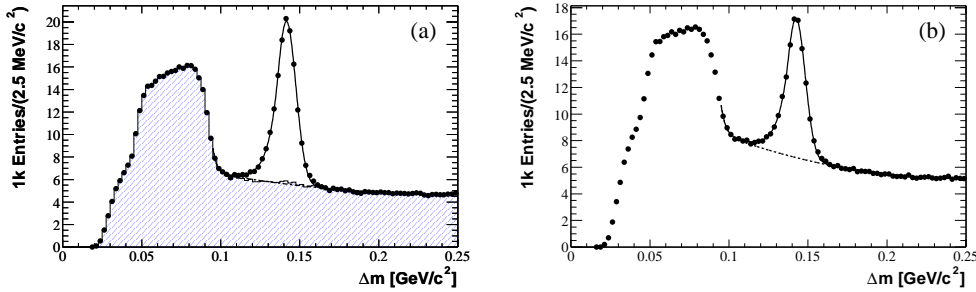


Figure 4.22: $\Delta m_{D^0 \gamma}$ invariant mass difference distribution and fit functions: (a) generic Monte Carlo; (b) data. The hatched area in the Monte Carlo diagram corresponds to background.

The first error of the ratio is statistical, the second represents uncertainties in the branching fractions.

It has been taken into account that the errors on the branching fractions are not independent. The Particle Data Group [3] calculates both branching fractions from three measurements of $D^{*0} \rightarrow D^0 \gamma$ [25, 26, 27] and the constraint $\mathcal{B}(D^{*0} \rightarrow D^0 \pi^0) + \mathcal{B}(D^{*0} \rightarrow D^0 \gamma) = 1$. The uncertainty of the branching fraction ratio is therefore the sum of the errors on the individual branching fractions.

4.9.5 Efficiencies of D^{*0} Decays from Signal Monte Carlo Events

30 000 signal Monte Carlo events for each of the channels $D^{*0} \rightarrow D^0 \pi^0$ and $D^{*0} \rightarrow D^0 \gamma$ have been processed, and the same functions have been fitted to the Δm distributions as for the data. To determine systematic effects due to Monte Carlo model uncertainties, this process has been repeated with ‘random π^0 killing’ and the γ correction for systematic uncertainties, as described in Section 4.8.1. All four Δm distributions are shown in Figure 4.23; the fit results are listed in Table 4.20.

	Generic Monte Carlo	Data
N	$94\,374 \pm 623$	$67\,882 \pm 665$
m	$141.586 \pm 0.042 \text{ MeV}/c^2$	$142.457 \pm 0.060 \text{ MeV}/c^2$
σ	$5.970 \pm 0.046 \text{ MeV}/c^2$	$5.791 \pm 0.065 \text{ MeV}/c^2$
n	$(1.512 \pm 0.741) \times 10^6$	$(635.2 \pm 519.1) \times 10^3$
α	-0.969 ± 0.023	-0.881 ± 0.029

Table 4.19: Results of the fits to the $\Delta m_{D^0\gamma}$ invariant mass difference distributions.

As in the case of the D_s^{*+} efficiencies, $\epsilon(D^{*0} \rightarrow D^0\pi^0)$ and $\epsilon(D^{*0} \rightarrow D^0\gamma)$ are obtained by dividing the event yields by 30 000, the number of processed events. The efficiencies and their ratio are shown in Table 4.21.

The D^{*0} efficiency ratio $\epsilon(D^{*0} \rightarrow D^0\pi^0)/\epsilon(D^{*0} \rightarrow D^0\gamma) = 0.5838 \pm 0.0313$ is in very good agreement (within statistical error margins) with the D_s^{*+} efficiency ratios $\epsilon(D_s^{*+} \rightarrow D_s^+\pi^0)/\epsilon(D_s^{*+} \rightarrow D_s^+\gamma) = 0.5774 \pm 0.0287$ and $\epsilon(D_s^{*+} \rightarrow D_s^+\pi^0)/\epsilon(D_s^{*+} \rightarrow D_s^+\gamma) = 0.5671 \pm 0.0293$ for the selection and weighting method, respectively. It is therefore justified to assume $\epsilon(D^{*0} \rightarrow D^0\pi^0)/\epsilon(D^{*0} \rightarrow D^0\gamma) = \epsilon(D_s^{*+} \rightarrow D_s^+\pi^0)/\epsilon(D_s^{*+} \rightarrow D_s^+\gamma)$.

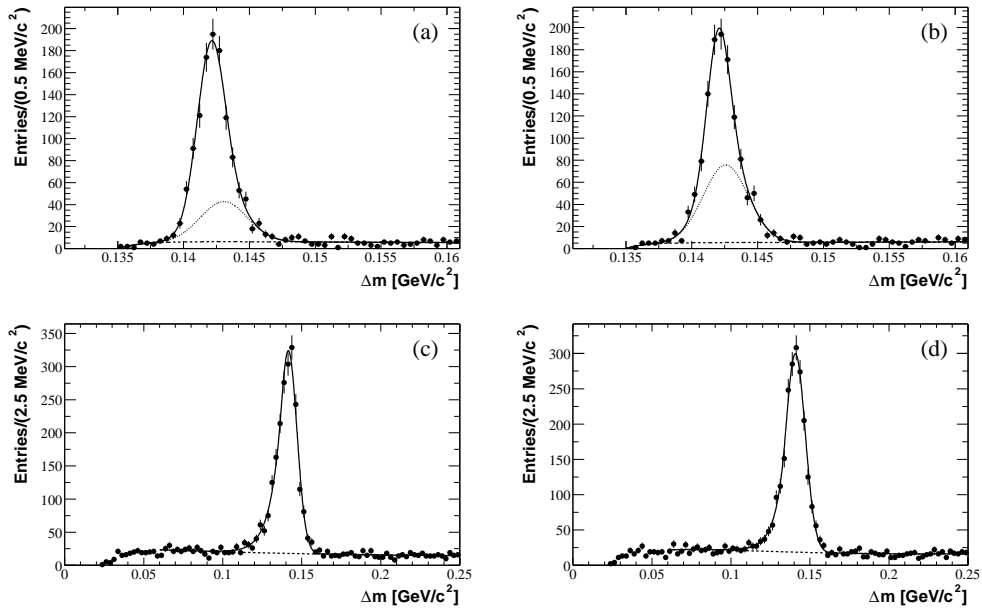


Figure 4.23: $\Delta m_{D^0 \pi^0}$ and $\Delta m_{D^0 \gamma}$ invariant mass difference distributions for 30 000 signal Monte Carlo events: (a) $\Delta m_{D^0 \pi^0}$ distribution; (b) $\Delta m_{D^0 \pi^0}$ distribution, with ‘random killing’ and the γ correction for systematic uncertainties; (c) $\Delta m_{D^0 \gamma}$ distribution; (d) $\Delta m_{D^0 \gamma}$ distribution, with ‘random killing’ and the γ correction for systematic uncertainties.

	$D^{*0} \rightarrow D^0\pi^0$ Signal Monte Carlo	
	No Systematic Corrections	Systematic Corrections
N_1	798.6 ± 224.6	549.2 ± 154.7
m_1	$142.094 \pm 0.108 \text{ MeV}/c^2$	$142.036 \pm 0.084 \text{ MeV}/c^2$
σ_1	$1.055 \pm 0.116 \text{ MeV}/c^2$	$0.864 \pm 0.112 \text{ MeV}/c^2$
N_2	325.7 ± 214.9	600.7 ± 150.6
m_2	$143.061 \pm 0.653 \text{ MeV}/c^2$	$142.572 \pm 0.168 \text{ MeV}/c^2$
σ_2	$1.783 \pm 0.381 \text{ MeV}/c^2$	$1.709 \pm 0.173 \text{ MeV}/c^2$
$N = N_1 + N_2$	$1\,124.4 \pm 52.2$	$1\,149.8 \pm 37.5$
	$D^{*0} \rightarrow D^0\gamma$ Signal Monte Carlo	
	No Systematic Corrections	Systematic Corrections
N	$1\,925.8 \pm 51.8$	$1\,890.3 \pm 61.1$
m	$141.487 \pm 0.268 \text{ MeV}/c^2$	$140.776 \pm 0.216 \text{ MeV}/c^2$
σ	$5.462 \pm 0.251 \text{ MeV}/c^2$	$6.207 \pm 0.209 \text{ MeV}/c^2$
n	$(1.485 \pm 0.904) \times 10^6$	17.53 ± 42.68
α	-0.805 ± 0.073	-1.071 ± 0.143

Table 4.20: Results of the fits to the signal Monte Carlo $\Delta m_{D^0\pi^0}$ and $\Delta m_{D^0\gamma}$ invariant mass difference distributions. The left column corresponds to the processing without corrections for the determination of systematic uncertainties, while the right column corresponds to the processing with ‘random killing’ and the γ correction function for systematic uncertainties.

$\epsilon(D^{*0} \rightarrow D^0\pi^0)$	0.0375 ± 0.0017
$\epsilon(D^{*0} \rightarrow D^0\gamma)$	0.0642 ± 0.0017
$\frac{\epsilon(D^{*0} \rightarrow D^0\pi^0)}{\epsilon(D^{*0} \rightarrow D^0\gamma)}$	$0.5838 \pm 0.0313 \pm 0.0225$

Table 4.21: Efficiencies of D^{*0} decays and ratio of efficiencies, as obtained from signal Monte Carlo events. The first error results from Monte Carlo statistics; the second error in the ratio represents systematic uncertainties of the Monte Carlo model.

	$\Gamma(D_s^{*+} \rightarrow D_s^+ \pi^0)/\Gamma(D_s^{*+} \rightarrow D_s^+ \gamma)$	
	Selection Method	Weighting Method
Efficiency Ratio from Monte Carlo	0.0621 ± 0.0049	0.0653 ± 0.0048
Efficiency Ratio from D^{*0} Decays	0.0574 ± 0.0046	0.0593 ± 0.0044

Table 4.22: Partial widths ratio $\Gamma(D_s^{*+} \rightarrow D_s^+ \pi^0)/\Gamma(D_s^{*+} \rightarrow D_s^+ \gamma)$. Errors are statistical only.

4.10 Results

With the knowledge of the event yields in the data and the ratio of the reconstruction efficiencies, the ratio of the partial widths can be calculated:

$$\frac{\Gamma(D_s^{*+} \rightarrow D_s^+ \pi^0)}{\Gamma(D_s^{*+} \rightarrow D_s^+ \gamma)} = \frac{N(D_s^{*+} \rightarrow D_s^+ \pi^0)}{N(D_s^{*+} \rightarrow D_s^+ \gamma)} \bigg/ \frac{\epsilon(D_s^{*+} \rightarrow D_s^+ \pi^0)}{\epsilon(D_s^{*+} \rightarrow D_s^+ \gamma)}. \quad (4.53)$$

By using all combinations of methods (selection vs. weighting method, and efficiency ratio from the signal Monte Carlo sample vs. D^{*0} decays), four results are obtained. They are listed in Table 4.22.

The quoted errors are the statistical errors on the $D_s^{*+} \rightarrow D_s^+ \pi^0$ and $D_s^{*+} \rightarrow D_s^+ \gamma$ event yields, and, for the numbers calculated with the efficiency ratio determined from D^{*0} decays, also include the statistical errors on the $D^{*0} \rightarrow D^0 \pi^0$ and $D^{*0} \rightarrow D^0 \gamma$ event yields.

4.11 Measurement of $\Gamma(D^{*0} \rightarrow D^0 \pi^0)/\Gamma(D^{*0} \rightarrow D^0 \gamma)$

Alternatively to using the measurement of the yield ratio $N(D^{*0} \rightarrow D^0 \pi^0)/N(D^{*0} \rightarrow D^0 \gamma)$ to determine $\epsilon(D_s^{*+} \rightarrow D_s^+ \pi^0)/\epsilon(D_s^{*+} \rightarrow D_s^+ \gamma)$ (cf. Section 4.9), it can also be considered a measurement of the partial widths ratio $\Gamma(D^{*0} \rightarrow D^0 \pi^0)/\Gamma(D^{*0} \rightarrow D^0 \gamma)$. With the efficiency ratio determined with signal Monte Carlo events (cf. Section 4.9.5), the following result is obtained (statistical errors only):

$$\frac{\Gamma(D^{*0} \rightarrow D^0 \pi^0)}{\Gamma(D^{*0} \rightarrow D^0 \gamma)} = \frac{N(D^{*0} \rightarrow D^0 \pi^0)}{N(D^{*0} \rightarrow D^0 \gamma)} \bigg/ \frac{\epsilon(D^{*0} \rightarrow D^0 \pi^0)}{\epsilon(D^{*0} \rightarrow D^0 \gamma)} = 1.7401 \pm 0.0204. \quad (4.54)$$

4.12 Confirmation of $D_{sJ}^*(2317)^+ \rightarrow D_s^+ \pi^0$

During *BABAR*'s search for the $D_{sJ}^*(2317)^+$ state [2], which decays to $D_s^+ \pi^0$, an attempt has been made to confirm the existence of the decay $D_{sJ}^*(2317)^+ \rightarrow D_s^+ \pi^0$ in the data used for the analysis presented in this dissertation. A subsample of 21.0 fb^{-1} has been reprocessed with slightly different criteria for the $\pi^0 \rightarrow \gamma\gamma$ selection:

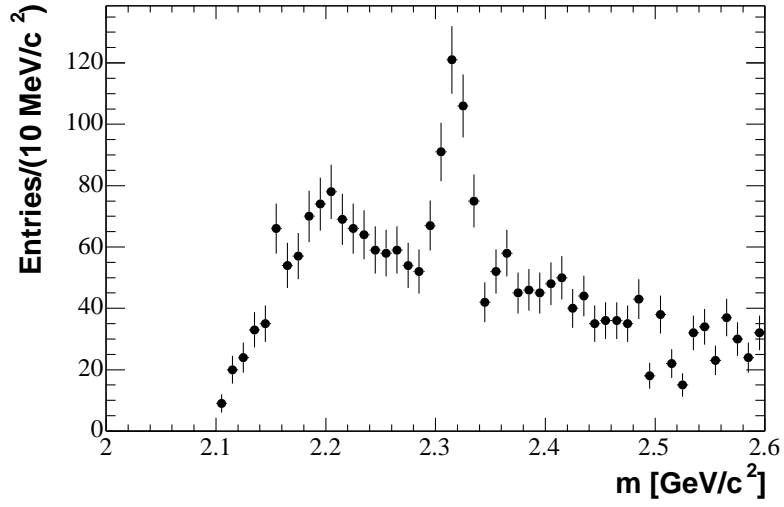


Figure 4.24: $D_s^+ \pi^0$ invariant mass distribution in the region of the $D_{sJ}^*(2317)^+$ mass, based on a 21.0 fb^{-1} subsample of the data.

- Photon energy in the laboratory frame: $E_\gamma > 150 \text{ MeV}$;
- π^0 mass window: $122 < m_{\gamma\gamma} < 148 \text{ MeV}/c^2$;
- π^0 momentum in the center-of-mass frame: $p_{\pi^0}^* > 300 \text{ MeV}/c$.

Figure 4.24 shows the resulting $D_s^+ \pi^0$ invariant mass distribution. A clear peak in the region of $2317 \text{ MeV}/c^2$ can be seen.

Chapter 5

Background

To test for peaking background structures in the signal region, left and right sidebands in the D_s^+ , D^0 , and π^0 invariant mass distributions have been analyzed. Monte Carlo sidebands have been compared to data sidebands; discrepancies are considered a systematic uncertainty.

The widths of the sidebands are chosen such that the expected number of background events in each sideband region corresponds to that of the signal region. The expected number of background events in a region is calculated by integrating the background function (obtained by fitting) over that region.

5.1 D_s^+ Sidebands

Table 5.1 lists the definitions of the D_s^+ sidebands.

	Selection Method	
	Left Sideband	Right Sideband
Monte Carlo	$1916 < m_{\phi\pi^+} < 1940 \text{ MeV}/c^2$	$2000 < m_{\phi\pi^+} < 2025 \text{ MeV}/c^2$
Data	$1916 < m_{\phi\pi^+} < 1940 \text{ MeV}/c^2$	$2000 < m_{\phi\pi^+} < 2026 \text{ MeV}/c^2$
	Weighting Method	
	Left Sideband	Right Sideband
Monte Carlo	$1914 < m_{\phi\pi^+} < 1940 \text{ MeV}/c^2$	$2000 < m_{\phi\pi^+} < 2025 \text{ MeV}/c^2$
Data	$1918 < m_{\phi\pi^+} < 1940 \text{ MeV}/c^2$	$2000 < m_{\phi\pi^+} < 2027 \text{ MeV}/c^2$

Table 5.1: Definitions of the D_s^+ sidebands.

	Selection Method	
	Left Sideband	Right Sideband
Monte Carlo	-5.03 ± 12.03	-0.52 ± 12.84
Data	9.62 ± 10.11	18.15 ± 10.62
	Weighting Method	
	Left Sideband	Right Sideband
Monte Carlo	7.69 ± 7.20	-8.53 ± 2.70
Data	-5.65 ± 2.97	34.36 ± 16.47

Table 5.2: Event yields in the $\Delta m_{D_s^+ \pi^0}$ invariant mass difference distributions with the D_s^{*+} candidate reconstructed from D_s^+ sidebands.

5.1.1 $D_s^+ \pi^0$ Reconstructed from D_s^+ Sidebands

The distributions of the invariant mass difference $\Delta m_{D_s^+ \pi^0}$ obtained by reconstructing the D_s^{*+} candidates with D_s^+ candidates from the sidebands are shown in Figure 5.1. The same function as for the $D_s^+ \pi^0$ signal, i.e., the sum of two Gauss functions and an ‘exponential/quadratic function’ (Equation 4.31), has been fitted to the distributions (cf. Section 4.6). In these fits, the signal shape parameters m_1 , σ_1 , m_2 , σ_2 , and the ratio N_1/N_2 have been fixed to the values found for the signal (cf. Table 4.10). The background parameters and the normalization of the signal have been included in the fit as free parameters.

The resulting event yields are summarized in Table 5.2. In the right D_s^+ sideband, an excess of events is observed in the data, but not in the Monte Carlo sample. It corresponds to 3.24% of the signal yield for the selection method and to 5.91% for the weighting method.

5.1.2 $D_s^+ \gamma$ Reconstructed from D_s^+ Sidebands

$D_s^{*+} \rightarrow D_s^+ \gamma$ is reconstructed with D_s^+ candidates from the sidebands; the results are shown in Figure 5.2. The sum of a Crystal Ball function (Equation 4.40) and a third-order polynomial are fitted to the $\Delta m_{D_s^+ \gamma}$ distributions, which is the same fit function as for the signal (cf. Section 4.7). Again, the signal shape parameters m , σ , n , α have been fixed to the values found for the signal (cf. Table 4.12), while the signal event yield and the background parameters have been determined by the fit.

The results are listed in Table 5.3. A peaking structure is observed both in the Monte Carlo sample and the data. By studying these structures with Monte Carlo events, it can be seen that in fact they arise from true $D_s^{*+} \rightarrow D_s^+ \gamma$ decays. If the momentum of one of the kaons or the pion from the D_s^+ decay is measured incorrectly (e.g., if the particle interacts with the drift chamber material), the invariant mass

	Selection Method	
	Left Sideband	Right Sideband
Monte Carlo	190.90 ± 33.54	122.24 ± 32.23
Data	207.20 ± 33.53	94.54 ± 31.05
	Weighting Method	
	Left Sideband	Right Sideband
Monte Carlo	173.08 ± 47.36	91.13 ± 43.21
Data	211.56 ± 50.78	38.74 ± 47.52

Table 5.3: Event yields in the $\Delta m_{D_s^+ \gamma}$ invariant mass difference distributions with the D_s^{*+} candidate reconstructed from D_s^+ sidebands.

of the D_s^+ candidate can fall into the sideband region.

Since the event yields of the peaking structures in the sidebands are compatible for the data and the Monte Carlo sample, it can be assumed that the Monte Carlo model describes this behavior correctly.

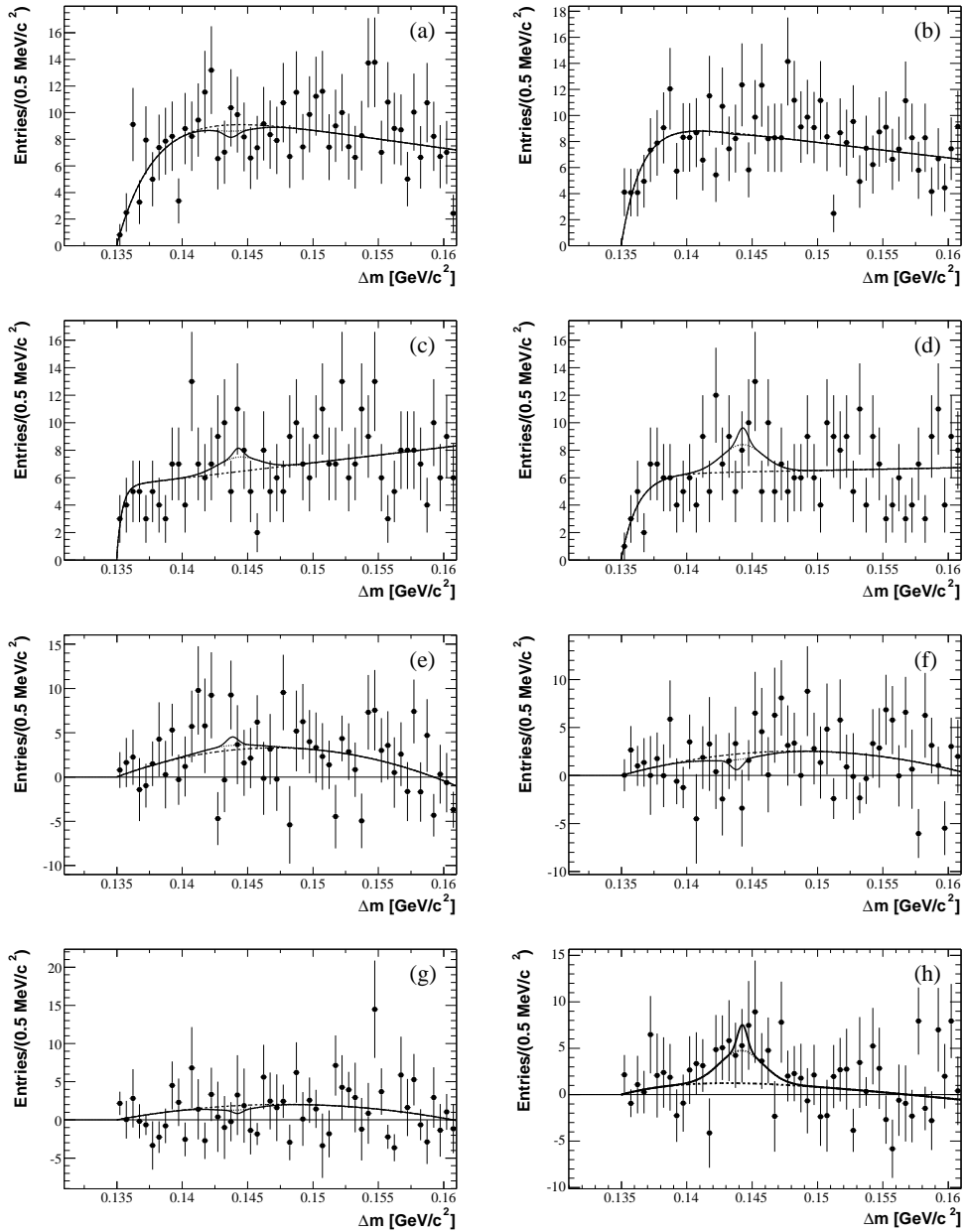


Figure 5.1: $\Delta m_{D_s^+ \pi^0}$ invariant mass difference distributions; D_s^{*+} reconstructed from D_s^+ sidebands: (a) generic Monte Carlo, selection method, left sideband; (b) generic Monte Carlo, selection method, right sideband; (c) data, selection method, left sideband; (d) data, selection method, right sideband; (e) generic Monte Carlo, weighting method, left sideband; (f) generic Monte Carlo, weighting method, right sideband; (g) data, weighting method, left sideband; (h) data, weighting method, right sideband.

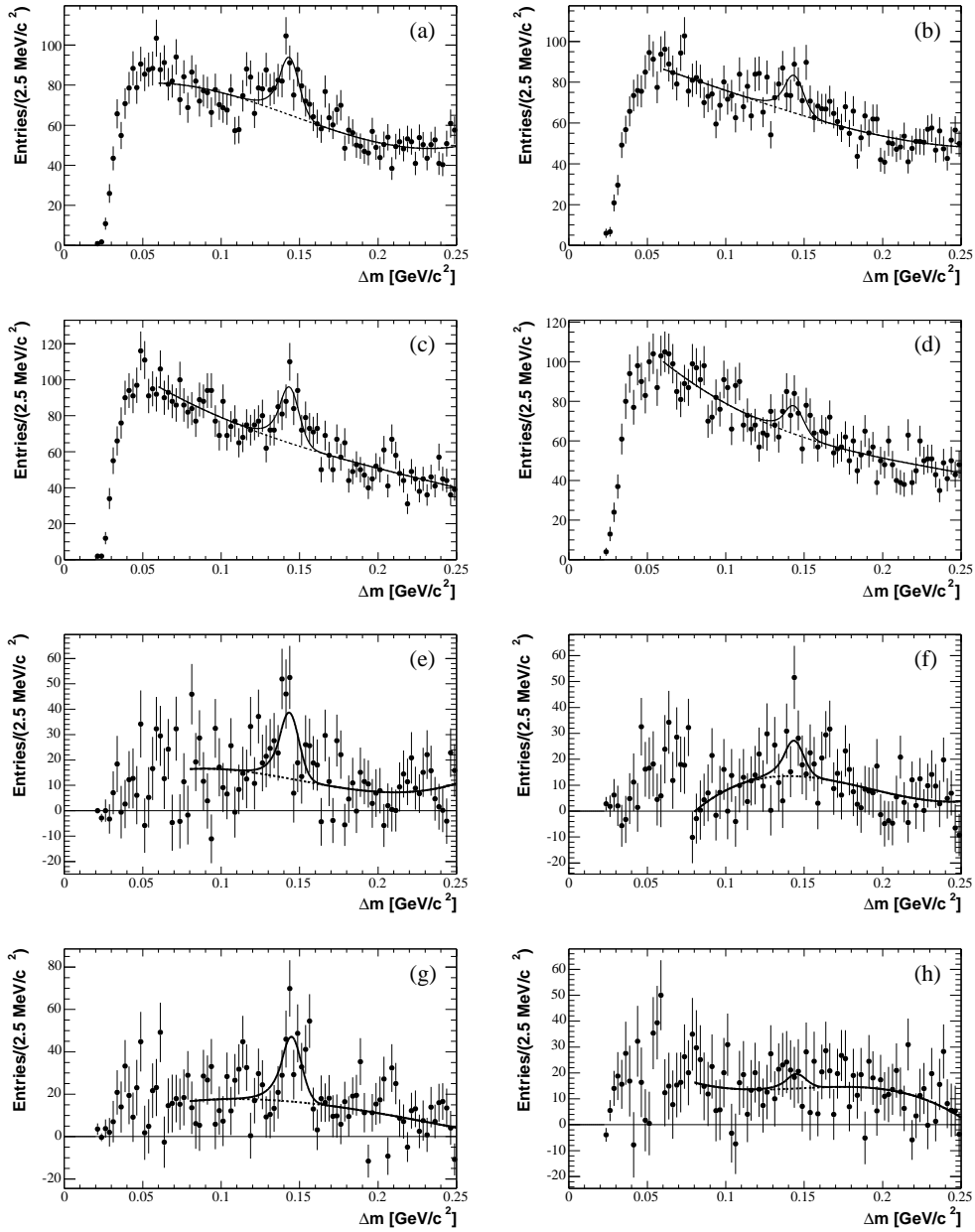
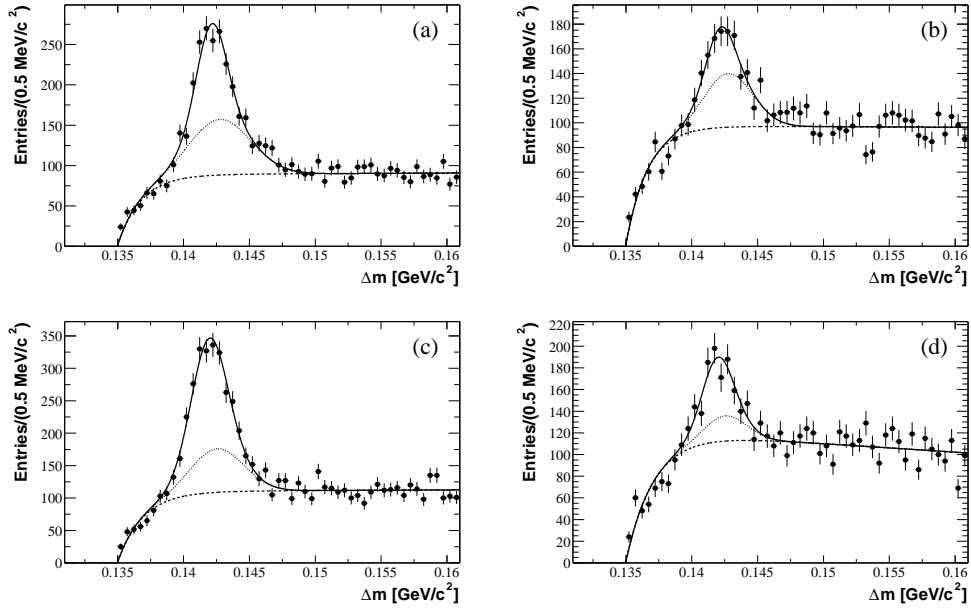


Figure 5.2: $\Delta m_{D_s^+ \gamma}$ invariant mass difference distributions; D_s^{*+} reconstructed from D_s^+ sidebands: (a) generic Monte Carlo, selection method, left sideband; (b) generic Monte Carlo, selection method, right sideband; (c) data, selection method, left sideband; (d) data, selection method, right sideband; (e) generic Monte Carlo, weighting method, left sideband; (f) generic Monte Carlo, weighting method, right sideband; (g) data, weighting method, left sideband; (h) data, weighting method, right sideband.

	Left Sideband	Right Sideband
Monte Carlo	$1801 < m_{K^- \pi^+} < 1830 \text{ MeV}/c^2$	$1900 < m_{K^- \pi^+} < 1939 \text{ MeV}/c^2$
Data	$1800 < m_{K^- \pi^+} < 1830 \text{ MeV}/c^2$	$1900 < m_{K^- \pi^+} < 1937 \text{ MeV}/c^2$

Table 5.4: Definitions of the D^0 sidebands.Figure 5.3: $\Delta m_{D^0 \pi^0}$ invariant mass difference distributions; D^{*0} reconstructed from D^0 sidebands: (a) generic Monte Carlo, left sideband; (b) generic Monte Carlo, right sideband; (c) data, left sideband; (d) data, right sideband.

5.2 D^0 Sidebands

The D^0 sidebands are defined according to Table 5.4.

5.2.1 $D^0 \pi^0$ Reconstructed from D^0 Sidebands

Figure 5.3 shows the $\Delta m_{D^0 \pi^0}$ distribution of D^{*0} candidates reconstructed with D^0 candidates from the sidebands. The distributions are fitted with the same function as the $D^{*0} \rightarrow D^0 \pi^0$ signal (cf. Section 4.9.2), but with the signal shape parameters fixed to the values of the signal (cf. Table 4.17). The resulting event yields are summarized in Table 5.5.

	Left Sideband	Right Sideband
Monte Carlo	1499.6 ± 87.0	608.1 ± 65.3
Data	1842.0 ± 79.2	511.3 ± 72.7

Table 5.5: Event yields in the $\Delta m_{D_s^+ \pi^0}$ invariant mass difference distributions with the D^{*0} candidate reconstructed from D^0 sidebands.

	Left Sideband	Right Sideband
Monte Carlo	1633.5 ± 102.2	916.4 ± 170.5
Data	1811.6 ± 157.1	727.5 ± 187.9

Table 5.6: Event yields in the $\Delta m_{D_s^+ \gamma}$ invariant mass difference distributions with the D^{*0} candidate reconstructed from D^0 sidebands.

As in the case of the D_s^+ sidebands, the peaking structures observed in the D^0 sidebands result from true D^0 particles with incorrectly measured momenta, which fall in the sideband regions. Since the event yields in the Monte Carlo sample and the data are again compatible, it can be assumed that no peaking structure is present under the signal.

5.2.2 $D^0 \gamma$ Reconstructed from D^0 Sidebands

The D^{*0} candidates are reconstructed with D^0 candidates from the sidebands; the resulting $\Delta m_{D^0 \gamma}$ distributions are shown in Figure 5.6. Again, the same fit function as for the signal is used (cf. Section 4.9.3) and the signal shape parameters are fixed to the signal values (cf. Table 4.19). Table 5.6 lists the event yields obtained in this way.

The peaking structures already observed in the D^0 sidebands for the decay $D^{*0} \rightarrow D^0 \pi^0$ are also seen in the $\Delta m_{D^0 \gamma}$ distributions. Again, the event yields in the Monte Carlo sample are compatible with the event yields in the data.

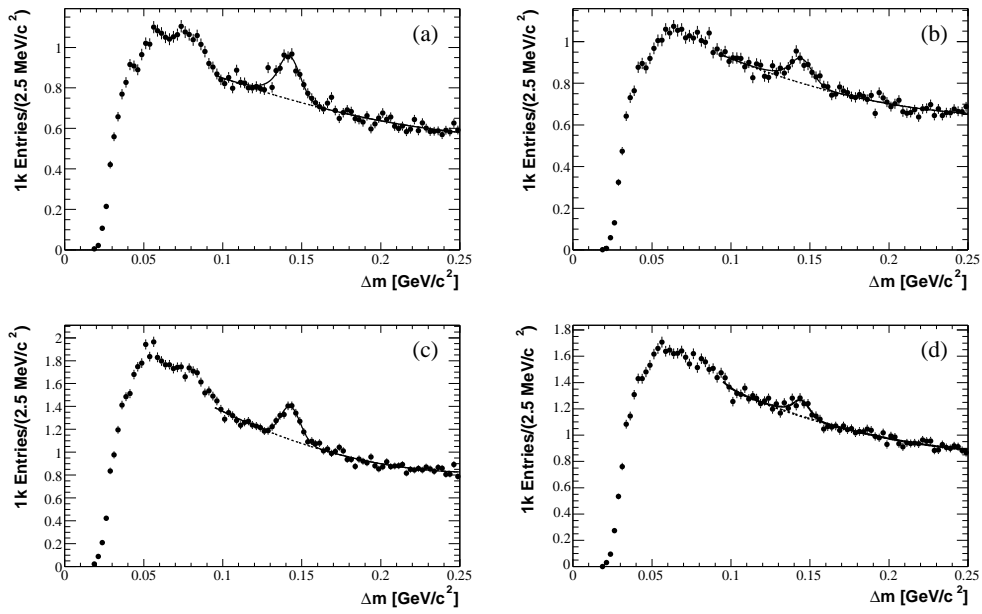


Figure 5.4: $\Delta m_{D^0\gamma}$ invariant mass difference distributions; D^{*0} reconstructed from D^0 sidebands: (a) generic Monte Carlo, left sideband; (b) generic Monte Carlo, right sideband; (c) data, left sideband; (d) data, right sideband.

	Run 1	
	Left Sideband	Right Sideband
Monte Carlo	$73.5 < m_{\gamma\gamma} < 100.0 \text{ MeV}/c^2$	$160.0 < m_{\gamma\gamma} < 187.9 \text{ MeV}/c^2$
Data	$71.2 < m_{\gamma\gamma} < 100.0 \text{ MeV}/c^2$	$160.0 < m_{\gamma\gamma} < 188.8 \text{ MeV}/c^2$
	Run 2	
	Left Sideband	Right Sideband
Monte Carlo	$74.7 < m_{\gamma\gamma} < 100.0 \text{ MeV}/c^2$	$160.0 < m_{\gamma\gamma} < 187.0 \text{ MeV}/c^2$
Data	$73.7 < m_{\gamma\gamma} < 100.0 \text{ MeV}/c^2$	$160.0 < m_{\gamma\gamma} < 186.6 \text{ MeV}/c^2$

Table 5.7: Definitions of the π^0 sidebands.

5.3 π^0 Sidebands

The π^0 sideband regions are defined separately for Run 1 and Run 2 according to Table 5.7.

5.3.1 $D_s^+\pi^0$ and $D^0\pi^0$ Reconstructed from π^0 Sidebands

The decays $D_s^{*+} \rightarrow D_s^+\pi^0$ and $D^{*0} \rightarrow D^0\pi^0$ are reconstructed with π^0 candidates from the sidebands, and as in the previous sections, the sum of two Gauss functions with fixed signal shape and an ‘exponential/quadratic function’ are fitted to the mass difference distributions. Figures 5.5 and 5.6 show the results.

The event yields obtained in this way are listed in Tables 5.8 and 5.9 for the D_s^{*+} and D^{*0} decays, respectively. They differ between Monte Carlo sample and data, but it should be noted that the fits to corresponding Monte Carlo and data distributions also yield very different background shapes. Therefore, another approach is followed to obtain potentially peaking background contributions, which is described in the following section.

	Selection Method	
	Left Sideband	Right Sideband
Monte Carlo	23.30 ± 20.19	14.59 ± 21.31
Data	-43.21 ± 22.70	-1.88 ± 26.63
	Weighting Method	
	Left Sideband	Right Sideband
Monte Carlo	31.91 ± 20.91	17.68 ± 22.19
Data	-81.26 ± 24.63	1.73 ± 24.42

Table 5.8: Event yields in the $\Delta m_{D_s^+ \pi^0}$ invariant mass difference distributions with the D_s^{*+} candidate reconstructed from π^0 sidebands.

	Left Sideband	Right Sideband
Monte Carlo	-97.4 ± 116.5	-304.4 ± 116.1
Data	-174.5 ± 117.4	-87.5 ± 115.4

Table 5.9: Event yields in the $\Delta m_{D_s^+ \pi^0}$ invariant mass difference distributions with the D^{*0} candidate reconstructed from π^0 sidebands.

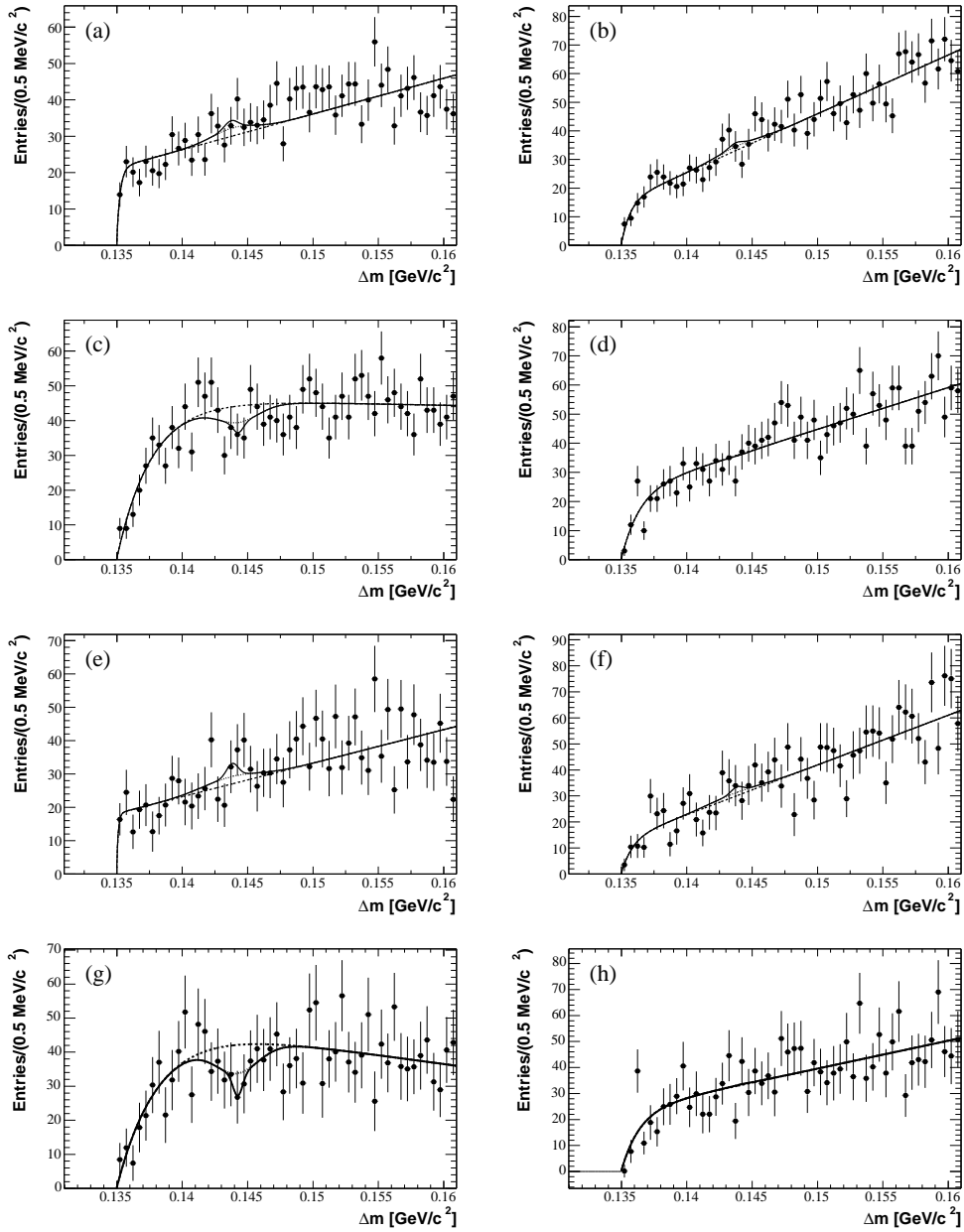


Figure 5.5: $\Delta m_{D_s^+ \pi^0}$ invariant mass difference distributions; D_s^{*+} reconstructed from π^0 sidebands: (a) generic Monte Carlo, selection method, left sideband; (b) generic Monte Carlo, selection method, right sideband; (c) data, selection method, left sideband; (d) data, selection method, right sideband; (e) generic Monte Carlo, weighting method, left sideband; (f) generic Monte Carlo, weighting method, right sideband; (g) data, weighting method, left sideband; (h) data, weighting method, right sideband.

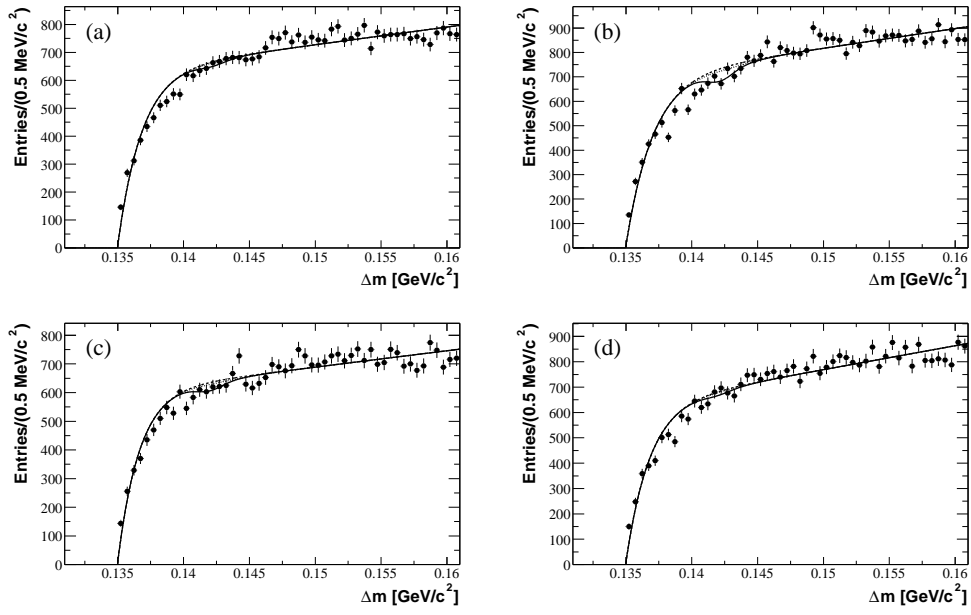


Figure 5.6: $\Delta m_{D^0\pi^0}$ invariant mass difference distributions; D^{*0} reconstructed from π^0 sidebands: (a) generic Monte Carlo, left sideband; (b) generic Monte Carlo, right sideband; (c) data, left sideband; (d) data, right sideband.

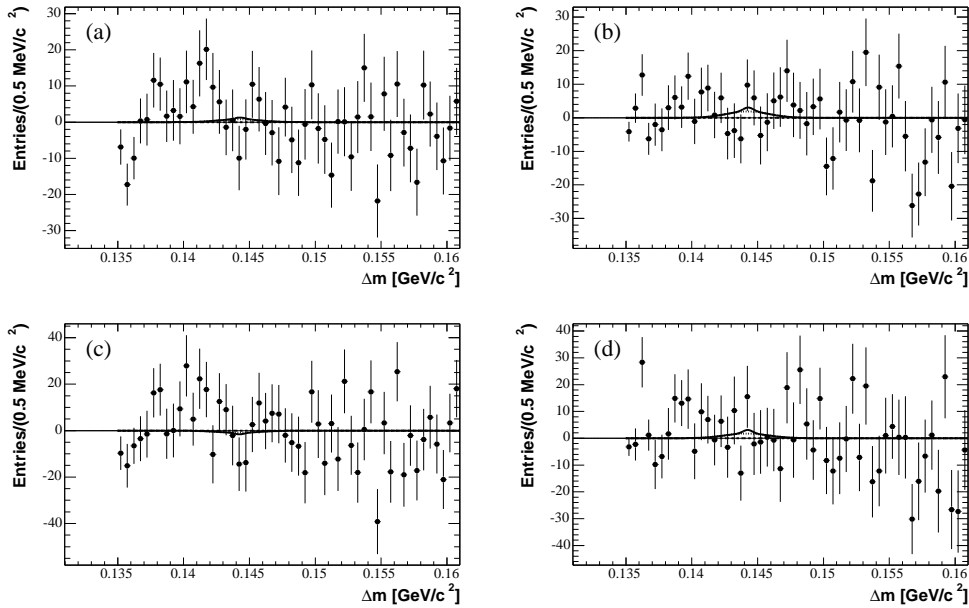


Figure 5.7: $\Delta m_{D_s^+ \pi^0}$ invariant mass difference distributions; D_s^{*+} reconstructed from π^0 sidebands; data with normalized Monte Carlo events subtracted: (a) selection method, left sideband; (b) selection method, right sideband; (c) weighting method, left sideband; (d) weighting method, right sideband.

5.3.2 Data with Monte Carlo Events Subtracted

For each π^0 sideband and decay channel involving π^0 mesons, the Monte Carlo histogram is normalized with respect to the corresponding data histogram, i.e., it is rescaled such that the total number of entries is the same for both histograms. The normalized Monte Carlo histogram is then subtracted from the data histogram, and a sum of two Gauss functions is fitted to the resulting difference histogram. In each fit, the signal shape parameters are again fixed to the values of the corresponding signal. Figures 5.7 and 5.8 show the resulting distribution.

Tables 5.10 and 5.11 list the event yields as well as what fraction of the corresponding signal event yield they constitute. All event yields are compatible with zero within error margins. However, to follow a conservative approach, the yields in the right sidebands (which are larger than the ones in the left sidebands) are taken as a systematic uncertainty of the background.

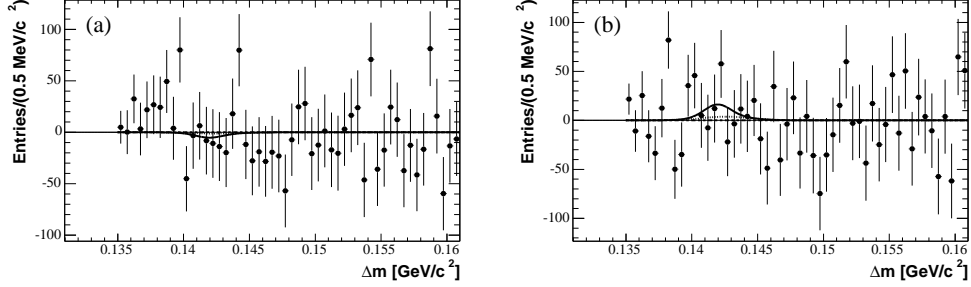


Figure 5.8: $\Delta m_{D^0\pi^0}$ invariant mass difference distributions; D^{*0} reconstructed from π^0 sidebands; data with normalized Monte Carlo events subtracted: (a) left sideband; (b) right sideband.

	Selection Method	
	Left Sideband	Right Sideband
Yield	7.2 ± 27.1	17.2 ± 24.7
Fraction of Signal Events	1.28%	3.07%
	Weighting Method	
	Left Sideband	Right Sideband
Yield	-8.7 ± 38.0	16.9 ± 35.7
Fraction of Signal Events	1.51%	2.92%

Table 5.10: Results of the fits to the $\Delta m_{D_s^+\pi^0}$ invariant mass difference distributions of data with normalized Monte Carlo events subtracted. The D_s^{*+} candidate has been reconstructed from the π^0 sidebands.

	Left Sideband	Right Sideband
Yield	-31.9 ± 100.4	98.7 ± 104.4
Fraction of Signal Events	0.05%	0.14%

Table 5.11: Results of the fits to the $\Delta m_{D^0\pi^0}$ invariant mass difference distributions of data with normalized Monte Carlo events subtracted. The D^{*0} candidate has been reconstructed from the π^0 sidebands.

Chapter 6

Momentum Spectra

6.1 Introduction

To test for a possible momentum dependency, the momentum p^* of the D_s^{*+} and D^{*0} candidates in the center-of-mass frame has been divided into five bins:

- $3.0 < p^* < 3.4 \text{ GeV}/c$;
- $3.4 < p^* < 3.8 \text{ GeV}/c$;
- $3.8 < p^* < 4.2 \text{ GeV}/c$;
- $4.2 < p^* < 4.6 \text{ GeV}/c$;
- $4.6 < p^* < 5.0 \text{ GeV}/c$.

The signal event yields for the four decays $D_s^{*+} \rightarrow D_s^+ \pi^0/\gamma$, $D^{*0} \rightarrow D^0 \pi^0/\gamma$ have been measured in the data, and signal Monte Carlo events have been used to correct for efficiency differences between the momentum bins. The theoretical fragmentation model by Collins and Spiller [28] has then been applied to estimate the momentum distribution of the D_s^{*+} and D^{*0} particles.

Next, $\Gamma(D_s^{*+} \rightarrow D_s^+ \pi^0)/\Gamma(D_s^{*+} \rightarrow D_s^+ \gamma)$ and $\Gamma(D^{*0} \rightarrow D^0 \pi^0)/\Gamma(D^{*0} \rightarrow D^0 \gamma)$ have been calculated for each bin. A constant function and a first-order polynomial have been fitted to the resulting distributions to test for a momentum dependency, and the latter fit has also been used to estimate a potentially unknown systematic momentum dependency.

The remainder of this chapter describes this methodology in more detail and presents the results.

6.2 Momentum Dependent Event Yields

The signal event yields for the decays $D_s^{*+} \rightarrow D_s^+ \pi^0$, $D_s^{*+} \rightarrow D_s^+ \gamma$, $D^{*0} \rightarrow D^0 \pi^0$, and $D^{*0} \rightarrow D^0 \gamma$ (the former two reconstructed with the selection and weighting

method) have been determined by fitting a function to the invariant mass difference distributions, as described in Chapter 4. Additionally, for each fit the momentum of the D_s^{*+} or D^{*0} candidates in the center-of-mass frame has been constrained to one of five 400 MeV/ c wide ranges, as specified in Section 6.1. The results are shown in Figures 6.1 to 6.6 and Tables 6.1 to 6.3. Figures 6.7 to 6.9 depict the momentum spectra.

	Selection Method	Weighting Method
$3.0 < p_{D_s^{*+}}^* < 3.4 \text{ GeV}/c$	68.2 ± 24.7	79.0 ± 16.3
$3.4 < p_{D_s^{*+}}^* < 3.8 \text{ GeV}/c$	162.0 ± 20.2	160.8 ± 19.7
$3.8 < p_{D_s^{*+}}^* < 4.2 \text{ GeV}/c$	192.4 ± 19.4	199.0 ± 23.1
$4.2 < p_{D_s^{*+}}^* < 4.6 \text{ GeV}/c$	92.6 ± 14.0	96.7 ± 12.3
$4.6 < p_{D_s^{*+}}^* < 5.0 \text{ GeV}/c$	32.2 ± 8.2	32.8 ± 7.1

Table 6.1: $D_s^{*+} \rightarrow D_s^+ \pi^0$ event yields obtained in the data for different momentum bins.

	Selection Method	Weighting Method
$3.0 < p_{D_s^{*+}}^* < 3.4 \text{ GeV}/c$	2063.6 ± 68.1	2051.8 ± 65.7
$3.4 < p_{D_s^{*+}}^* < 3.8 \text{ GeV}/c$	4726.7 ± 90.6	4831.0 ± 89.3
$3.8 < p_{D_s^{*+}}^* < 4.2 \text{ GeV}/c$	4638.9 ± 84.2	4561.5 ± 83.1
$4.2 < p_{D_s^{*+}}^* < 4.6 \text{ GeV}/c$	3142.2 ± 67.7	3098.5 ± 67.0
$4.6 < p_{D_s^{*+}}^* < 5.0 \text{ GeV}/c$	1029.2 ± 39.8	1051.8 ± 39.0

Table 6.2: $D_s^{*+} \rightarrow D_s^+ \gamma$ event yields obtained in the data for different momentum bins.

	$D^{*0} \rightarrow D^0 \pi^0$	$D^{*0} \rightarrow D^0 \gamma$
$3.0 < p_{D^{*0}}^* < 3.4 \text{ GeV}/c$	13112 ± 210	11820 ± 767
$3.4 < p_{D^{*0}}^* < 3.8 \text{ GeV}/c$	24522 ± 298	24489 ± 376
$3.8 < p_{D^{*0}}^* < 4.2 \text{ GeV}/c$	18631 ± 266	18321 ± 301
$4.2 < p_{D^{*0}}^* < 4.6 \text{ GeV}/c$	10975 ± 136	10726 ± 217
$4.6 < p_{D^{*0}}^* < 5.0 \text{ GeV}/c$	3365 ± 93	3143 ± 112

Table 6.3: $D^{*0} \rightarrow D^0 \pi^0$ and $D^{*0} \rightarrow D^0 \gamma$ event yields obtained in the data for different momentum bins.

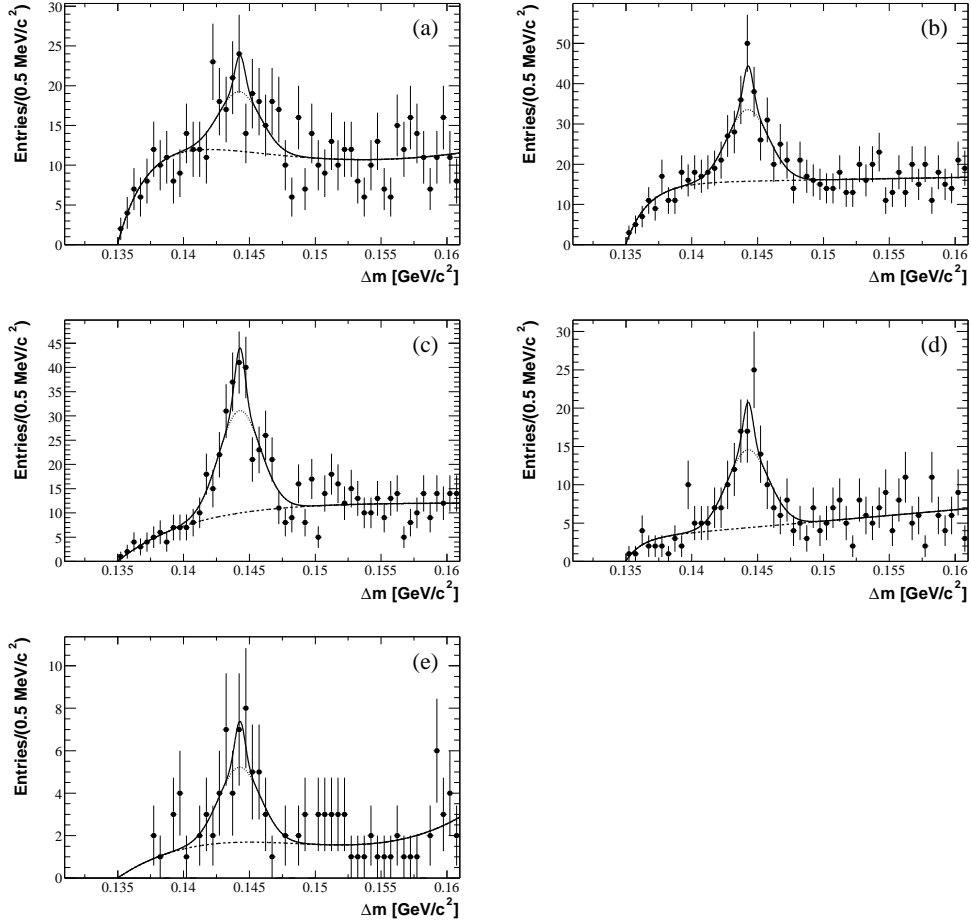


Figure 6.1: $\Delta m_{D_s^+ \pi^0}$ invariant mass difference distributions in different bins of the D_s^{*+} momentum $p_{D_s^{*+}}^*$: (a) $3.0 < p_{D_s^{*+}}^* < 3.4 \text{ GeV}/c$; (b) $3.4 < p_{D_s^{*+}}^* < 3.8 \text{ GeV}/c$; (c) $3.8 < p_{D_s^{*+}}^* < 4.2 \text{ GeV}/c$; (d) $4.2 < p_{D_s^{*+}}^* < 4.6 \text{ GeV}/c$; (e) $4.6 < p_{D_s^{*+}}^* < 5.0 \text{ GeV}/c$. The D_s^+ candidate has been reconstructed with the selection method.

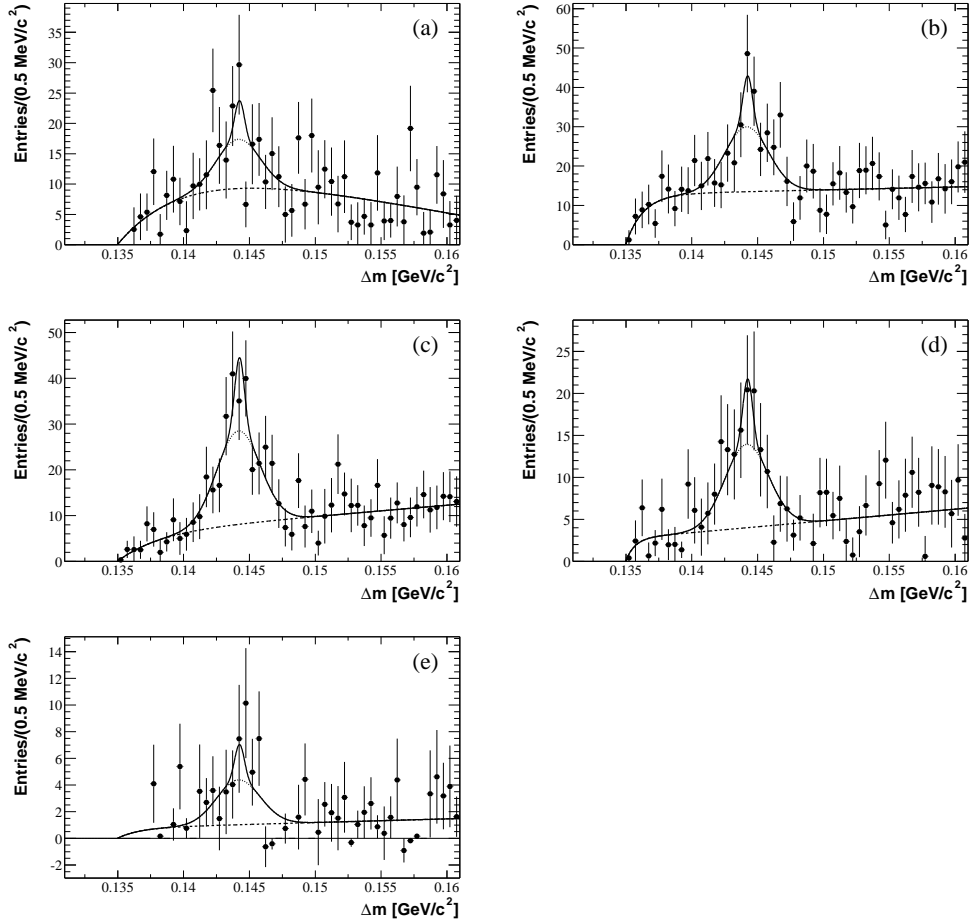


Figure 6.2: $\Delta m_{D_s^+ \pi^0}$ invariant mass difference distributions in different bins of the D_s^{*+} momentum $p_{D_s^{*+}}^*$: (a) $3.0 < p_{D_s^{*+}}^* < 3.4 \text{ GeV}/c$; (b) $3.4 < p_{D_s^{*+}}^* < 3.8 \text{ GeV}/c$; (c) $3.8 < p_{D_s^{*+}}^* < 4.2 \text{ GeV}/c$; (d) $4.2 < p_{D_s^{*+}}^* < 4.6 \text{ GeV}/c$; (e) $4.6 < p_{D_s^{*+}}^* < 5.0 \text{ GeV}/c$. The D_s^+ candidate has been reconstructed with the weighting method.

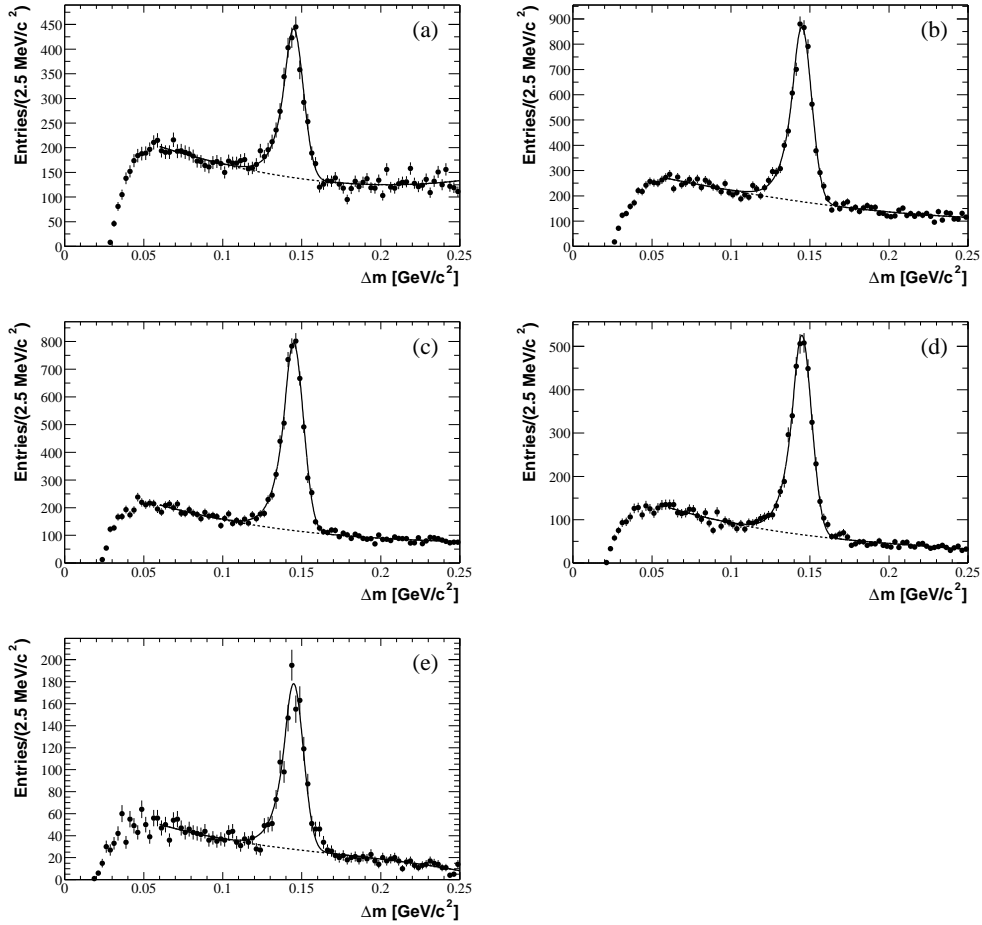


Figure 6.3: $\Delta m_{D_s^+ \gamma}$ invariant mass difference distributions in different bins of the D_s^{*+} momentum $p_{D_s^{*+}}^*$: (a) $3.0 < p_{D_s^{*+}}^* < 3.4 \text{ GeV}/c$; (b) $3.4 < p_{D_s^{*+}}^* < 3.8 \text{ GeV}/c$; (c) $3.8 < p_{D_s^{*+}}^* < 4.2 \text{ GeV}/c$; (d) $4.2 < p_{D_s^{*+}}^* < 4.6 \text{ GeV}/c$; (e) $4.6 < p_{D_s^{*+}}^* < 5.0 \text{ GeV}/c$. The D_s^+ candidate has been reconstructed with the selection method.

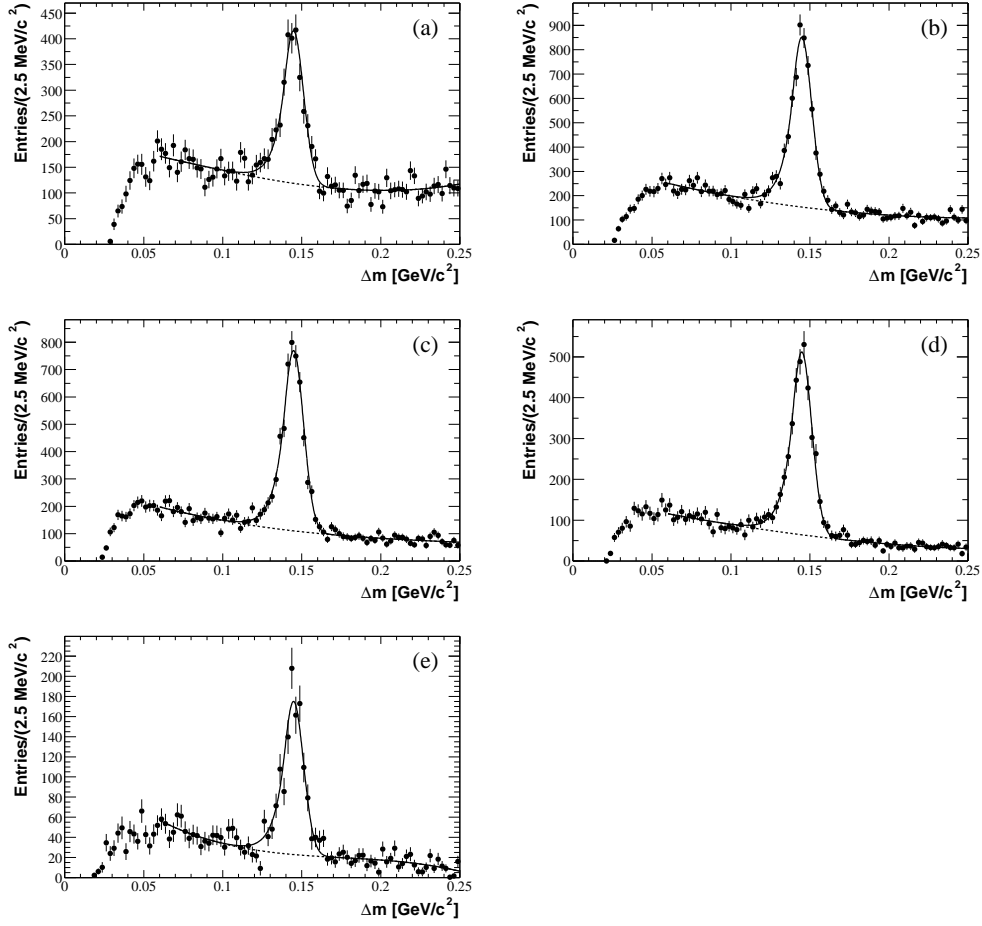


Figure 6.4: $\Delta m_{D_s^+ \gamma}$ invariant mass difference distributions in different bins of the D_s^{*+} momentum $p_{D_s^{*+}}^*$: (a) $3.0 < p_{D_s^{*+}}^* < 3.4$ GeV/c; (b) $3.4 < p_{D_s^{*+}}^* < 3.8$ GeV/c; (c) $3.8 < p_{D_s^{*+}}^* < 4.2$ GeV/c; (d) $4.2 < p_{D_s^{*+}}^* < 4.6$ GeV/c; (e) $4.6 < p_{D_s^{*+}}^* < 5.0$ GeV/c. The D_s^+ candidate has been reconstructed with the weighting method.

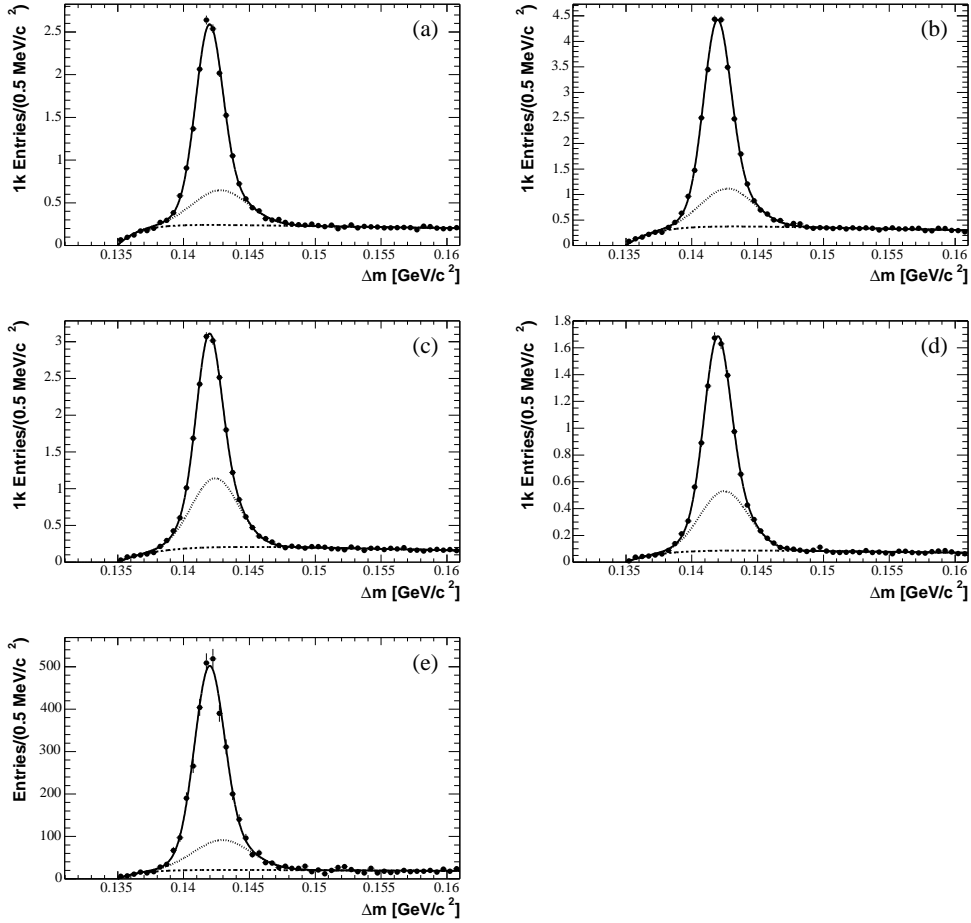


Figure 6.5: $\Delta m_{D^0\pi^0}$ invariant mass difference distributions in different bins of the D^{*0} momentum $p_{D^{*0}}^*$: (a) $3.0 < p_{D^{*0}}^* < 3.4 \text{ GeV}/c$; (b) $3.4 < p_{D^{*0}}^* < 3.8 \text{ GeV}/c$; (c) $3.8 < p_{D^{*0}}^* < 4.2 \text{ GeV}/c$; (d) $4.2 < p_{D^{*0}}^* < 4.6 \text{ GeV}/c$; (e) $4.6 < p_{D^{*0}}^* < 5.0 \text{ GeV}/c$.

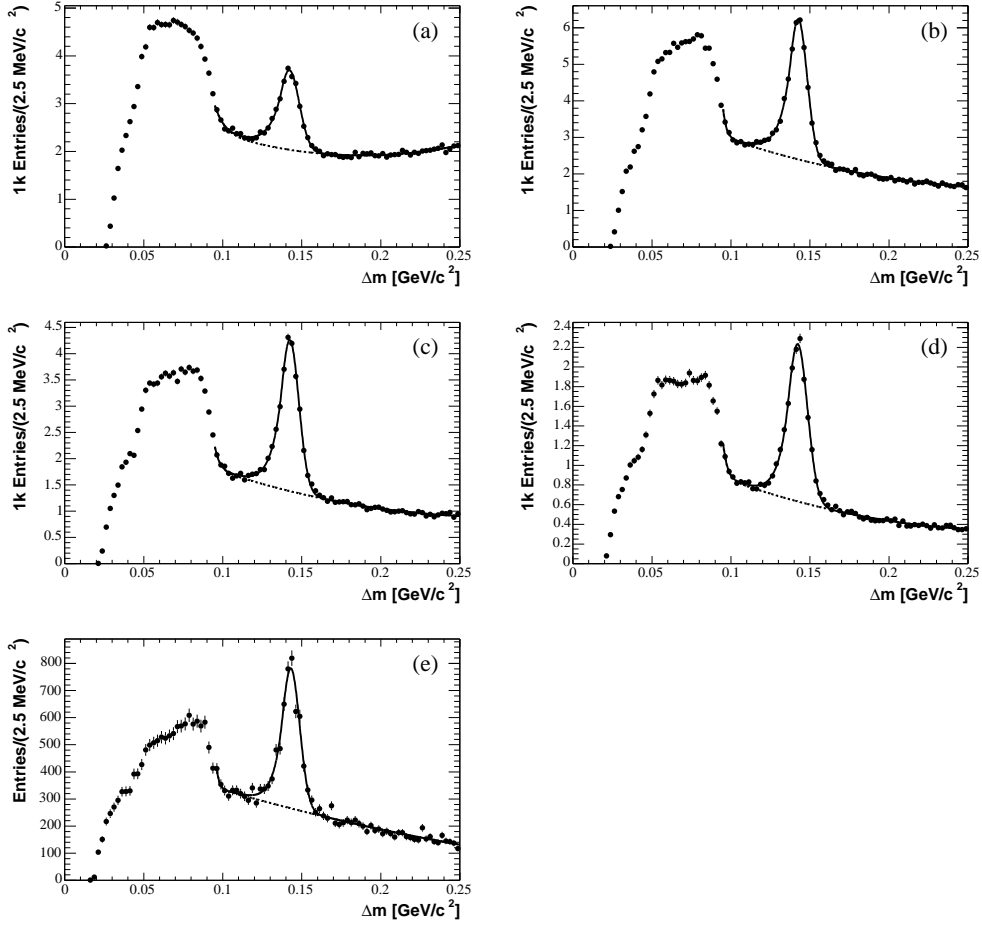


Figure 6.6: $\Delta m_{D^*0 \gamma}$ invariant mass difference distributions in different bins of the D^{*0} momentum $p_{D^{*0}}^*$: (a) $3.0 < p_{D^{*0}}^* < 3.4$ GeV/c; (b) $3.4 < p_{D^{*0}}^* < 3.8$ GeV/c; (c) $3.8 < p_{D^{*0}}^* < 4.2$ GeV/c; (d) $4.2 < p_{D^{*0}}^* < 4.6$ GeV/c; (e) $4.6 < p_{D^{*0}}^* < 5.0$ GeV/c.

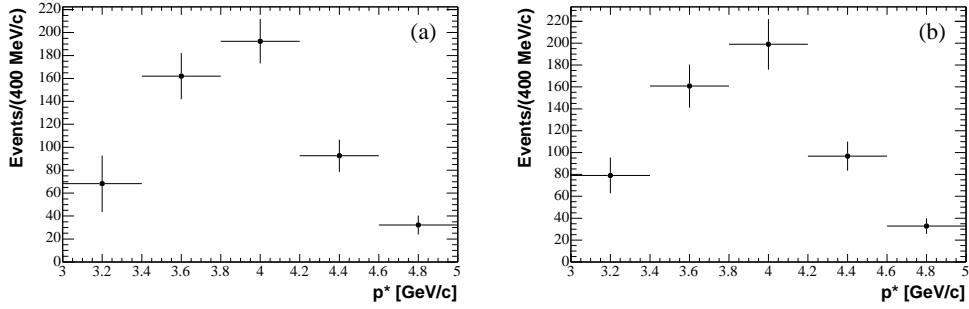


Figure 6.7: Momentum spectra of $D_s^{*+} \rightarrow D_s^+ \pi^0$ event yields in the data: (a) selection method; (b) weighting method.

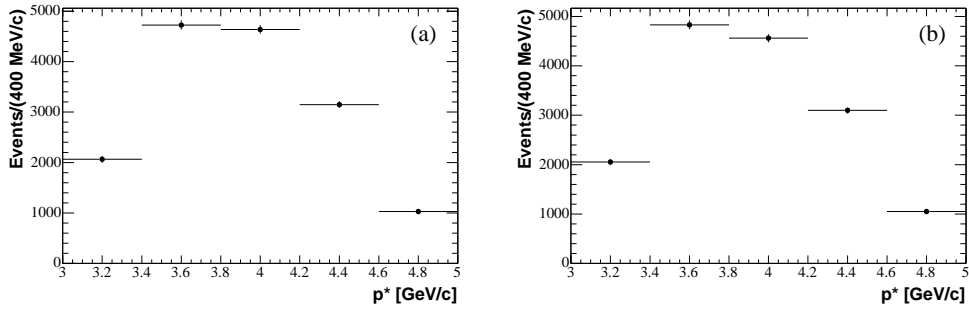


Figure 6.8: Momentum spectra of $D_s^{*+} \rightarrow D_s^+ \gamma$ event yields in the data: (a) selection method; (b) weighting method.

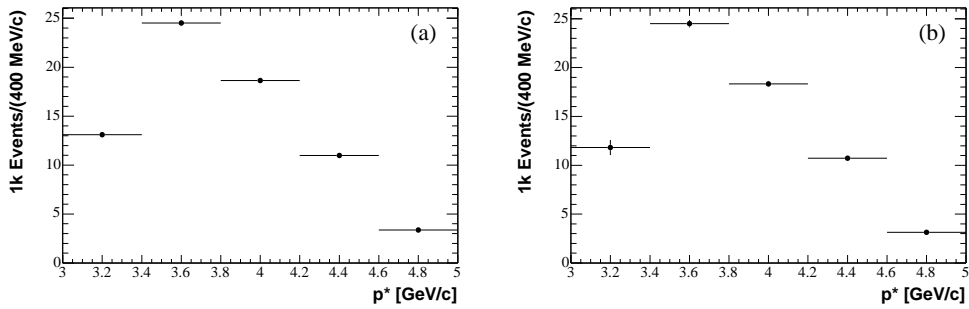


Figure 6.9: Momentum spectra of event yields in the data: (a) $D^{*0} \rightarrow D^0 \pi^0$; (b) $D^{*0} \rightarrow D^0 \gamma$.

6.3 Efficiency Correction

6.3.1 Determination of Momentum Dependent Efficiencies with Signal Monte Carlo Events

To estimate the reconstruction efficiencies in the five momentum bins, the numbers of reconstructed and total events have been counted in the signal Monte Carlo samples. The ratio of the two numbers represents the efficiency. For each channel, this has been performed separately for each momentum bin. Tables 6.4 to 6.9 list the results.

A comparison of the resulting efficiencies is shown in Figure 6.10. Except for the $3.0 < p^* < 3.4 \text{ GeV}/c$ bin, where the efficiencies are reduced by the scaled momentum (x_p) selection of the D_s^+ and D^0 candidates, the efficiencies appear to be momentum independent within the error margins. Therefore, for each decay channel, a constant function has been fitted to the efficiency distributions over the range $3.4 < p^* < 5.0 \text{ GeV}/c$. The results are given in Table 6.10.

It should be noted that these numbers are larger than the total efficiencies presented in Chapter 4. This is expected, as the effect of the scaled momentum selections influences the latter, but not the former efficiencies.

6.3.2 Efficiency Corrected Momentum Spectra

To correct the momentum spectra (Figures 6.7 to 6.9) for different efficiencies, the event yields in the $3.0 < p^* < 3.4 \text{ GeV}/c$ bins are divided by the efficiency in that bin. The event yields in the other bins are divided by the efficiencies according to the respective fit results.

Two theoretical models to describe the momentum distribution have been considered. The first one, by Peterson, Schlatter, Schmitt, and Zerwas [29], models the momentum distribution resulting from the heavy quark fragmentation process by the function

$$f_{\text{PSSZ}}(x_p) = N \frac{1}{x_p \left(1 - \frac{1}{x_p} - \frac{\epsilon}{1-x_p}\right)^2}. \quad (6.1)$$

The second model, by Collins and Spiller [28], refines the first one and describes the momentum distribution by the function

$$f_{\text{CS}}(x_p) = N \frac{\left(\frac{1-x_p}{x_p} + \frac{2-x_p}{1-x_p} \epsilon\right) (1+x_p^2)}{\left(1 - \frac{1}{x_p} - \frac{\epsilon}{1-x_p}\right)^2}. \quad (6.2)$$

Both model functions are fitted to each efficiency corrected momentum spectrum. The results are shown in Figures 6.11 to 6.13. Each fit yields a shape parameter ϵ ; these are tabulated in Table 6.11.

The function by Collins and Spiller models the observed distributions much better than the function by Peterson *et al.* Therefore, the former function is used in Section 6.5 to estimate systematic uncertainties.

	Total Events	Reconstructed Events	Reconstruction Efficiency
$3.0 < p_{D_s^{*+}}^* < 3.4 \text{ GeV}/c$	4 822	216	0.0448 ± 0.0030
$3.4 < p_{D_s^{*+}}^* < 3.8 \text{ GeV}/c$	4 590	374	0.0815 ± 0.0042
$3.8 < p_{D_s^{*+}}^* < 4.2 \text{ GeV}/c$	3 749	338	0.0902 ± 0.0049
$4.2 < p_{D_s^{*+}}^* < 4.6 \text{ GeV}/c$	2 527	238	0.0942 ± 0.0061
$4.6 < p_{D_s^{*+}}^* < 5.0 \text{ GeV}/c$	196	15	0.0765 ± 0.0198

Table 6.4: Momentum dependent number of total events, reconstructed events, and reconstruction efficiency in the $D_s^{*+} \rightarrow D_s^+ \pi^0$ signal Monte Carlo sample, reconstructed with the selection method.

	Total Events	Reconstructed Events	Reconstruction Efficiency
$3.0 < p_{D_s^{*+}}^* < 3.4 \text{ GeV}/c$	4 822	236.2	0.0490 ± 0.0032
$3.4 < p_{D_s^{*+}}^* < 3.8 \text{ GeV}/c$	4 590	390.6	0.0851 ± 0.0043
$3.8 < p_{D_s^{*+}}^* < 4.2 \text{ GeV}/c$	3 749	319.7	0.0853 ± 0.0048
$4.2 < p_{D_s^{*+}}^* < 4.6 \text{ GeV}/c$	2 527	239.0	0.0946 ± 0.0061
$4.6 < p_{D_s^{*+}}^* < 5.0 \text{ GeV}/c$	196	13.4	0.0684 ± 0.0187

Table 6.5: Momentum dependent number of total events, reconstructed events, and reconstruction efficiency in the $D_s^{*+} \rightarrow D_s^+ \pi^0$ signal Monte Carlo sample, reconstructed with the weighting method.

The four shape parameters ϵ of the D_s^{*+} distributions agree within error margins, as do the two D^{*0} shape parameters. For each of the two particles, the weighted average of the individual parameters is calculated, with the squares of the inverse errors as weights. The resulting values,

$$\epsilon_{D_s^{*+}} = 0.0836 \quad (6.3)$$

for the D_s^{*+} , and

$$\epsilon_{D^{*0}} = 0.4505 \quad (6.4)$$

for the D^{*0} , are used in the systematic uncertainty estimate in Section 6.5.

	Total Events	Reconstructed Events	Reconstruction Efficiency
$3.0 < p_{D_s^{*+}}^* < 3.4 \text{ GeV}/c$	4 888	383	0.0784 ± 0.0040
$3.4 < p_{D_s^{*+}}^* < 3.8 \text{ GeV}/c$	4 516	660	0.1461 ± 0.0057
$3.8 < p_{D_s^{*+}}^* < 4.2 \text{ GeV}/c$	4 170	628	0.1506 ± 0.0060
$4.2 < p_{D_s^{*+}}^* < 4.6 \text{ GeV}/c$	2 307	360	0.1560 ± 0.0082
$4.6 < p_{D_s^{*+}}^* < 5.0 \text{ GeV}/c$	298	48	0.1611 ± 0.0232

Table 6.6: Momentum dependent number of total events, reconstructed events, and reconstruction efficiency in the $D_s^{*+} \rightarrow D_s^+ \gamma$ signal Monte Carlo sample, reconstructed with the selection method.

	Total Events	Reconstructed Events	Reconstruction Efficiency
$3.0 < p_{D_s^{*+}}^* < 3.4 \text{ GeV}/c$	4 888	403.5	0.0825 ± 0.0041
$3.4 < p_{D_s^{*+}}^* < 3.8 \text{ GeV}/c$	4 516	707.1	0.1566 ± 0.0059
$3.8 < p_{D_s^{*+}}^* < 4.2 \text{ GeV}/c$	4 170	622.4	0.1493 ± 0.0060
$4.2 < p_{D_s^{*+}}^* < 4.6 \text{ GeV}/c$	2 307	359.1	0.1557 ± 0.0082
$4.6 < p_{D_s^{*+}}^* < 5.0 \text{ GeV}/c$	298	56.2	0.1886 ± 0.0252

Table 6.7: Momentum dependent number of total events, reconstructed events, and reconstruction efficiency in the $D_s^{*+} \rightarrow D_s^+ \gamma$ signal Monte Carlo sample, reconstructed with the weighting method.

	Total Events	Reconstructed Events	Reconstruction Efficiency
$3.0 < p_{D^{*0}}^* < 3.4 \text{ GeV}/c$	4 918	216	0.0439 ± 0.0030
$3.4 < p_{D^{*0}}^* < 3.8 \text{ GeV}/c$	4 227	398	0.0942 ± 0.0047
$3.8 < p_{D^{*0}}^* < 4.2 \text{ GeV}/c$	3 281	301	0.0917 ± 0.0053
$4.2 < p_{D^{*0}}^* < 4.6 \text{ GeV}/c$	2 049	179	0.0874 ± 0.0065
$4.6 < p_{D^{*0}}^* < 5.0 \text{ GeV}/c$	386	43	0.1114 ± 0.0170

Table 6.8: Momentum dependent number of total events, reconstructed events, and reconstruction efficiency in the $D^{*0} \rightarrow D^0 \pi^0$ signal Monte Carlo sample.

	Total Events	Reconstructed Events	Reconstruction Efficiency
$3.0 < p_{D^{*0}}^* < 3.4 \text{ GeV}/c$	5 017	332	0.0662 ± 0.0036
$3.4 < p_{D^{*0}}^* < 3.8 \text{ GeV}/c$	4 313	712	0.1651 ± 0.0062
$3.8 < p_{D^{*0}}^* < 4.2 \text{ GeV}/c$	3 185	544	0.1708 ± 0.0073
$4.2 < p_{D^{*0}}^* < 4.6 \text{ GeV}/c$	1 928	334	0.1732 ± 0.0095
$4.6 < p_{D^{*0}}^* < 5.0 \text{ GeV}/c$	418	64	0.1531 ± 0.0191

Table 6.9: Momentum dependent number of total events, reconstructed events, and reconstruction efficiency in the $D^{*0} \rightarrow D^0\gamma$ signal Monte Carlo sample.

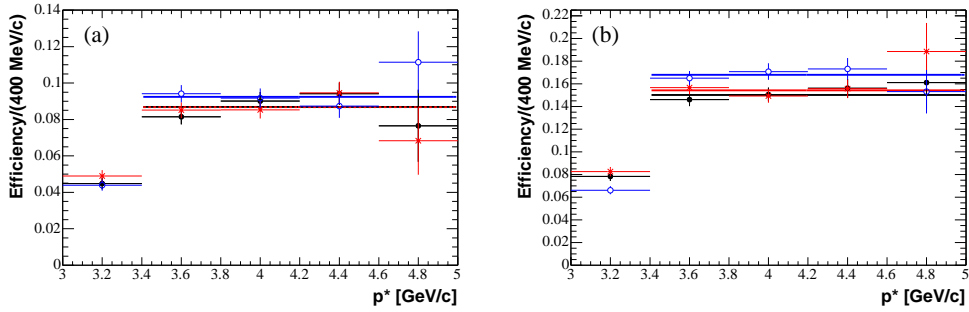


Figure 6.10: Momentum dependent efficiencies from signal Monte Carlo events: (a) hadronic decays: $D_s^{*+} \rightarrow D_s^+\pi^0$, selection method (black, dot markers); $D_s^{*+} \rightarrow D_s^+\pi^0$, weighting method (red, cross markers); $D^{*0} \rightarrow D^0\pi^0$ (blue, open circle markers); (b) radiative decays: $D_s^{*+} \rightarrow D_s^+\gamma$, selection method (black, dot markers); $D_s^{*+} \rightarrow D_s^+\gamma$, weighting method (red, cross markers); $D^{*0} \rightarrow D^0\gamma$ (blue, open circle markers). The horizontal lines represent the results of fits of constant functions in the range $3.4 < p^* < 5.0 \text{ GeV}/c$.

Decay Channel	Efficiency
$D_s^{*+} \rightarrow D_s^+\pi^0$, selection method	0.0869 ± 0.0028
$D_s^{*+} \rightarrow D_s^+\pi^0$, weighting method	0.0868 ± 0.0028
$D^{*0} \rightarrow D^0\pi^0$	0.0924 ± 0.0030
$D_s^{*+} \rightarrow D_s^+\gamma$, selection method	0.1501 ± 0.0036
$D_s^{*+} \rightarrow D_s^+\gamma$, weighting method	0.1543 ± 0.0037
$D^{*0} \rightarrow D^0\gamma$	0.1679 ± 0.0041

Table 6.10: Results of the fit of a constant function to the momentum dependent efficiencies determined from signal Monte Carlo events in the range $3.4 < p^* < 5.0 \text{ GeV}/c$.

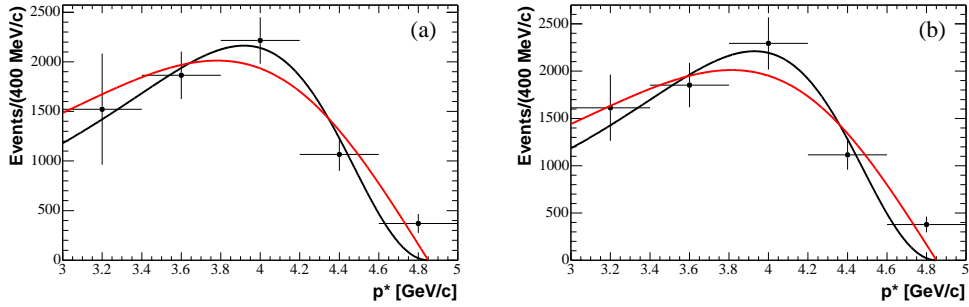


Figure 6.11: Efficiency corrected momentum spectra of $D_s^{*+} \rightarrow D_s^+ \pi^0$ event yields in the data: (a) selection method; (b) weighting method. The functions are fits of the momentum distribution models by Peterson *et al.* (black) and Collins and Spiller (red).

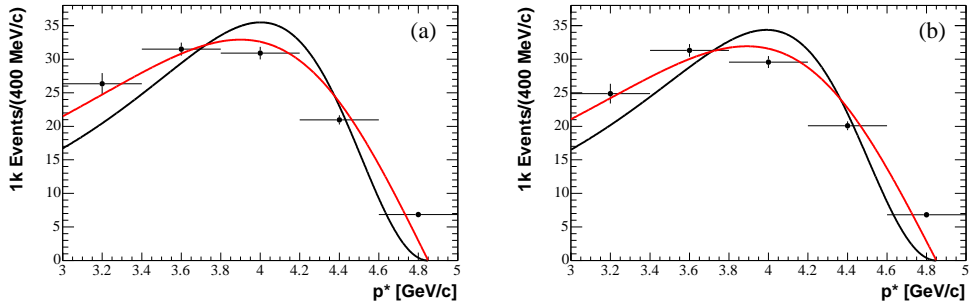


Figure 6.12: Efficiency corrected momentum spectra of $D_s^{*+} \rightarrow D_s^+ \gamma$ event yields in the data: (a) selection method; (b) weighting method. The functions are fits of the momentum distribution models by Peterson *et al.* (black) and Collins and Spiller (red).

Decay Channel	ϵ (Peterson <i>et al.</i>)	ϵ (Collins and Spiller)
$D_s^{*+} \rightarrow D_s^+ \pi^0$, selection method	0.0458 ± 0.0088	0.1132 ± 0.0413
$D_s^{*+} \rightarrow D_s^+ \pi^0$, weighting method	0.0445 ± 0.0076	0.1042 ± 0.0327
$D^{*0} \rightarrow D^0 \pi^0$	0.0639 ± 0.0041	0.4125 ± 0.0781
$D_s^{*+} \rightarrow D_s^+ \gamma$, selection method	0.0371 ± 0.0018	0.0817 ± 0.0067
$D_s^{*+} \rightarrow D_s^+ \gamma$, weighting method	0.0381 ± 0.0019	0.0838 ± 0.0068
$D^{*0} \rightarrow D^0 \gamma$	0.0674 ± 0.0039	0.5449 ± 0.1232

Table 6.11: Results of the fits of theoretical model functions to the measured and efficiency corrected momentum spectra.

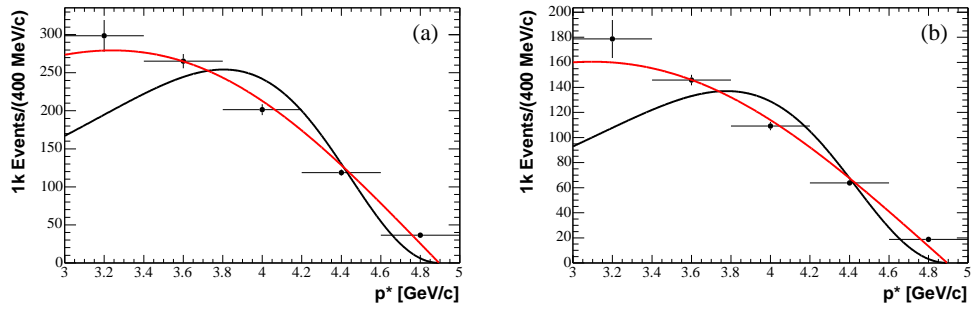


Figure 6.13: Efficiency corrected momentum spectra of event yields in the data: (a) $D^{*0} \rightarrow D^0 \pi^0$; (b) $D^{*0} \rightarrow D^0 \gamma$. The functions are fits of the momentum distribution models by Peterson *et al.* (black) and Collins and Spiller (red).

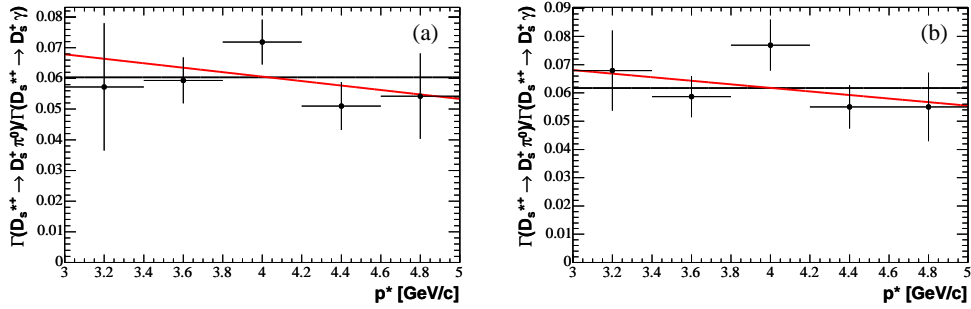


Figure 6.14: Momentum dependent $\Gamma(D_s^{*+} \rightarrow D_s^+ \pi^0) / \Gamma(D_s^{*+} \rightarrow D_s^+ \gamma)$ with efficiencies from signal Monte Carlo events, and results of the fits of a constant function (black) and a first-order polynomial (red): (a) selection method; (b) weighting method. Errors are statistical only.

6.4 Momentum Dependent Partial Widths Ratios

For each momentum bin, the partial widths ratios $\Gamma(D_s^{*+} \rightarrow D_s^+ \pi^0) / \Gamma(D_s^{*+} \rightarrow D_s^+ \gamma)$ and $\Gamma(D^{*0} \rightarrow D^0 \pi^0) / \Gamma(D^{*0} \rightarrow D^0 \gamma)$ have been calculated in the same way as described in Chapter 4. The results are shown in Figures 6.14 to 6.16 and Tables 6.12 to 6.14.

A constant function has been fitted to each partial widths ratio distribution (black line in Figures 6.14 to 6.16). The resulting values are in good agreement with the respective partial widths ratios calculated from all events.

Additionally, a first-order polynomial has been fitted to each partial widths ratio distribution (red line in Figures 6.14 to 6.16). In each case, the slope of the polynomial is compatible with zero within error margins.

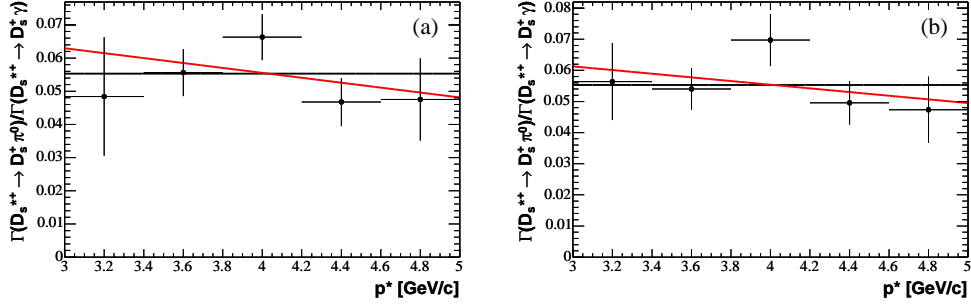


Figure 6.15: Momentum dependent $\Gamma(D_s^{*+} \rightarrow D_s^+ \pi^0) / \Gamma(D_s^{*+} \rightarrow D_s^+ \gamma)$ with efficiencies from D^{*0} decays, and results of the fits of a constant function (black) and a first-order polynomial (red): (a) selection method; (b) weighting method. Errors are statistical only.

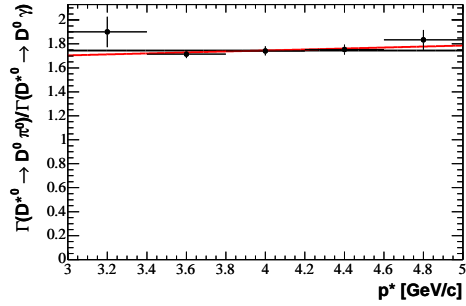


Figure 6.16: Momentum dependent $\Gamma(D^{*0} \rightarrow D^0 \pi^0) / \Gamma(D^{*0} \rightarrow D^0 \gamma)$ with efficiencies from signal Monte Carlo events, and results of the fits of a constant function (black) and a first-order polynomial (red). Errors are statistical only.

	$\Gamma(D_s^{*+} \rightarrow D_s^+ \pi^0)/\Gamma(D_s^{*+} \rightarrow D_s^+ \gamma)$	
	Selection Method	Weighting Method
$3.0 < p_{D_s^{*+}}^* < 3.4 \text{ GeV}/c$	0.0572 ± 0.0208	0.0679 ± 0.0142
$3.4 < p_{D_s^{*+}}^* < 3.8 \text{ GeV}/c$	0.0594 ± 0.0075	0.0587 ± 0.0073
$3.8 < p_{D_s^{*+}}^* < 4.2 \text{ GeV}/c$	0.0719 ± 0.0073	0.0769 ± 0.0090
$4.2 < p_{D_s^{*+}}^* < 4.6 \text{ GeV}/c$	0.0510 ± 0.0078	0.0550 ± 0.0076
$4.6 < p_{D_s^{*+}}^* < 5.0 \text{ GeV}/c$	0.0542 ± 0.0139	0.0550 ± 0.0121
Fit of constant	0.0604 ± 0.0041	0.0617 ± 0.0041
Fit of first-order polynomial: a : slope $\times \text{GeV}/c$ b : ordinate intercept	$(-7.27 \pm 9.89) \times 10^{-3}$ 0.0897 ± 0.0400	$(-6.30 \pm 8.67) \times 10^{-3}$ 0.0870 ± 0.0350
All Events (cf. Table 4.22)	0.0621 ± 0.0049	0.0653 ± 0.0048

Table 6.12: Momentum dependent $\Gamma(D_s^{*+} \rightarrow D_s^+ \pi^0)/\Gamma(D_s^{*+} \rightarrow D_s^+ \gamma)$ with efficiencies from signal Monte Carlo events, results of the fits to the momentum spectra, and $\Gamma(D_s^{*+} \rightarrow D_s^+ \pi^0)/\Gamma(D_s^{*+} \rightarrow D_s^+ \gamma)$ for all events. Errors are statistical only.

	$\Gamma(D_s^{*+} \rightarrow D_s^+ \pi^0)/\Gamma(D_s^{*+} \rightarrow D_s^+ \gamma)$	
	Selection Method	Weighting Method
$3.0 < p_{D_s^{*+}}^* < 3.4 \text{ GeV}/c$	0.0484 ± 0.0179	0.0564 ± 0.0124
$3.4 < p_{D_s^{*+}}^* < 3.8 \text{ GeV}/c$	0.0556 ± 0.0071	0.0540 ± 0.0068
$3.8 < p_{D_s^{*+}}^* < 4.2 \text{ GeV}/c$	0.0663 ± 0.0069	0.0697 ± 0.0083
$4.2 < p_{D_s^{*+}}^* < 4.6 \text{ GeV}/c$	0.0467 ± 0.0072	0.0495 ± 0.0070
$4.6 < p_{D_s^{*+}}^* < 5.0 \text{ GeV}/c$	0.0475 ± 0.0124	0.0474 ± 0.0106
Fit of constant	0.0553 ± 0.0038	0.0553 ± 0.0037
Fit of first-order polynomial: a : slope $\times \text{GeV}/c$ b : ordinate intercept	$(-7.42 \pm 9.00) \times 10^{-3}$ 0.0852 ± 0.0365	$(-5.89 \pm 7.77) \times 10^{-3}$ 0.0789 ± 0.0314
All Events (cf. Table 4.22)	0.0574 ± 0.0046	0.0593 ± 0.0044

Table 6.13: Momentum dependent $\Gamma(D_s^{*+} \rightarrow D_s^+ \pi^0)/\Gamma(D_s^{*+} \rightarrow D_s^+ \gamma)$ with efficiencies from D^{*0} decays, results of the fits to the momentum spectra, and $\Gamma(D_s^{*+} \rightarrow D_s^+ \pi^0)/\Gamma(D_s^{*+} \rightarrow D_s^+ \gamma)$ for all events. Errors are statistical only.

	$\Gamma(D^{*0} \rightarrow D^0\pi^0)/\Gamma(D^{*0} \rightarrow D^0\gamma)$
$3.0 < p_{D_s^{*+}}^* < 3.4 \text{ GeV}/c$	1.9000 ± 0.1270
$3.4 < p_{D_s^{*+}}^* < 3.8 \text{ GeV}/c$	1.7151 ± 0.0336
$3.8 < p_{D_s^{*+}}^* < 4.2 \text{ GeV}/c$	1.7417 ± 0.0379
$4.2 < p_{D_s^{*+}}^* < 4.6 \text{ GeV}/c$	1.7527 ± 0.0416
$4.6 < p_{D_s^{*+}}^* < 5.0 \text{ GeV}/c$	1.8342 ± 0.0829
Fit of constant	1.7443 ± 0.0205
Fit of first-order polynomial:	
a : slope $\times \text{GeV}/c$	$(41.0 \pm 52.3) \times 10^{-3}$
b : ordinate intercept	1.5811 ± 0.2089
All Events (cf. Equation 4.54)	1.7401 ± 0.0204

Table 6.14: Momentum dependent $\Gamma(D^{*0} \rightarrow D^0\pi^0)/\Gamma(D^{*0} \rightarrow D^0\gamma)$ with efficiencies from signal Monte Carlo events, results of the fits to the momentum spectrum, and $\Gamma(D_s^{*+} \rightarrow D_s^+\pi^0)/\Gamma(D_s^{*+} \rightarrow D_s^+\gamma)$ for all events. Errors are statistical only.

6.5 Systematic Momentum Dependency

Systematic uncertainties are calculated under the assumption that the slopes of the first-order polynomials (referred to as $p_1(x_p) = ax_p + b$ in the following text) fitted to the partial widths ratio distributions represent systematic momentum dependencies. Such dependencies could arise due to unknown momentum dependencies of the efficiencies which do not compensate in the partial widths ratios and which are not correctly modeled by the signal Monte Carlo events. The method described here yields a conservative estimate of the uncertainties such unknown dependencies could cause.

Under the assumption stated above, if the partial width ratios had been measured in n bins which covered the allowed momentum range ($0 \leq x_p \leq 1$) completely, the partial width ratio in the i th bin ($i \in \{1, \dots, n\}$) would be given by

$$(\Gamma_{\pi^0}/\Gamma_\gamma)_i = p_1(x_{p,i}) = ax_{p,i} + b, \quad (6.5)$$

where $x_{p,i}$ is the scaled momentum x_p at the center of the i th bin.

In the case of $\Gamma(D_s^{*+} \rightarrow D_s^+\pi^0)/\Gamma(D_s^{*+} \rightarrow D_s^+\gamma)$ with efficiencies determined with signal Monte Carlo events, the relative statistical error of the i th bin would be

$$\frac{\sigma_i}{(\Gamma_{\pi^0}/\Gamma_\gamma)_i} = \sqrt{\frac{1}{N_i(D_s^+\pi^0)} + \frac{1}{N_i(D_s^+\gamma)}}. \quad (6.6)$$

$N_i(D_s^+\pi^0)$ and $N_i(D_s^+\gamma)$ are the event yields of $D_s^{*+} \rightarrow D_s^+\pi^0$ and $D_s^{*+} \rightarrow D_s^+\gamma$, respectively, in the i th bin. Except for unknown normalization factors, these yields are given by the momentum distribution function $f_{\text{CS},D_s^{*+}}$ (Equation 6.2), with the shape parameter $\epsilon_{D_s^{*+}} = 0.0836$ as given by Equation 6.3.

The squares of the absolute errors are therefore proportional to

$$\sigma_i^2 \propto \frac{(ax_{p,i} + b)^2}{f_{\text{CS},D_s^{*+}}(x_{p,i})}. \quad (6.7)$$

The total partial widths ratio $\Gamma(D_s^{*+} \rightarrow D_s^+\pi^0)/\Gamma(D_s^{*+} \rightarrow D_s^+\gamma)$ could be calculated as the weighted sum of the values in the n bins, with the inverse squares of the errors as weights:¹

$$(\Gamma_{\pi^0}/\Gamma_\gamma)_{\text{mom.dep}} = \sum_{i=1}^n \frac{ax_{p,i} + b}{\sigma_i^2} \bigg/ \sum_{i=1}^n \frac{1}{\sigma_i^2}. \quad (6.8)$$

In the limit $n \rightarrow \infty$ and with the unknown proportionality constant in σ_i^2 cancelled, this becomes

$$(\Gamma_{\pi^0}/\Gamma_\gamma)_{\text{mom.dep}} = \int_0^1 dx_p \frac{f_{\text{CS},D_s^{*+}}(x_p)}{ax_p + b} \bigg/ \int_0^1 dx_p \frac{f_{\text{CS},D_s^{*+}}(x_p)}{(ax_p + b)^2}. \quad (6.9)$$

¹This is mathematically equivalent to fitting a constant function to the partial widths ratio distribution.

In the case of $\Gamma(D_s^{*+} \rightarrow D_s^+ \pi^0)/\Gamma(D_s^{*+} \rightarrow D_s^+ \gamma)$ with efficiencies determined with D^{*0} decays, the relative statistical error of the i th bin would be

$$\frac{\sigma_i}{(\Gamma_{\pi^0}/\Gamma_\gamma)_i} = \sqrt{\frac{1}{N_i(D_s^+ \pi^0)} + \frac{1}{N_i(D_s^+ \gamma)} + \frac{1}{N_i(D^0 \pi^0)} + \frac{1}{N_i(D^0 \gamma)}}. \quad (6.10)$$

This case is slightly more complicated due to the different momentum spectra of the D_s^{*+} and D^{*0} particles: there is no common momentum distribution function to factor out. Instead, the N_i are assumed to be proportional to the measured event yields N , and the different normalizations of the momentum distribution functions $f_{\text{CS},D_s^{*+}}$ (cf. Equation 6.3) for the D_s^{*+} decays and $f_{\text{CS},D^{*0}}$ (cf. Equation 6.4) for the D^{*0} decays are taken into account:

$$N_i(D_s^+ \pi^0) \propto N(D_s^{*+} \rightarrow D_s^+ \pi^0) f_{\text{CS},D_s^{*+}}(x_{p,i}) \left/ \int_0^1 dx_p f_{\text{CS},D_s^{*+}}(x_p) \right.; \quad (6.11)$$

$$N_i(D_s^+ \gamma) \propto N(D_s^{*+} \rightarrow D_s^+ \gamma) f_{\text{CS},D_s^{*+}}(x_{p,i}) \left/ \int_0^1 dx_p f_{\text{CS},D_s^{*+}}(x_p) \right.; \quad (6.12)$$

$$N_i(D^0 \pi^0) \propto N(D^{*0} \rightarrow D^0 \pi^0) f_{\text{CS},D^{*0}}(x_{p,i}) \left/ \int_0^1 dx_p f_{\text{CS},D^{*0}}(x_p) \right.; \quad (6.13)$$

$$N_i(D^0 \gamma) \propto N(D^{*0} \rightarrow D^0 \gamma) f_{\text{CS},D^{*0}}(x_{p,i}) \left/ \int_0^1 dx_p f_{\text{CS},D^{*0}}(x_p) \right. . \quad (6.14)$$

With the measured event yields given in Tables 4.10, 4.12, 4.17, and 4.19, and the normalizations of the momentum distribution functions

$$\int_0^1 dx_p f_{\text{CS},D_s^{*+}}(x_p) = 0.0930, \quad (6.15)$$

$$\int_0^1 dx_p f_{\text{CS},D^{*0}}(x_p) = 0.5186, \quad (6.16)$$

the squares of the absolute errors of the partial widths ratios are proportional to

$$\sigma_i^2 \propto (ax_{p,i} + b)^2 \left(\frac{1.72 \times 10^{-4}}{f_{\text{CS},D_s^{*+}}(x_{p,i})} + \frac{1.52 \times 10^{-5}}{f_{\text{CS},D^{*0}}(x_{p,i})} \right) \quad (6.17)$$

for the selection method and

$$\sigma_i^2 \propto (ax_{p,i} + b)^2 \left(\frac{1.67 \times 10^{-4}}{f_{\text{CS},D_s^{*+}}(x_{p,i})} + \frac{1.52 \times 10^{-5}}{f_{\text{CS},D^{*0}}(x_{p,i})} \right) \quad (6.18)$$

for the weighting method.

If again the limit $n \rightarrow \infty$ is performed and the unknown proportionality constant in σ_i^2 cancelled, the equations

$$(\Gamma_{\pi^0}/\Gamma_{\gamma})_{\text{mom.dep}} = \int_0^1 dx_p \frac{\left(\frac{1.72 \times 10^{-4}}{f_{\text{CS}, D_s^{*+}}(x_p)} + \frac{1.52 \times 10^{-5}}{f_{\text{CS}, D^{*0}}(x_p)} \right)^{-1}}{ax_p + b} \Bigg/ \int_0^1 dx_p \frac{\left(\frac{1.72 \times 10^{-4}}{f_{\text{CS}, D_s^{*+}}(x_p)} + \frac{1.52 \times 10^{-5}}{f_{\text{CS}, D^{*0}}(x_p)} \right)^{-1}}{(ax_p + b)^2} \quad (6.19)$$

for the selection method and

$$(\Gamma_{\pi^0}/\Gamma_{\gamma})_{\text{mom.dep}} = \int_0^1 dx_p \frac{\left(\frac{1.67 \times 10^{-4}}{f_{\text{CS}, D_s^{*+}}(x_p)} + \frac{1.52 \times 10^{-5}}{f_{\text{CS}, D^{*0}}(x_p)} \right)^{-1}}{ax_p + b} \Bigg/ \int_0^1 dx_p \frac{\left(\frac{1.67 \times 10^{-4}}{f_{\text{CS}, D_s^{*+}}(x_p)} + \frac{1.52 \times 10^{-5}}{f_{\text{CS}, D^{*0}}(x_p)} \right)^{-1}}{(ax_p + b)^2} \quad (6.20)$$

for the weighting method are obtained.

Finally, the case of $\Gamma(D^{*0} \rightarrow D^0 \pi^0)/\Gamma(D^{*0} \rightarrow D^0 \gamma)$ with efficiencies determined with signal Monte Carlo events is very similar to $\Gamma(D_s^{*+} \rightarrow D_s^+ \pi^0)/\Gamma(D_s^{*+} \rightarrow D_s^+ \gamma)$ with efficiencies determined with signal Monte Carlo events:

$$(\Gamma_{\pi^0}/\Gamma_{\gamma})_{\text{mom.dep}} = \int_0^1 dx_p \frac{f_{\text{CS}, D^{*0}}(x_p)}{ax_p + b} \Bigg/ \int_0^1 dx_p \frac{f_{\text{CS}, D^{*0}}(x_p)}{(ax_p + b)^2}. \quad (6.21)$$

The numbers obtained in this way for the momentum dependent partial widths ratios $(\Gamma_{\pi^0}/\Gamma_{\gamma})_{\text{mom.dep}}$ are compared with the results of the fits of a constant function to the partial widths ratio distributions, which represent the assumption that no momentum dependencies exist. The differences are taken as systematic uncertainties. Table 6.15 shows the results.

Partial Widths Ratio	$(\Gamma_{\pi^0}/\Gamma_{\gamma})_{\text{mom.dep}}$	Constant Function Fit	Relative Difference
$\Gamma(D_s^{*+} \rightarrow D_s^+ \pi^0)/\Gamma(D_s^{*+} \rightarrow D_s^+ \gamma)$, selection method, eff. from signal Monte Carlo	0.0644	0.0604	6.80%
$\Gamma(D_s^{*+} \rightarrow D_s^+ \pi^0)/\Gamma(D_s^{*+} \rightarrow D_s^+ \gamma)$, weighting method, eff. from signal Monte Carlo	0.0653	0.0617	5.83%
$\Gamma(D_s^{*+} \rightarrow D_s^+ \pi^0)/\Gamma(D_s^{*+} \rightarrow D_s^+ \gamma)$, selection method, eff. from D^{*0} decays	0.0599	0.0553	8.33%
$\Gamma(D_s^{*+} \rightarrow D_s^+ \pi^0)/\Gamma(D_s^{*+} \rightarrow D_s^+ \gamma)$, weighting method, eff. from D^{*0} decays	0.0590	0.0553	6.82%
$\Gamma(D^{*0} \rightarrow D^0 \pi^0)/\Gamma(D^{*0} \rightarrow D^0 \gamma)$	1.6966	1.7443	2.77%

Table 6.15: Comparison of momentum dependent partial widths ratios $(\Gamma_{\pi^0}/\Gamma_{\gamma})_{\text{mom.dep}}$ (see text for details) and fits of a constant function to the partial widths ratio distributions. The relative difference represents a systematic momentum dependency.

Chapter 7

Systematic Uncertainties

Various sources of systematic uncertainties have been identified in the previous chapters. They are summarized here.

7.1 Systematic Uncertainties on

$$\Gamma(D_s^{*+} \rightarrow D_s^+ \pi^0) / \Gamma(D_s^{*+} \rightarrow D_s^+ \gamma)$$

There is an uncertainty of 3.2% for the selection method and 5.9% for the weighting method in the D_s^+ background shape of the $D_s^{*+} \rightarrow D_s^+ \pi^0$ signal, as described in Section 5.1.1. The π^0 background shape of the same channel has an uncertainty of 3.1% for the selection method and 2.9% for the weighting method (see Section 5.3.2). These uncertainties do not depend on how the efficiency ratio is determined (signal Monte Carlo events or D^{*0} decays), therefore they are common to both efficiency ratio methods.

If the efficiency ratio is determined with signal Monte Carlo events, the limited statistics of these events are a systematic uncertainty. It contributes 5.0% and 5.2% to the total uncertainty for the selection and weighting method, respectively, as described in Section 4.8.1. The same section also explains how uncertainties in the Monte Carlo model influence the efficiency ratio. They amount to 3.6% uncertainty for the selection method and 7.4% for the weighting method.

For the efficiency ratio determination from D^{*0} decays, it must be taken into account that the uncertainties in the branching fractions $\mathcal{B}(D^{*0} \rightarrow D^0 \pi^0)$ and $\mathcal{B}(D^{*0} \rightarrow D^0 \gamma)$ are correlated, as detailed in Section 4.9.4. This results in an uncertainty of 12.3% in the ratio of the branching fractions.

There is also a small uncertainty of 0.1% in the π^0 background shape for the $D^{*0} \rightarrow D^0 \pi^0$ signal (see Section 5.3.2).

Potentially unknown momentum dependencies of the efficiencies have been estimated as described in Section 6.5. If the efficiency ratio is determined with signal Monte Carlo events, they amount to 6.8% and 5.8% for the selection and weighting method, respectively. For the efficiency ratio determination from D^{*0} decays, the uncertainty is 8.3% for the selection method and 6.8% for the weighting method.

	Efficiencies from Signal Monte Carlo	
	Selection Method	Weighting Method
$D_s^{*+} \rightarrow D_s^+ \pi^0$: D_s^+ Background Shape	3.2%	5.9%
$D_s^{*+} \rightarrow D_s^+ \pi^0$: π^0 Background Shape	3.1%	2.9%
Signal Monte Carlo Statistics	5.0%	5.2%
Monte Carlo Model Uncertainty	3.6%	7.4%
Momentum Dependency	6.8%	5.8%
Total	10.2%	12.6%
	Efficiencies from D^{*0} Decays	
	Selection Method	Weighting Method
$D_s^{*+} \rightarrow D_s^+ \pi^0$: D_s^+ Background Shape	3.2%	5.9%
$D_s^{*+} \rightarrow D_s^+ \pi^0$: π^0 Background Shape	3.1%	2.9%
D^{*0} Branching Fractions		12.3%
$D^{*0} \rightarrow D^0 \pi^0$: π^0 Background Shape		0.1%
Momentum Dependency	8.3%	6.8%
Total	15.5%	15.5%

Table 7.1: Summary of systematic uncertainties on $\Gamma(D_s^{*+} \rightarrow D_s^+ \pi^0)/\Gamma(D_s^{*+} \rightarrow D_s^+ \gamma)$.

The systematic uncertainties are summarized in Table 7.1. The uncertainties for the efficiency ratio determination with D^{*0} decays are dominated by the uncertainties in the D^{*0} branching fractions. If the knowledge about these branching fractions is improved by future measurements, this method of efficiency determination could potentially be superior to the efficiency determination from Monte Carlo events.

While the weighting method has smaller statistical errors than the selection method, its systematic uncertainties can be larger. Specifically, this should be expected for the D_s^+ background. The weighting method does not remove any background events, so that *more* events contribute than for the selection method. While the positive and negative weights cause the background events to mostly cancel, this is not the case for the errors, which add up (in quadrature). Therefore, the D_s^+ background distribution has less entries, but larger errors in each bin for the weighting method compared to the selection method.

$D^{*0} \rightarrow D^0\pi^0$: π^0 Background Shape	0.1%
Signal Monte Carlo Statistics	5.4%
Monte Carlo Model Uncertainty	3.8%
Momentum Dependency	2.8%
Total	7.2%

Table 7.2: Summary of systematic uncertainties on $\Gamma(D^{*0} \rightarrow D^0\pi^0)/\Gamma(D^{*0} \rightarrow D^0\gamma)$.

7.2 Systematic Uncertainties on $\Gamma(D^{*0} \rightarrow D^0\pi^0)/\Gamma(D^{*0} \rightarrow D^0\gamma)$

The 0.1% uncertainty in the π^0 background shape for the $D^{*0} \rightarrow D^0\pi^0$ signal, which has already been mentioned in the previous section, also contributes to the $\Gamma(D^{*0} \rightarrow D^0\pi^0)/\Gamma(D^{*0} \rightarrow D^0\gamma)$ uncertainty.

The limited statistics of signal Monte Carlo events is another source of uncertainty (see Section 4.9.5); it amounts to 5.4%. Uncertainties in the Monte Carlo model contribute with 3.8%; Section 4.9.5 explains how this value has been determined.

Potentially unknown momentum dependencies of the efficiencies are estimated to contribute 2.8% to the uncertainty, as described in Section 6.5.

Table 7.2 summarizes the systematic uncertainties. If the individual uncertainties are summed in quadrature, a total uncertainty of 7.2% is obtained.

Chapter 8

Summary and Results

Using 90.40 fb^{-1} of *BABAR* data, the branching fraction ratio $\Gamma(D_s^{*+} \rightarrow D_s^+ \pi^0) / \Gamma(D_s^{*+} \rightarrow D_s^+ \gamma)$ has been measured with four different combinations of methods.

The ‘selection method’ and ‘weighting method’ both exploit the fact that when the D_s^+ meson decays to a ϕ and a π^+ meson, the ϕ meson is polarized, so that its decay products show a characteristic angular distribution. This is expressed by the helicity angle θ_H ; see Section 4.4.1 for details. The selection method removes events from further consideration if the helicity angle is not compatible with an expected range of values. The weighting method retains all events and weights each one with a positive or negative factor. The weighting factor, which is a function of θ_H , is chosen such that the signal event yield remains unaffected, while most of the background is projected away.

Each of the above methods has been followed in combination with two different ways to obtain the ratio of the efficiencies of the hadronic to the radiative D_s^{*+} decay. First of all, signal Monte Carlo events have been used to determine the efficiency ratio; this is described in Section 4.8. Secondly, as explained in Section 4.9, the efficiency ratio has been calculated from a measurement of the decays $D^{*0} \rightarrow D^0 \pi^0$ and $D^{*0} \rightarrow D^0 \gamma$, and the known branching fractions of these decays.

The resulting values for $\Gamma(D_s^{*+} \rightarrow D_s^+ \pi^0) / \Gamma(D_s^{*+} \rightarrow D_s^+ \gamma)$ are shown in Table 8.1. Also listed are the branching fractions $\mathcal{B}(D_s^{*+} \rightarrow D_s^+ \pi^0)$ and $\mathcal{B}(D_s^{*+} \rightarrow D_s^+ \gamma)$, which can be calculated under the constraint

$$\mathcal{B}(D_s^{*+} \rightarrow D_s^+ \pi^0) + \mathcal{B}(D_s^{*+} \rightarrow D_s^+ \gamma) = 1, \quad (8.1)$$

i.e., under the assumption that the D_s^{*+} meson can decay only to $D_s^+ \pi^0$ or to $D_s^+ \gamma$.

Figure 8.1 compares the results obtained with the different methods. All four $\Gamma(D_s^{*+} \rightarrow D_s^+ \pi^0) / \Gamma(D_s^{*+} \rightarrow D_s^+ \gamma)$ values confirm the 1995 measurement of the CLEO Collaboration of $\Gamma(D_s^{*+} \rightarrow D_s^+ \pi^0) / \Gamma(D_s^{*+} \rightarrow D_s^+ \gamma) = 0.062_{-0.018}^{+0.020} \pm 0.022$ [1]. However, both the statistical errors and the systematic uncertainties of the measurements presented in this dissertation are much smaller than those given by CLEO.

	Efficiencies from Signal Monte Carlo	
	Selection Method	Weighting Method
$\frac{\Gamma(D_s^{*+} \rightarrow D_s^+ \pi^0)}{\Gamma(D_s^{*+} \rightarrow D_s^+ \gamma)}$	$0.0621 \pm 0.0049 \pm 0.0063$	$0.0653 \pm 0.0048 \pm 0.0082$
$\mathcal{B}(D_s^{*+} \rightarrow D_s^+ \pi^0)$	$0.0585 \pm 0.0043 \pm 0.0056$	$0.0613 \pm 0.0042 \pm 0.0073$
$\mathcal{B}(D_s^{*+} \rightarrow D_s^+ \gamma)$	$0.9415 \pm 0.0043 \pm 0.0056$	$0.9387 \pm 0.0042 \pm 0.0073$
	Efficiencies from D^{*0} Decays	
	Selection Method	Weighting Method
$\frac{\Gamma(D_s^{*+} \rightarrow D_s^+ \pi^0)}{\Gamma(D_s^{*+} \rightarrow D_s^+ \gamma)}$	$0.0574 \pm 0.0046 \pm 0.0089$	$0.0593 \pm 0.0044 \pm 0.0092$
$\mathcal{B}(D_s^{*+} \rightarrow D_s^+ \pi^0)$	$0.0542 \pm 0.0041 \pm 0.0080$	$0.0559 \pm 0.0039 \pm 0.0082$
$\mathcal{B}(D_s^{*+} \rightarrow D_s^+ \gamma)$	$0.9458 \pm 0.0041 \pm 0.0080$	$0.9441 \pm 0.0039 \pm 0.0082$

Table 8.1: Partial widths ratio $\Gamma(D_s^{*+} \rightarrow D_s^+ \pi^0)/\Gamma(D_s^{*+} \rightarrow D_s^+ \gamma)$ and branching fractions $\mathcal{B}(D_s^{*+} \rightarrow D_s^+ \pi^0)$, $\mathcal{B}(D_s^{*+} \rightarrow D_s^+ \gamma)$. The first error is statistical, the second represents systematic uncertainties.

$\frac{\Gamma(D^{*0} \rightarrow D^0 \pi^0)}{\Gamma(D^{*0} \rightarrow D^0 \gamma)}$	$1.7401 \pm 0.0204 \pm 0.1247$
$\mathcal{B}(D^{*0} \rightarrow D^0 \pi^0)$	$0.6351 \pm 0.0027 \pm 0.0166$
$\mathcal{B}(D^{*0} \rightarrow D^0 \gamma)$	$0.3649 \pm 0.0027 \pm 0.0166$

Table 8.2: Partial widths ratio $\Gamma(D^{*0} \rightarrow D^0 \pi^0)/\Gamma(D^{*0} \rightarrow D^0 \gamma)$ and branching fractions $\mathcal{B}(D^{*0} \rightarrow D^0 \pi^0)$, $\mathcal{B}(D^{*0} \rightarrow D^0 \gamma)$. The first error is statistical, the second represents systematic uncertainties.

The measurement of the event yield ratio $N(D^{*0} \rightarrow D^0 \pi^0)/N(D^{*0} \rightarrow D^0 \gamma)$ and signal Monte Carlo events for the channels $D^{*0} \rightarrow D^0 \pi^0$ and $D^{*0} \rightarrow D^0 \gamma$ have also been used to calculate the partial width ratio $\Gamma(D^{*0} \rightarrow D^0 \pi^0)/\Gamma(D^{*0} \rightarrow D^0 \gamma)$. The result as well as the branching fractions $\mathcal{B}(D^{*0} \rightarrow D^0 \pi^0)$ and $\mathcal{B}(D^{*0} \rightarrow D^0 \gamma)$, which have again been calculated under the assumption

$$\mathcal{B}(D^{*0} \rightarrow D^0 \pi^0) + \mathcal{B}(D^{*0} \rightarrow D^0 \gamma) = 1, \quad (8.2)$$

are shown in Table 8.2.

The branching fractions agree within error margins with the values in [3]: $\mathcal{B}(D^{*0} \rightarrow D^0 \pi^0) = 0.619 \pm 0.029$, $\mathcal{B}(D^{*0} \rightarrow D^0 \gamma) = 0.381 \pm 0.029$. However, the precision of the branching fractions is greater in the measurement presented here than in [3].

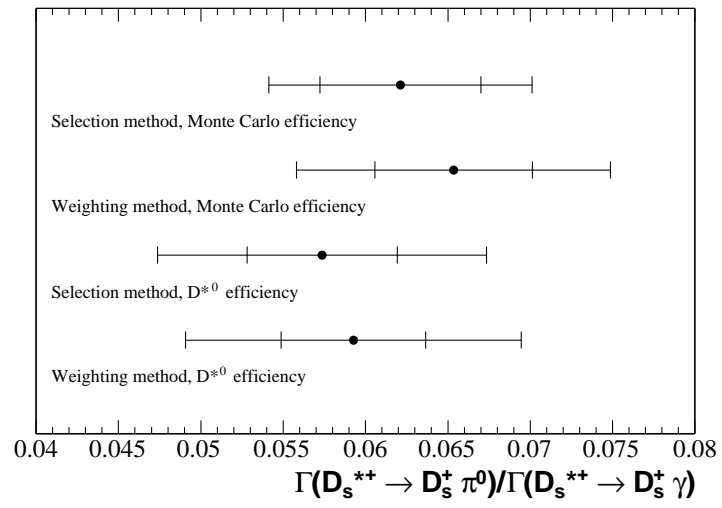


Figure 8.1: Comparison of $\Gamma(D_s^{*+} \rightarrow D_s^+ \pi^0) / \Gamma(D_s^{*+} \rightarrow D_s^+ \gamma)$ obtained with different methods.

References

- [1] J. Gronberg *et al.* (CLEO Collaboration), Phys. Rev. Lett. **75**, 3232 (1995).
- [2] B. Aubert *et al.* (BABAR Collaboration), Phys. Rev. Lett. **90**, 242001 (2003).
- [3] K. Hagiwara *et al.*, Phys. Rev. D **66**, 010001 (2002).
- [4] E. M. Henley and T. Meissner, Phys. Rev. C **55**, 3093 (1997).
- [5] J. Gasser and H. Leutwyler, Nucl. Phys. B **250**, 465 (1985).
- [6] P. L. Cho and M. B. Wise, Phys. Rev. D **49**, 6228 (1994).
- [7] J. F. Amundson *et al.*, Phys. Lett. B **296**, 415 (1992).
- [8] J. H. Christenson, J. W. Cronin, V. L. Fitch, and R. Turlay, Phys. Rev. Lett. **13**, 138 (1964).
- [9] PEP-II: An Asymmetric B Factory, Conceptual Design Report, SLAC-R-418 (1993).
- [10] D. Boutigny *et al.* (BABAR Collaboration), Letter of Intent for the Study of CP Violation and Heavy Flavor Physics at PEP-II, SLAC-R-443 (1994).
- [11] D. Boutigny *et al.* (BABAR Collaboration), BABAR Technical Design Report, SLAC-R-457 (1995).
- [12] D. G. Hitlin (for the BABAR Collaboration), First CP Violation Results from BABAR, SLAC-PUB-8698 (2000).
- [13] H. Aihara (for the BELLE Collaboration), A Measurement of CP Violation in B^0 Meson Decays with BELLE, hep-ex/0010008 (2000).
- [14] B. Aubert *et al.* (BABAR Collaboration), Phys. Rev. Lett. **86**, 2515 (2001).
- [15] A. Abashian *et al.* (BELLE Collaboration), Phys. Rev. Lett. **86**, 2509 (2001).
- [16] P. F. Harrison and H. R. Quinn, Editors, The BABAR Physics Book, Physics at an Asymmetric B Factory, SLAC-R-504 (1998).

- [17] B. Aubert *et al.* (*BABAR* Collaboration), Nucl. Instrum. Meth. A **479**, 1 (2002).
- [18] B. Aubert *et al.* (*BABAR* Collaboration), Phys. Rev. D **65**, 091104 (2002).
- [19] R. Gamet, R. Parry, and C. Touramanis, Luminosity Measurement for Run I and Run II data using SP4 Simulation, *BABAR* Analysis Document #535, Version 1, November 19, 2002, unpublished.
- [20] C. Hearty, Hadronic Event Selection and B-Counting for Inclusive Charmonium Measurements, *BABAR* Analysis Document #30, Version 5, July 23, 2000, unpublished.
- [21] M. Bona *et al.*, Report of the Tracking Efficiency Task Force for 2001, *BABAR* Analysis Document #324, Version 2, October 3, 2002, unpublished.
- [22] G. Mancinelli and S. Spanier, Kaon Selection at the *BABAR* Experiment, *BABAR* Analysis Document #116, Version 1, July 27, 2001, unpublished.
- [23] W. Dunwoodie, private communication (2002).
- [24] F. Bellini, S. Brunet, and F. Di Lodovico, Comparison between Monte Carlo and Data of the π^0 detection and reconstruction efficiency using τ 1-on-1 decays, *BABAR* Analysis Document #378, Version 1, September 17, 2003, unpublished.
- [25] H. Albrecht *et al.* (ARGUS Collaboration), Z. Phys. C **66**, 63 (1995).
- [26] F. Butler *et al.* (CLEO Collaboration), Phys. Rev. Lett. **69**, 2041 (1992).
- [27] J. Adler *et al.*, Phys. Lett. B **208**, 152 (1988).
- [28] P. D. B. Collins and T. P. Spiller, J. Phys. G **11**, 1289 (1985).
- [29] C. Peterson, D. Schlatter, I. Schmitt, and P. M. Zerwas, Phys. Rev. D **27**, 105 (1983).

Acknowledgements

I am thankful to my thesis advisor Prof. Dr. Bernhard Spaan of the *Institut für Kern- und Teilchenphysik* (Tech. Univ. Dresden) for giving me the opportunity to work on this interesting subject. Various helpful discussions with him have guided me through the work.

I am also thankful to Prof. Dr. Klaus R. Schubert (*Institut für Kern- und Teilchenphysik*) and Prof. Dr. Helmut Koch of the *Institut für Experimentalphysik I* (Ruhr-Univ. Bochum) who have agreed to referee this dissertation.

Discussions with and comments from my colleagues of the *BABAR* charm working group have greatly helped me. William Dunwoodie (SLAC) has provided very valuable advice by suggesting the weighting method to me.

My colleagues at the *Institut für Kern- und Teilchenphysik* have made it an enjoyable place to work at. I am particularly thankful to Rainer Schwierz, who works hard to support and administer the computer systems. Without his efforts, this work would not have been possible.

I am grateful to the *Deutsche Forschungsgemeinschaft (DFG)* and the *Bundesministerium für Bildung und Forschung (BMBF)*, which have supported this work financially.

Versicherung

Hiermit versichere ich, dass ich die vorliegende Arbeit ohne unzulässige Hilfe Dritter und ohne Benutzung anderer als der angegebenen Hilfsmittel angefertigt habe; die aus fremden Quellen direkt oder indirekt übernommenen Gedanken sind als solche kenntlich gemacht. Die Arbeit wurde bisher weder im Inland noch im Ausland in gleicher oder ähnlicher Form einer anderen Prüfungsbehörde vorgelegt.

Die vorliegende Arbeit wurde am Institut für Kern- und Teilchenphysik der Technischen Universität Dresden unter wissenschaftlicher Betreuung von Prof. Dr. B. Spaan angefertigt.

Dresden, den 05.04.2004

M. Dickopp

